3D Printing of Porous Polymeric Materials for Stationary Phases of Chromatography Columns

---

A thesis submitted in partial fulfilment of the requirements for the Degree of Doctor of Philosophy in Chemical and Process Engineering

By

Roya Rezanavaz

Department of Chemical and Process Engineering,

University of Canterbury,

New Zealand

2018

Abstract

The work described in this thesis focused on the creation of 3D printed chromatography columns using high internal phase emulsion polymer (polyHIPE) materials. The first step was to prepare and optimize a porous, polymeric stationary phase for chromatography. An approach used throughout the work was based on a special type of emulsion polymerization, the HIPE, which results in a highly porous, interconnected structure, in which the pore size and pore size distribution can be tightly controlled. Glycidyl methacrylate (GMA) is a reactive monomer that is frequently used for the preparation of functional polymers. The possibility of preparation of materials with a high level of porosity (up to 90%), pore size tuning and the availability of an epoxy reactive group for further chemical modification to include adsorptive ligands make GMA-based polyHIPEs good candidates for chromatographic applications.

Photo polymerization of GMA-based HIPE was achieved with a UV lamp operating at a 300-400 nm wavelength. Scanning electron microscopy and the

Brunauer–Emmett–Teller method were used to analyze the size and distribution of porosity as well as the surface area of the materials.

The polyHIPE materials reported to date have typically been weak and brittle, with a chalky consistency that crushes and readily breaks down under applied stress. The mechanical properties of the prepared porous polyHIPE materials were therefore improved using crosslinkers or co-crosslinkers of high molecular weights (average MW 286 and 550 g mol^{-1}). The Young's modulus of GMA-based polyHIPEs containing 40% PEGDMA increased by 50% and the crush strength by 400% when compared with traditional GMA/Ethylene glycol dimethylacrylate polyHIPEs. Subsequent morphological studies showed that the mechanically improved foams possessed the characteristic interconnected pore structure and properties of typical polyHIPEs, meaning that mechanical strength was improved without a loss of the desired high internal porosity.

For the first time, 3D-printed chromatographic columns were created from poly(HIPE) materials, using a digital light processing 3D printer that was developed to polymerize GMA-based HIPEs through control of UV scattering, light penetration and the monomer surface. Chromatographic columns (column size: 100 mL) with complex but uniform internal flow channel geometries (gyroids) with 50% porosity and 500 µm channel diameter were created by

computer aided design and printed layer-by-layer using the DLP printer. The GMA backbone epoxy groups in the printed columns were then chemically functionalized with diethylaminoethyl groups to create a printed anion exchange chromatography column. Residual carboxylic groups were capped with ethanolamine to remove cationic charges to ensure only anionic modality in the column.

The chromatographic performance of the functionalized, printed column with and without mechanical improvement was assessed using an ion-exchange chromatography system. The static BSA binding capacity of the basic printed, functionalized had a maximum protein capacity of 160 mg BSA g^{-1} polyHIPE, while it was 140 mg BSA g-1 polyHIPE for the mechanically improved one. The dynamic binding capacity of the mentioned monoliths was also measured in different flow rates from 0.5 ml min^{-1} to 6 ml min^{-1} and the maximum dynamic binding capacity at 50% breakthrough was 13.56 mg ml^{-1} polyHIPE. A complete separation of cytochrome C from BSA was achieved on both printed monoliths. This was done using an ion-exchange chromatography system, testing and optimizing the printed columns with different bimolecular solutions. Finally, the results show, for the first time, that the printed crosslinked GMA-based polyHIPE material is a promising material a stationary phase for separation of biomolecules in chromatography.

UNIVERSITY OF CANTERBURY
Te Whare Wānanga o Waitaha
CHRISTCHURCH NEW ZEALAND

Deputy Vice-Chancellor's Office
Postgraduate Office

Co-Authorship Form

This form is to accompany the submission of any thesis that contains research reported in co-authored work that has been published, accepted for publication, or submitted for publication. A copy of this form should be included for each co-authored work that is included in the thesis. Completed forms should be included at the front (after the thesis abstract) of each copy of the thesis submitted for examination and library deposit.

Please indicate the chapter/section/pages of this thesis that are extracted from co-authored work and provide details of the publication or submission from the extract comes:

Chapter 4 – results from this chapter has been published in the journal of applied polymer science as a full paper entitled "GMA- based emulsion- templated solid foams: Influence of co- crosslinker on morphology and mechanical properties" – Authored by Roya Rezanavaz, Conan Fee and Simone Dimartino.

Please detail the nature and extent (%) of contribution by the candidate:

Roya Rezanavaz is the first author of the abovementioned paper. Her works in the submitted PhD thesis involve literature search, experimental design,

data collection and analysis as well as writing of each chapter. Revision and refinement of the work is attributed to the other authors

Certification by Co-authors:

If there is more than one co-author then a single co-author can sign on behalf of all

The undersigned certifys that:

- The above statement correctly reflects the nature and extent of the PhD candidate's contribution to this co-authored work
- In cases where the candidate was the lead author of the co-authored work he or she wrote the text

Name: *Conan Fee* Signature:  Date: *31 July 2018*

Contents

List of Tables

List of Figures

List of Schemes

Chapter 1 Introduction

The subject of this thesis is the creation of 3D printed porous polymers from a high internal phase emulsion (HIPE) for use as chromatographic media. Chromatography is a mainstream purification process used in the biotechnology, pharmaceutical and food industries that requires intimate contact between solid and fluid phases. The stationary phase in liquid chromatography is composed of randomly packed beads that may themselves be porous or non-porous and/or a single piece of highly porous material with interconnected channels. Packed-bed column preparation has traditionally involved slurry packing, from which the chromatography columns are produced containing beads in a random close-packed configuration that has disordered packing. Chromatographic resolution and effectiveness are mainly affected by the flow-related properties of mass transfer, fluid distribution, back pressure and fluid dispersion, which in turn depend upon packing geometry. Because columns are

randomly packed and no two random packings are alike, an exact prediction of the detailed packed bed geometry is not possible.

Additive manufacturing technology (also known as 3D printing or rapid prototyping) offers a new approach for the manufacture of a single piece chromatography column with control of the shape, orientation and position of any geometric feature within the porous bed. In this technique, solid objects are created from computer aided design (CAD) models. The 3D printing group at the University of Canterbury was the first in the world to propose and demonstrate the concept of printing highly-ordered porous structures with finely controlled geometries for use in chromatography. The group includes a large number of active researchers from chemical engineering, mechanical engineering, physics, mathematics, computer science and chemistry, investigating a wide range of topics.

The first publication of the group by Fee et al. [1] in employing the use of 3D printing in chromatography describes the concept of fabricating perfectly ordered column packings with internal flow distributors and fluid fittings in one integrated piece. Later, Nawada et al. [2] evaluated the performance of 3D printed beds of ordered particles with a range of geometric shapes, thus for the first time, experimentally validating the computational predictions of the performance of simple cubic (SC), body centered cubic (BCC) and face centered

cubic (FCC) arrangements of spheres. They also show that the printed columns were highly reproducible with excellent fidelity to the computer-aided design models, which showed promise for 3D printing in the design of highly efficient 3D-printed columns in the future.

In another publication by Dolamore et al. [3] from the 3D printing group, the chromatographic performance of ordered configurations of particles in chromatographic processes including convection, diffusion and adsorption was simulated using computational fluid dynamics methods based on the Lattice Boltzmann Model. They demonstrated the advantages of ordered packings over randomly packed beds and evaluated the influence of the orientation of the ordered beds with respect to the main direction of flow. For the first time they introduced the key aspects that should be taken into account when designing new ordered morphologies for packed bed columns with improved performance.

Selection and development of suitable materials for stationary phase is also very important in optimizing the internal pore characteristics as well as strength and chemical functionality when printed using various approaches. In this regard, Gordon et al. [4] successfully produced various stationary phases made from agarose and cellulose hydrogels with different

chemical functionalities and of different geometries by using 3D printing methods.

High internal phase emulsions (HIPEs) have gained significant interest as stationary phase materials over the last 20 years, mainly due to their pore sizes (around 10 μm) and open pore structures that makes them highly permeable materials and an ideal media for separations at high flow rate. There have been some attempts for 3D printing of polyHIPE [5-8]. However, the printed structures were in simple shape such as lines or cylinder and the supposed applications for the printed polyHIPE were as a scaffold for tissue engineering [7] or a conductive object [8]. The work described herein aimed to use HIPE templated materials in 3D printing to produce a chromatographic stationary phase with complex geometry for separation of biomolecules. To the author's knowledge, this is the first time this has been achieved.

1.1 Project Objectives

The main goal of the current project was to develop a novel highly porous 3D printed monolith through meeting the following objectives:

- The development of macro porous polymeric materials with a controllable and highly interconnected porous structure.

- Determination of an optimum method for functionalizing the resulted porous polymeric materials.

- Investigation of different 3D printing techniques and choosing an applicable technique for creating chromatographic columns from functionalized porous polymeric materials, with designed flow channel geometries, with respect to printing behaviour.

- Optimization and characterization of the properties (adsorption capacity, mechanical strength, swelling, and chromatographic performance) of 3D printed functionalized porous materials for creating 3D printed chromatography columns.

1.2 Thesis organization

Based on the above objectives, the remainder of this thesis is organized as follows:

Chapter 2 is a literature review in three sections. Section 1 gives a brief overview of the different porous polymers available, with more specific detail on poly high internal phase emulsions (polyHIPEs), which are used regularly for synthesis throughout this thesis. Section 2 covers recent attempts to apply polyHIPE materials in chromatography columns and related functionalization

of polyHIPEs. Section 3 briefly outlines additive manufacturing and its various technologies, with a brief review of 3D printing of polyHIPE.

In *Chapter 3*, the optimization of the preparation and synthesis scheme for glycidyl methacrylate (GMA)-based polyHIPE, with attempts to control the morphology are discussed.

In *Chapter 4*, the improvement of the mechanical properties of GMA-based polyHIPEs in terms of toughness by using crosslinkers or co-crosslinkers of different molecular weights is described.

In *Chapter 5*, the development of a digital light processing (DLP) 3D printer for additive manufacture of a polyHIPE chromatographic monolith with a good fidelity to the designed models is presented.

In *Chapter 6*, the development of an anion exchanger from printed GMA-based polyHIPEs is discussed and the chromatographic performance of the mechanically improved/non-improved of the printed anion exchange monoliths is presented.

In *Chapter 7*, conclusions and recommendations for future studies are given.

Chapter 2 Literature Review

In this chapter, a background about the current research will be presented in three main topics including a brief review on different porous polymers and particularly the methods for preparation, properties and functionalization of polyHIPEs, a background of applications of polyHIPE in column chromatography, and a brief discussion about additive manufacturing and 3D printing of polyHIPE.

2.1 Porous Polymers

Porous polymers are a subdivision of porous materials that exploit of the ease of processability related with polymers to create monoliths, films, and beads, often with tuneable and well-defined porosities. The first reported application of porous polymers was in ion exchange resins and insulator, that rapidly continued with their outstanding performance in different types of column

chromatography and as gel separation media [9]. Meanwhile, porous polymers found applications as high tech materials for sensors [10], artificial antibodies [11] or as enantioselective catalysts [12], and their use for electro-optical [13] and (micro) electronic devices [14], implant materials [15] and supports for flow-through reactors [16] is currently being explored.

2.1.1 Macroporous copolymer networks

Macroporous copolymer networks are defined as a class of materials with a permanent, well-defined porous structure [17]. They are widely used in different types of column chromatography and in sorbent specific separations [18].

Crosslinked polystyrene foams were first created by free-radical crosslinking copolymerization of styrene and divinylbenzene using suspension polymerization. It was concluded that this novel polymer had a three-dimensional network structure, with solvent-filled pores of the typical size of the distance between two cross-linking units in the range between 3 and 50 nm [9, 19]. In the late 1950s, a new polymerization method that produced a solid crosslinked polystyrene polymer with a porous structure was discovered [20]. The method involved suspension polymerization of a styrene-divinyl benzene (S–DVB) monomer mixture in the presence of inert diluents (porogens) which

were removed from the polymer gel after polymerization. These new materials were called ‘macroporous’ polymer networks [18].

During the past 50 years, the synthesis of macroporous copolymer networks based on various chemical reactions and compositions has been the subject of numerous studies. The latest developments in the field include the invention of macroporous monoliths [21] and their implementation in capillary electrophoretic chromatography, nanoliquid chromatography, and reverse phase separation of proteins and peptides [22], as well as the microfluidic synthesis of macroporous copolymer particles with extremely narrow size distributions [23, 24].

Currently, a number of techniques are used for the production of rigid macroporous polymers. Classical synthesis routes towards porous polymers and resins, include induced phase separation or the use of gaseous supercritical media, such as supercritical carbon dioxide ($scCO_2$), and liquid porogenes, for certain applications, such as electrophoresis gels or supports for solid-phase chemistry [9, 25]. The polymers are obtained as macroscopic monolithic or particulate materials. Recently, concepts of template synthesis and the employment of self-organizing templates have become increasingly important for the synthesis of porous materials.

Colloidal templating is a template synthesis method that generally used to create macroporous polymers. In this method a two-phase system is created and then the continuous phase is polymerized. Depending on the type of the employed colloidal templating system (emulsions, microemulsions or solid particles), the characteristic pore size can vary from a few nanometers to hundreds of micrometers [26].

2.1.2 Emulsion Templating

An emulsion can be characterized as a dispersal of immiscible liquids. Usually the emulsion can be kept in a semi-stable state by incorporating suitable surfactants. A schematic of two basic types of emulsions: oil-in-water (O/W) and water-in-oil (W/O) is shown in Figure 2-1.

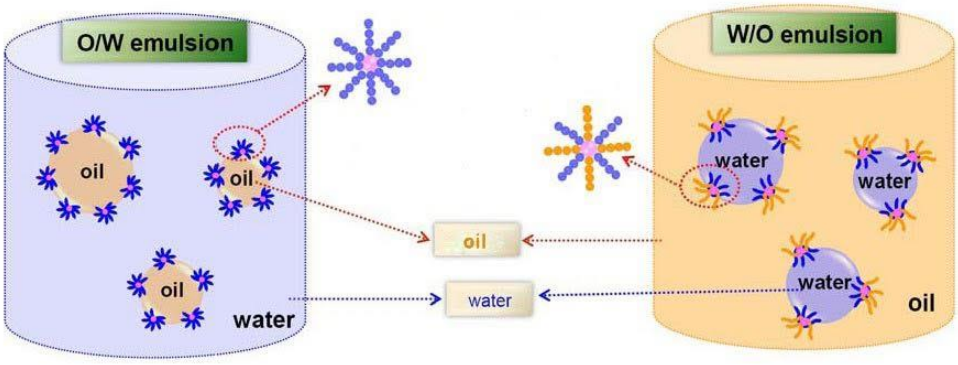

Figure 2-1. Schematic of stabilised O/W and W/O emulsions.

Emulsion polymerisation consists of two ways for forming polymers. One method to create polymer beads is for an emulsion to be formed of a monomer mixture with an immiscible solvent, such as water. The formed emulsion is then polymerized, by heat, UV irradiation, or redox reactions as examples, so that the internal phase of the emulsion is polymerised, creating discrete particles. In this method, controlling of the size and distribution of the particles in the emulsion will resulted in the formation of polymerized beads with controlled size and shape. Conversely, if an emulsion is formed by curing the monomer mixture as the continues phase, the water droplets are then suspended within an enclosed polymer structure.

2.1.3 High Internal Phase Emulsion

Emulsion templating using high internal phase emulsions (HIPEs) is an effective way to prepare low-density, high-porosity macroporous polymers known as polyHIPEs. A HIPE is an emulsion in which the internal (or dispersed) phase occupies more than 74% of the total volume fraction. This figure is the average density of maximal packing by Kepler's conjecture, where droplets are non-deformable and spherical. High internal phase emulsion systems exceed this maximum packing and for that reason the droplets are forced into non-uniform polyhedral shapes, separated by thin continuous films [27, 28].

HIPEs are non-equilibrium systems because of the maximized interfacial free energy associated with their large interfacial area [28]. The system is not at its minimum total free energy and is thus far from equilibrium. Like ordinary non-concentrated emulsions, HIPEs can be prepared from water-in-oil (W/O) or oil-in-water (O/W) types. While these types are most common, Oil-in-water-in-oil (O/W/O) [29] and water-in-oil-in-water (W/O/W) HIPEs are becoming increasingly common [30]. High internal phase emulsions are highly viscous, paste-like emulsions, where their viscosity is influenced by the concentration of the internal phase and vigorous mixing, by surfactant proportion [31] and by droplet size or the temperature of the internal phase [32].

As mentioned above, HIPEs are a class of emulsions with an internal volume phase of greater than 74%. In the context of porous solids they provide a flexible synthetic route to a variety of materials. This is achieved by including monomers within the external or internal phase and then polymers can be synthesized within the HIPE. By this procedure, porous polymers with more than 74% of porosity can be prepared. The preparation of these highly porous materials consists of dropwise addition of the droplet phase to the external phase mixture during constant stirring to form a uniform HIPE. Mixing is followed by polymerisation of the continuous phase, which depends upon the initiation system used; thermal-, redox-, catalytic-, UV-, or microwave-induced

initiation and is washed generally by Soxhlet extraction and vacuum-dried. The stages of polyHIPE formation are shown in Figure 2-2.

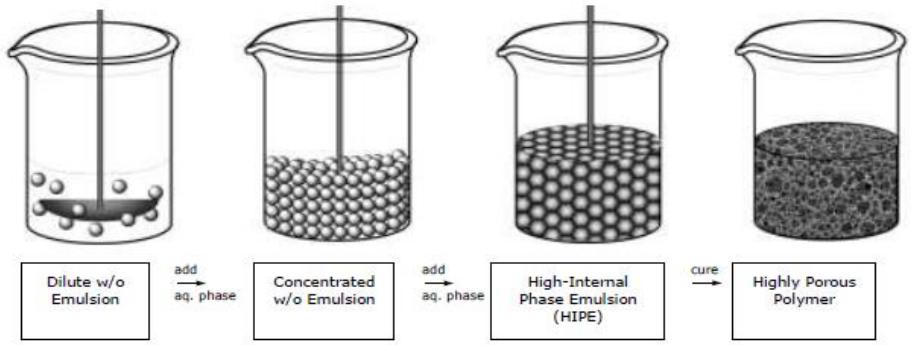

Figure 2-2. Schematic of the steps required to make a polyHIPE material from an emulsion [24].

Typically, polyHIPEs are synthesized using typical free radical copolymerization (FCC) in surfactant-stabilized W/O HIPEs. However, other polymerization techniques (e.g. step-growth, , atom transfer radical polymerization (ATRP), cationic polymerization, ring opening metathesis polymerization (ROMP)), other HIPE stabilization methods (e.g. the particle-based stabilization in Pickering HIPEs), and other types of HIPEs (e.g. oil-in-water (O/W), water-in-oil-in-water (W/O/W) have also been studied [17].

The FCC system for the synthesis of macroporous copolymers generally includes a monovinyl monomer, a divinyl monomer (crosslinker), a surfactant, an initiator and the dispersed aqueous phase as porogen. The decomposition of the initiator produces free-radicals that initiate the polymerization and crosslinking reactions. After a particular reaction time, a three-dimensional network of infinitely large size may start to form. At this point the emulsion system (monomer–water mixture) changes from a liquid to a solid-like state. This state of the emulsion is called the "gel point". After conversion of monomers to a polymer, only the polymer network and the aqueous phase remain in the reaction system.

In the past, thermal polymerization has been used as a technique to polymerize high internal phase emulsions "HIPEs". The thermal polymerization technique is very time intensive and heating is known to destabilize HIPE formulation. The time consuming and the requirement for a stable emulsion limits the types of monomers and surfactants that may be used in a thermal polymerization process. Therefore, photopolymerization was preferred over its thermal equivalent [24, 33].

Resulting PolyHIPEs typically exhibit a distinctive open pore system (Figure 2-3). Terminology of polyHIPEs varies between research groups. The spherical pores caused by the water droplets (typically of the size range 1 - 100

μm) are called "cavity", "voids", "cells", "pores", and the interconnecting holes between these are called, "holes", "interconnects", "windows", "pore throats", "channels", amongst other terms [34]. Throughout this work, the terms "pore" and "window" will be used. The interconnecting windows often form at the thinnest points of the continuous phase film surrounding the droplet phase. The extensive formation of these windows transforms the slight shrinkage of the continuous phase during the polymerisation because of volume contraction [35, 36]. Another explanation is that interconnecting pore formation is a postpolymerisation process and is generated as a result of extraction and drying in vacuum [37].

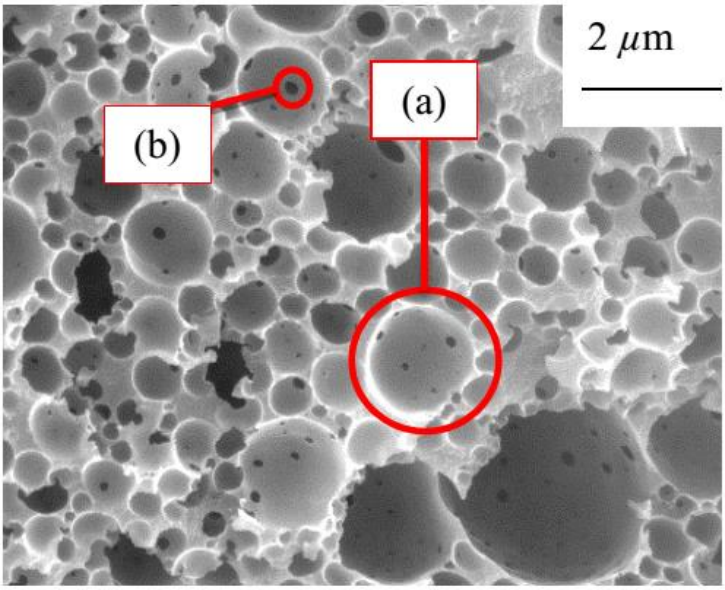

Figure 2-3. SEM image of a typical PolyHIPE. (a) defines a "pore" and (b) an "interconnect" window.

Poly(HIPE)s are mostly prepared via a bulk process, thereby resulting a monolith. However, there have been various reported synthesis methods in the literature for polyHIPE beads. Zhang and Cooper reported the production of monodisperse hydrophilic polyHIPE beads (~2 mm diameter) of polyacrylamide (PAM) by sedimentation polymerisation [38]. Recently, by dispersing HIPEs into a third phase, high internal-phase double emulsions were used to fabricate monodisperse polyHIPE spheres and rods, with diameters of approximately 400 μm [24]. Droplets were generated in a co-flow device from a water-in-oil HIPE, hence creating a W/O/W emulsion. Spherical beads

were created through the photopolymerization of monomers within the single droplets (Fig. 2-4).

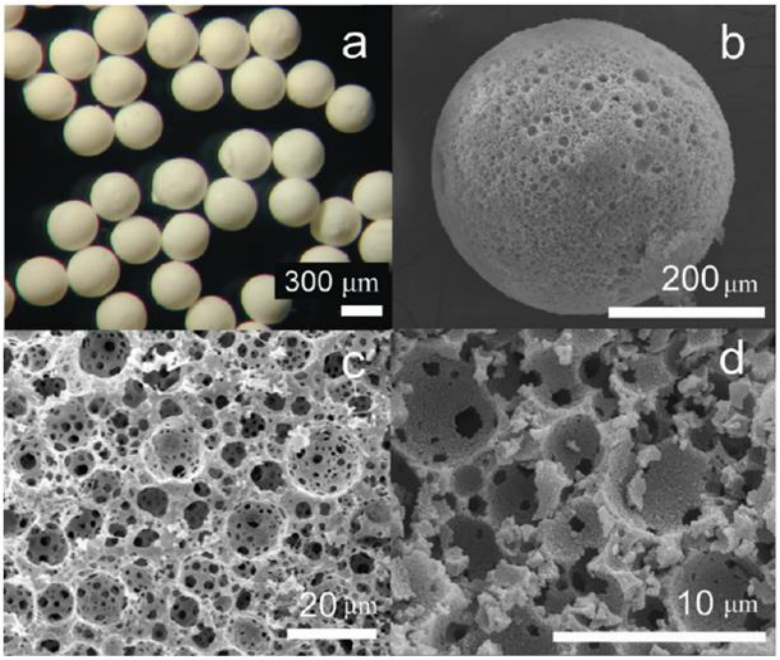

Figure 2-4. Porous, monodisperse spherical polyHIPE beads: (a) optical microscopy image of size monodispersity; SEM images of (b) a bead, (c) surface of a bead, and (d) inner part of a broken bead [15].

The final structure of polyHIPE depends on the form and stability of the parent emulsion and parameters such as curing time and temperature. Tuning the parent emulsion to define and control emulsion parameters and to produce a stable emulsion, with defined pore size, shape and architecture is discussed further in the literature [39-41]. Williams and Wrobleski were the first to investigate the influence of synthesis factors on the pores (cellular) structure

of porous materials [86]. It was shown that surfactant (emulsifier) concentration played the most important role in influencing the porous structure, while internal phase volume ratio also had an influence. Increasing the surfactant concentration resulted in thinning of the monomer films between neighbouring droplets in the emulsion. It was hypothesized that the thickness of monomer films between neighbouring droplets in the emulsion decreased with increasing the surfactant concentration. Attaining a particular critical film thickness, would create interconnecting windows between the neighbouring droplets during polymerisation. Considering this hypothesis, the reason for creation of interconnecting windows would be film shrinkage during conversion of monomer to polymer. During this time the separating monomer film between adjacent droplets is at its thinnest point, as confirmed by cryo-SEM studies of Styrene/Divinylbenzene HIPEs by Gregory et al. [36]. They showed that the gelation point of polyHIPE polymerisation coincides with the creation of the first interconnecting windows. It has been also noted [86] that an increase in surfactant concentration relative to monomer content (w/w) above 50%, would result in weak, unconnected porous materials.

The other influence of an increase in surfactant concentration is a decrease in average pore diameter as a result of increased emulsion stability. The average pore diameter of polyHIPE is in the range of 1 μm to more than 100 μm. The

key parameter for controlling the pore diameter is the proportion of more hydrophobic monomer. Wiliams et al. [86] have found a significant decrease in average pore diameter with an increasing proportion of a more hydrophobic monomer. They suggested that increasing the proportion of the more hydrophobic monomer would result in a decrease in interfacial tension, creating smaller droplets and increasing the emulsion stability.

Finally, it was demonstrated that increasing electrolyte content in the aqueous phase resulted in a dramatic decrease of average pore diameter [86]. The reason stated for this is a reduction in the tendency for Ostwald ripening with increasing electrolyte concentration. Ostwald ripening is a phenomenon in which large droplets grow at the expense of smaller ones due to the migration of droplet phase molecules through the continuous phase. If Ostwald ripening occurs in an emulsion, it leads to coalescence and, finally, emulsion break-down. Therefore, limiting Ostwald ripening with increasing electrolyte content results in a more stable emulsion with a smaller average droplet diameter.

Although polyHIPEs have significantly high porosity and interconnectivity, they possess low surface area (around 5 m2 g–1) because of their relatively large pore size (microns to 10’s of microns). This character of polyHIPEs hampers their application as stationary phases for chromatography, which requires high surface areas because all of the action takes place at the solid surface and rapid

exchange processes require high surface areas. There have been some attempts reported in the literature to increase the surface area of polyHIPEs. Hainey and co-workers [77] showed that replacing some of the monomer (up to 50% by vol.) with a non-polymerisable (water-immiscible) organic solvent in conjunction with a high crosslinker content, results in a high surface area of up to 350 m2 g-1 [77]. It was found that the closer the value of the solubility parameter of the solvent to that of the polymer, the larger the windows connecting adjacent cells, gaining high surface area materials with better mechanical performance [41].

2.1.4 HIPE Stability

HIPEs can remain stable for periods ranging from several hours to under a minute, and although the mechanisms behind their high stability are not fully understood, there are several factors that contribute to HIPE stability. The instability in the parent emulsion is caused by two main effects, droplet coalescence and Ostwald ripening [42], which lead to a coarsening of the emulsion and increase in droplet size. Coalescence is where two droplets meet and merge, and Ostwald ripening is a thermodynamically driven effect where larger, more energetically favoured droplets grow larger at the expense of smaller droplets, because of molecules in the dispersed phase migrate from smaller droplets towards larger droplets through the continuous

phase, leading to an overall minimization of total surface area. The nature of the surfactant is the foremost variable that affects stability [33]. Nevertheless, the concentration of the surfactant as well as the internal phase ratio, the electrolyte concentration of the aqueous phase, the viscosity of the continuous phase, the nature of the two phases and the temperature of the HIPE also affect overall stability [43].

The Hydrophilic-Lipophilic Balance, or HLB, is a concept that describes an association between the structural properties of a surfactant and its emulsifying properties. It is a semi-empirical scale based upon the relative percentage of hydrophobic to hydrophilic groups. The HLB of a surfactant affects the stability of HIPE. High HLBs are required to form O/W HIPEs and conversely low HLBs are required for W/O HIPEs. Typical W/O surfactants have an HLB number in the range of 4-8 and an O/W surfactant in the range 12-16 [44]. However, other surfactant properties must also be taken into consideration. For two surfactants with identical HLB, the surfactant with the highest molecular weight will produce the most stable HIP [45, 46]. Surfactant concentration can also play a vital role. Below a certain concentration HIPEs are always unstable because of incomplete coverage of the emulsion droplets.

Another important factor is the nature of the two phases, as well as the necessity for the surfactant to be more soluble in the continuous phase, HIPEs will

be more stable the greater the insolubility between the two phases [47]. In addition, the viscosities of the two phases are important, and an external phase with a high viscosity prevents efficient mixing of the HIPE, which leads to a smaller maximum possible volume fraction [31].

The presence of electrolytes in the immiscible phase can increase the stability of the emulsion through interactions between the hydrophilic portion of the surfactant and the electrolyte, which further increase surfactant solubility in the aqueous phase and inhibition of the Ostwald ripening process [48].

Another approach for stabilizing HIPEs is using solid amphiphilic particles [21, 29]. Pickering emulsions are stabilized by solid particles, which self-assemble at the oil–water interface, thus preventing droplet coalescence. PolyHIPEs were successfully synthesized from stabilized HIPEs, with over 74% internal phase, using relatively low loadings of nanoparticles (1%) based on the monomer content. W/O Pickering HIPEs were successfully formed through the dispersion of nanoparticles in the organic continuous phase, however carbon nanotubes (CNT) for the formation of W/O Pickering HIPEs also dispersed in the aqueous internal phase. However, polyHIPEs from Pickering HIPEs usually tend to have closed-cell-like structures, while small amounts of surfactant can promote the formation of more open-cell structures for such polyHIPEs [38, 49].

2.2 PolyHIPE as a Chromatography Column

PolyHIPEs have been investigated for use in numerous applications, including as supports for chemical reactions [44, 50], scavengers [51], chromatography columns for separations [52], scaffolds for cell growth [53, 54], and absorbents for purification and storage [55, 56].

Column chromatography in chemistry is a method used to purify individual chemical compounds from mixtures of compounds. The adsorbent or stationary phases in column chromatography are usually beaded polymers or finely ground powders (packed bed) and/or a single piece of highly porous material with interconnected channels (monoliths). Table 2-1 gives a summary of the properties of commercial stationary phases in anion exchange column chromatography.

Table 2-1. Properties of commercial porous polymeric stationary phases in chromatography.

Commercial stationary phases	**Material**	**Particle size**	**Pore size**	**Dynamic binding capacity (mg/mL media)**
Capto DEAE	Highly cross-linked agarose with dextran surface extender	90 µm		> 90 mg ovalbumin
DEAE Sepharose Fast Flow	cross-linked agarose, 6%, spherical	~90 µm		110 mg HSA/ml medium
SOURCE 15Q	Polystyrene/divinyl benzene	15		45 (mg/ml gel)

DEAE Sephacel		~100 µm		10 mg Thyroglobulin (MW 669 000)/mL drained resin, 160 mg HSA (MW 68 000)/mL drained resin
TOYOPEARL DEAE-650C	hydroxylated methacrylic polymer	100 µm	100 nm	25 - 35 g/L
TSKgel DEAE-5PW (20)	hydroxylated methacrylic polymer	20 µm	100 nm	25 - 45 g/L
TOYOPEARL SuperQ				
CIM (Convective Interaction Media)	Poly(glycidyl methacrylate - co- ethylene dimethacrylate)	Channel size: 675 nm		≥ 20 mg BSA/ml
ProSwift WAX-1S	Polymethacrylate			18 mg/mL BSA

The particular structure of monoliths (interconnected network of open pores) enables them to withstand higher flow rates than packed bed columns due to lower backpressure, resulting in shorter times for analytical chromatography. It also results in several properties such as flow resolution and dynamic binding capacity unaffected by flow, and high dynamic binding capacities for very large molecules such as proteins and DNA or particles such as viruses. Monolithic columns can be made from silica or organic polymers. The structure of silica monolith contains large pores and nanometre-scale pores that provide a large specific surface area around 400 m^2/g. It has been mentioned in the literature [57] that silica supports are particularly suitable for separation of small

molecules with MW<1000 Da. However, for the separation of large molecules such as nucleic acids, synthetic polymers and proteins, polymeric monoliths are generally preferable due to their larger pore diameter which notably resulted in lower surface area (50 m^2/g) [57, 58, 59].

There are further discussions about porous polymer monoliths in literature but just a few attempts have been reported regarding application of polyHIPE monoliths. The main reported area of application of polyHIPE monoliths were in separation of small molecules and large biological molecules [60]. In the area of small molecules separation, removal of environmental contaminants, especially heavy metals of groundwater, has been extensively researched and implemented in successful commercial systems. However, high backpressures in commercial packed bed columns limit their separation quality. Because of this limitation, polyHIPE materials offering interconnected network channels have been investigated in several studies into removal of heavy metals from water, such as glycidyl methacrylate (GMA) polyHIPE [61], styrene-co-vinylbenzyl chloride-co-divinylbenzene polyHIPEs [62] and isodecylacrylate-co- divinylbenzene polyHIPE [63]. All of the investigations demonstrated the suitability of polyHIPE materials for high pressure applications as well as their advantages in offering superior efficiencies over polymer resin beads and carbon adsorbents.

For application of polyHIPE monoliths in chromatographic separation of large biomolecules such as proteins, GMA is the most frequently used monomer for the preparation of functional polymers. Yao et al. demonstrated an improved protein separation using GMA- Ethylene glycol dimethylacrylate (EGDMA) as a stationary phase with a near complete separation within 1 min of a standard mixture of lysozyme, bovin serum albumin (BSA), ovalbumin and pepsin at a high flow rate of 6 ml min^{-1} [64]. They also compared the binding capacity of GMA polyHIPE with Convective Interaction Media (CIM) columns in another study, where the binding capacity was 12.5 mg mL^{-1} higher than the commercial ones. In addition, a GMA polyHIPE separated cytochrome c, myoglobin, ribonuclease A, lysozyme and BSA at a high flow rate (1440 cm h^{-1}) within 4 min in comparison with a conventional GMA monolith [65]. Krajnc et al. prepared GMA-EGDMA polyHIPEs with porosities of 60%, 75%, 80% and 90% in a CIM disk format and used them for comparison with commercial CIM disks in protein separation. They functionalized GMA-EGDMA with diethylamine (DEA) to bear weak-anion exchange groups and tested them on the separation of a standard protein mixture. Although they achieved an improved run time of 0.6 min for the polyHIPE, they observed a higher dispersion compared with commercial CIMs, accompanied by significant co-elution of myoglobin, conalbumin and soybean trypsin inhibitor. They also measured dynamic binding capacities of GMA-based polyHIPE monoliths with

90% porosity, which had the largest pores and consequently the lowest surface area amongst the prepared samples. The reported BSA dynamic binding capacity at 50% of absorbance in breakthrough curve was around 9 mg mL^{-1} which is two times lower than conventional methacrylate monoliths [66]. In later work, they added ethylhexyl acrylate (EHA) to the GMA-based formulation to improve the mechanical rigidity of the polyHIPE, however while they achieved an elastic polyHIPE and brittleness was overcome, the separation efficiency was compromised and the measured dynamic binding capacity remained around 9 mg mL^{-1} [67]. Yang et al. prepared polyHIPEs from a vinyl ester resin cross-linked with EGDMA and used for separation of immunoglobulins from human plasma and egg yolk. They chose a vinyl ester monomer to improve mechanical rigidity of the polyHIPE and also the presence of hydroxyl groups in the matrix for further modifications. Morphological characterization of the prepared polyHIPE showed that the obtained open porous foam had an average pore diameter of 0.85 μm and a specific surface area of 121.96 m^2g^{-1}. The resultant dynamic binding capacity of lysozyme was 1.579 mgg^{-1} with water as the mobile phase and 1M NaCl as the eluent. They also showed a high resolution separation of interleukin-18 and lysozyme within 2 min at a rate of 1445 cmh^{-1} [65].

As demonstrated in all the above mentioned reports, the potential of polyHIPEs for use in protein separation at high operating flow rates without mechanical deficiencies is clear. In addition, the high potential of these materials for chemical modification and tailoring the selectivity for a particular analyte makes them desirable materials as stationary phases.

2.3 Functionalizing of polyHIPE

To achieve the specific separation ability, reactivity or absorptivity required in many of optimized porous polyHIPEs, they must be functionalized to introduce special functional groups onto the polyHIPE surfaces. To this aim, two different functionalization methods have been reported; using a co-monomer containing the desired functional group during HIPE formulation, post-functionalization of prepared polyHIPE by reaction with small organic molecules or grafting functionalised macromolecules chains to the prepared polyHIPE. While the first method above seems to be most convenient, as it is a one-step reaction, there are several drawbacks that should be considered. For instance, incorporation of a copolymer with polar functional groups that are more hydrophilic can result in destabilization of the parent emulsion, so this method is limited to comonomers containing hydrophobic functional groups [68] . Although the second method can be considered as a two-step process, the final functionalized polyHIPE can retain its tailored morphological structure. On the other hand, the

excellent achievable conversion under mild conditions with the post-functionalized method, makes this method the preferred method for functionalizing polyHIPEs. In this method monomers bearing reactive groups are commonly used in the HIPE formulation, so that the surface of the resulting polyHIPE can be readily modified through appropriate surface chemistry reactions. The surfaces of polyHIPEs containing epoxy or carboxyl moieties can be readily post-functionalized through nucleophilic substitution. To achieve good modification results, the chosen solvent should have good swelling properties for both the unmodified and modified polyHIPE. The post modification of polyHIPE has been shown to be feasible, thanks to its open porous morphology [30]. Table 2-1 gives a summary of several reports on post-functionalization of polyHIPEs and their applications. As can be seen from Table 1 most post-functionalization has been done on ST/DVD and acrylic monomers. Krajnc et al. have studied a series of post-functionalizations using different monomers such as functionalization of aryl acrylate-based polyHIPEs with an amine (tris(hydroxymethyl)aminomethane, tris(2-aminoethyl)amine) to use these materials as monolithic porous reactive supports [69], modification of acrylic acid polyHIPE with amines [70].

Table 2-2. Post-functionalization of various polyHIPEs and their applications [71].

Monomer/Crosslinker/Comonomer	Post Functionalization	Application
Styrene/Divinylbenzene	Nitration, bromination, sulfonation	Catalyst for the hydration of cyclohexene, ion exchange modules
Styrene/Divinylbenzene/ Vinylbenzyl chloride	Nucleophilic substitution	Catalyst support, Scavenger resins
Styrene/Divinylbenzene/ Vinylbenzyl chloride	4-Iodobenzoic acid	Support material in suzuli cross-coupling reactions, yielding pure biaryl products
Styrene/Divinylbenzene or EGDMA/ (2,4,6Trichlorophenyl)acrylate	Nucleophilic substitution	Scavenger resins
Styrene/Divinylbenzene or EGDMA/ n-propyl acrylate	Reacted to possess acid chloride and amino or hydroxy functionality	Scavenger resins, removal of atrazine from aqueous solutions
DVB or EGDMA/GMA	Hydrolysis	Monolithic supports for protein separation
Isobornyl Acrylate/2-Ethylhexylacrylate /trimethylolpropane triacrylate / N-Acryloxysuccinimide	Nucleophilic addition	Immobilization of enzyme CAL-B
Dicyclopentadiene	Thiol-ene reaction, oxidation followed by hydrazine formation	—
N,N-methylenebisacrylamide/Acrylic acid	Chlorination	Scavenger resins
GMA/EGDMA	Nucleophilic substitution	Separation of protein mixture

GMA/Methyl methacrylate/EGDMA	Pentaerythritol tetrakis(3mercaptopropionate), 1,9-nonanedithiol and 2-aminobenzenethiol	Removal of Silver, lead and cadmium ions

and vinylbnzyl chloride-based polyHIPEs modified with amines and hydroxyl groups [72]. Unilever also described in the patent literature the functionalization of poly(4-vinylbenzyl chloride) monoliths containing reactive benzyl chloride moieties using a variety of nucleophiles including amines, carboxylates, and alkoxides. They reported the investigated ion-exchange properties of the resulting modified monoliths [73, 74]. Benicewicz et al. demonstrated surface grafting of polyVBC with poly(4-vinylpyridine) by UV-initiated graft copolymerization of 4-vinylpyridine over modified benzyl chloride residues. The resulting monoliths were used in separation of heavy metals from aqueous solutions under flow-through conditions [75]. Sulfonation [76] and nitration [77] of poly(styrene-co-divinylbenzene) polyHIPE also has been reported, however, solvent compatibility of styrene-based polymers can present a problem due to the uniformly nonpolar structure of the polymer backbone.

2.4 Acrylic-based polyHIPE

The first used monomers in preparation of polyHIPE was styrene-co-divinylbenzene in the early 1970's [78] and until now it has been the most commonly used one. In the mid-1990's, researchers began to synthesize

polyHIPEs within o/w or w/o emulsions from different monomers including acrylates, methacrylates, 2-ethylhexyl acrylate, 4-vinylbenzyl chloride, acrylic acid (AA), and 2-hydroxyethyl methacrylate (HEMA). Although styrene-based polyHIPEs are the most common used polyHIPEs, it is well-known that the nonpolar structure of styrene in these highly porous materials results in compatibility problems with polar solvents. Despite styrene, various acrylic monomers have high potential for use in a wide range of applications, including chromatographic applications because of their compatibility with different solvents and their different mechanical properties, changing from brittle to elastomeric, while retaining the required morphology, density, and porosity for each application.

Among different acrylate monomers, GMA is a widely used monomer in HIPE formulations. GMA presents epoxy reactive moieties that are able to react with a range of nucleophiles, thus making it suitable for further chemical modification. Several authors have reported the preparation of GMA-based polyHIPE materials by thermal or photochemical polymerization, and their successive functionalization with nucleophiles [23].

2.5 Additive Manufacturing

Additive manufacturing (AM), colloquially known as 3D printing, is an attractive technology because of its potential to create a variety of macrostructured architectures such as medical implants, and to produce plastic prototypes for engineers and designers. AM technologies (Figure 2-5) that build complex 3D objects by adding layer-upon-layer of material include selective laser sintering (SLS; which is called micro laser sintering (μLS) in microscale) based on obtaining 3D structures by starting with powder, 3D printing (3DP), inkjet printing processes, fused deposition modelling (FDM) based on melting a polymer that enables patterning with the liquid, and laminated object manufacturing (LOM) based on gluing layers of adhesive-coated paper, plastic, or metal laminates together and cutting to shape with a knife or laser cutter. Another technique is stereo lithography (SL; which is called micro-SL (μSL) in microscale) obtaining 3D structures by scanning or projection an UV beam on a liquid polymerizable monomer resin and curing the resin into a solid polymer layer by layer, and stacking together all layers with various contours. In this work we aim to fabricate a porous chromatography column via μSL.

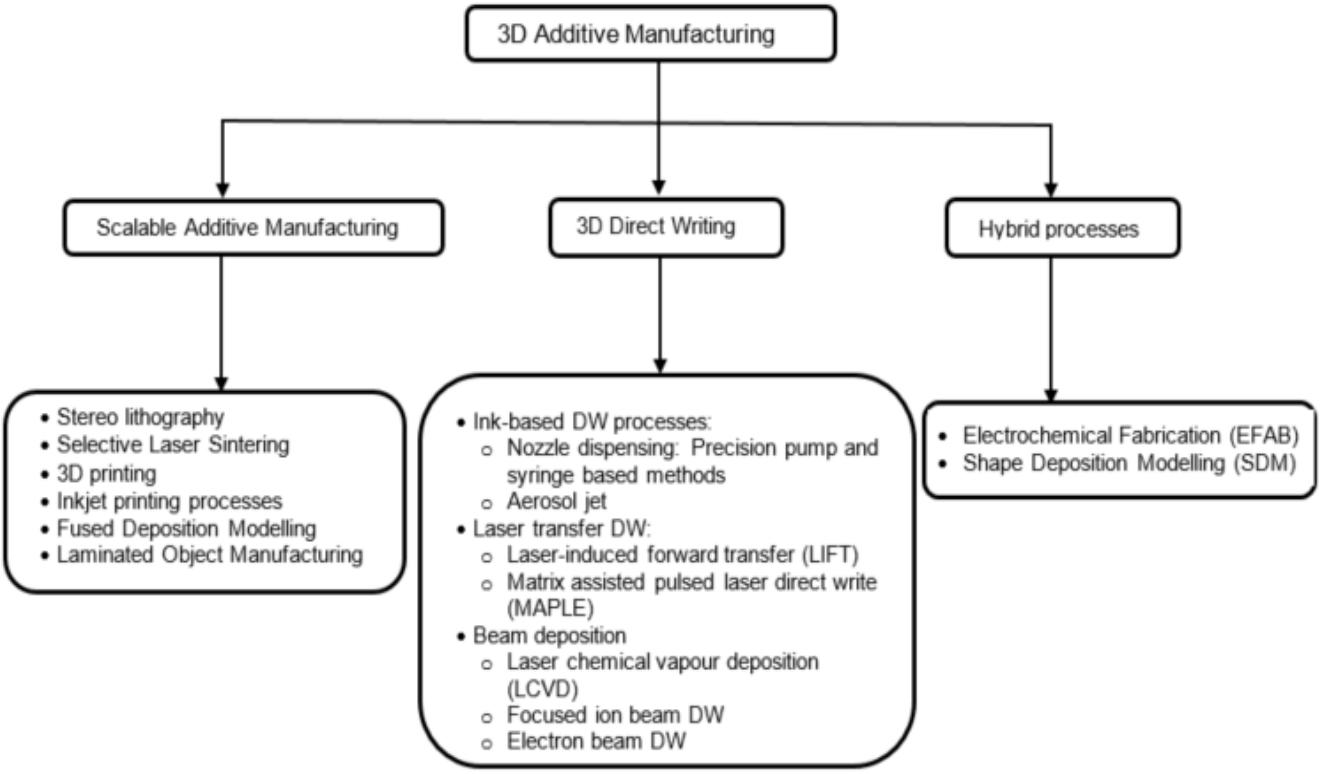

Figure 2-5. Classification of 3D micro-AM processes [70].

2.5.1 Micro stereo lithography (μSL)

Rapid prototyping processes or additive manufacturing μSL, which is derived from conventional stereo lithography, is used mainly for the production of 3D structures, using different types of monomers and additives. A schematic of the basic principle of stereo lithography is shown in Figure 2-6. In this method a 3D

solid model designed by Computer Aided Design (CAD) software is sliced into hundreds or thousands of horizontal layers with uniform thickness. For each layer, the focused scanning UV beam traces a cross-section of the part pattern on the surface of the liquid resin that is absorbed by the UV curable solution, leading to the polymerization solidifying the solution. After the pattern has been traced, the controlled elevator platform moves downward by a distance equal to the thickness of a single layer, then a resin-filled blade sweeps across the cross-section of the part, re-coating it with fresh material that can be solidified as the next layer and bonded with the previous layer. With the synchronized x–y pattern tracing and the z-axis motion, the complicated three dimensional object is built in a layer by layer fashion.

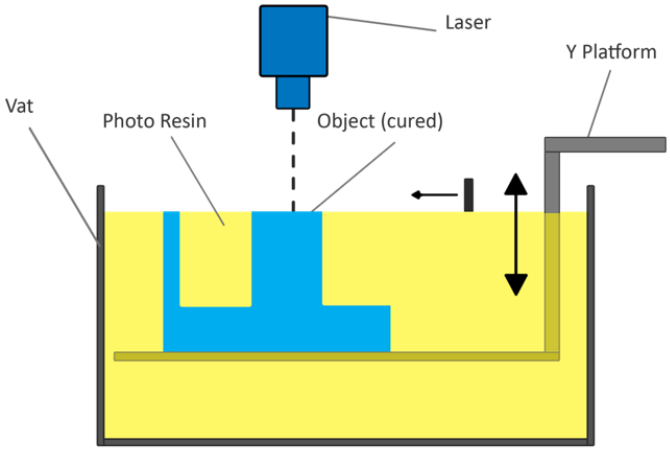

Figure 2-6. Schematic of stereo lithography set-up [70].

2.5.2 Digital Light Processing (DLP)

Digital Light Processing (DLP) is a method of printing that is very similar to sterolithography but with a different light-source (Figure 2-7). While in stereolithography ultraviolet lasers are the possible light sources, DLP utilizes a digital micro mirror device (DMD) to project patterns with a resolution of up to 10 µm onto a layer of photoresist and selectively polymerized individual pixels within a thin layer. Several hundred thousand microscopic mirrors arranged in a rectangular array on the surface of a DMD chip correspond to the pixels in the

image to be displayed. With the use of DMD, an entire layer can be cured at once, which makes DLP faster than most forms of 3D printing. The DLP method is currently used mainly for the production of 3D structures. The Envision Tec Ultra (EnvisionTEC Inc., Dearborn, Michigan), MiiCraft High Resolution 3D printer (MiiCraft, Germany), and Lunavast XG2 (Lunavast, Japan) are examples of DLP printers.

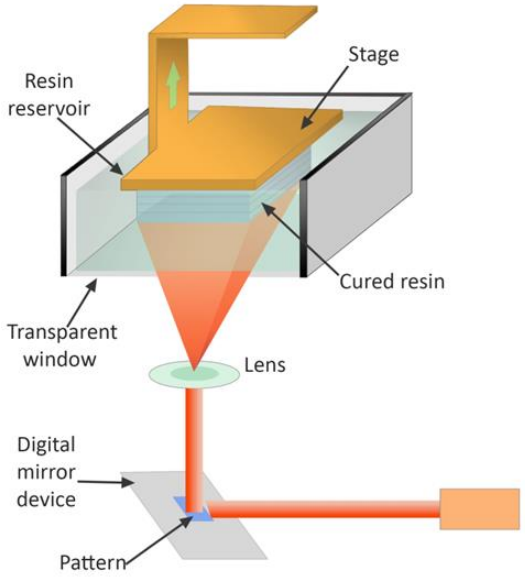

Figure 2-7. Schematic of Digital Light Processing Set-up [70].

2.6 3D printing of HIPE

The combination of 3D printing and high internal phase emulsion (HIPE) was reported for porous structures. For example, Sears et al. described a new Solid Freeform Fabrication (SFF) technology (a similar method to FDM) capable of printing photocurable emulsion inks to form porous polyHIPE foams with hierarchical porosity. In this method, a HIPE material is deposited layer-by-layer using an open-source 3D printer equipped with a syringe and motor-actuated plunger. Emulsion inks are rapidly cured after deposition by constant UV irradiation to form high porosity constructs [5]. Susec et al. [6] used a w/o HIPE with 80 wt% droplet and UV polymerizable continuous phase to print a hierarchically porous material by a DLP printer, which resulted in a monolithic porous structure with an average pore size of 2–4 μm . Cooperstein et al. combined the DLP printer and o/w HIPE to fabricate composite conductive monoliths, made of sintered silver nanoparticles and UV curable oil droplets [79]. Johnson et al. created a variety of macrostructured porous 3D polyHIPE architectures including lines and tubular structures with scanning and projection microstereolithography by photopolymerization of acrylate-based HIPE [80].

As it has been noted in the above mentioned reports, there are some limitations for 3D printing of HIPEs by the UV streolithography technique. The aqueous phase in the emulsion can scatter the light emitted by a LED lamp or laser. For

this, Cooperstein et al. has suggested to perform printing with a layer thickness below 30 µm to limit the light scattering, and therefore have sufficient UV polymerization but they have not mentioned the resolution of their printing [79]. Controlling the voxel-size (the size of the smallest sampled 3D element in 3D space) and therefore the final resolution by limiting the penetration depth of the illumination beam is another aspect that has been considered by using UV light absorber. However, they didn't describe the accuracy of their printing and the differences between the pre-defined CAD design and the resulted print [81]. It also has been shown that cured polyHIPEs can act as a scatterer for the UV light, especially in the intersections area, thus lines at the intersections are printed three-fold fold thicker than the other lines in a grid pattern [80].

Controlling the feature size of a printed liquid depends on the spreading of the liquid on the surface; in other words, when a liquid is deposited onto a surface, the configuration is predominantly determined by its surface-wetting properties. Typically, a small contact angle is advantageous to obtain good adhesion to a surface, but this condition allows the liquid to spread and form relatively large and thin features. On the other hand, if the liquid does not wet the surface, a large contact angle will form, allowing the formation of small drop features. But, these printed droplets may adhere poorly to the underlying surface [82]. The effect of surface-wetting properties for HIPE have not yet been explored.

2.7 Conclusion

The efforts in producing porous polymers with well-defined porosities grow continuously year to year. Emulsion templating is a method that use a colloidal system for simultaneous polymerization and porosity induction. High internal phase emulsion (HIPE), a type of emulsion templating with more than 74% internal phase volume, is known for creation of a highly porous, interconnected structure, in which the architecture can be tightly controlled.

Polymer monoliths are being researched more intensely in the past years due to increased demand for such type of materials biomedical applications and separation systems. Among different techniques to induce porosity in polymer monoliths, high internal phase emulsion (HIPE) with special structure exhibit several properties such as flow-independent resolution and dynamic binding capacity, low pressure drop, and high dynamic binding capacity for very large molecules. GMA is a reactive monomer that is frequently used for the preparation of functional polymers. The possibility of preparation of materials with a high level of porosity (up to 90%) and pore size tuning make GMA-based polyHIPEs good candidates for chromatographic applications.

3D printing technology is a promising approach for building chromatography columns in which the size, shape, and packing morphology is controllable,

using a tuneable porous materials such as GMA-based polyHIPE which can be chemically modified as an anion exchange chromatography media.

Chapter 3 Synthesis of polyHIPE

This chapter describes photoinitiated synthesis of highly porous acrylic polymers with controlled pore sizes and interconnectivities suitable for protein separation in column chromatography. The porous polymer was synthesized by photopolymerization of a concentrated emulsion of mixtures of GMA, EGDMA, and an aqueous phase. Figure 3-1 shows a schematic of GMA, EGDMA and the resulted poly (GMA-EGDMA). The use of GMA was motivated by the ability to carry out subsequent modification of the surface of the prepared porous column, due to the reactivity of the pendant epoxide groups [83].

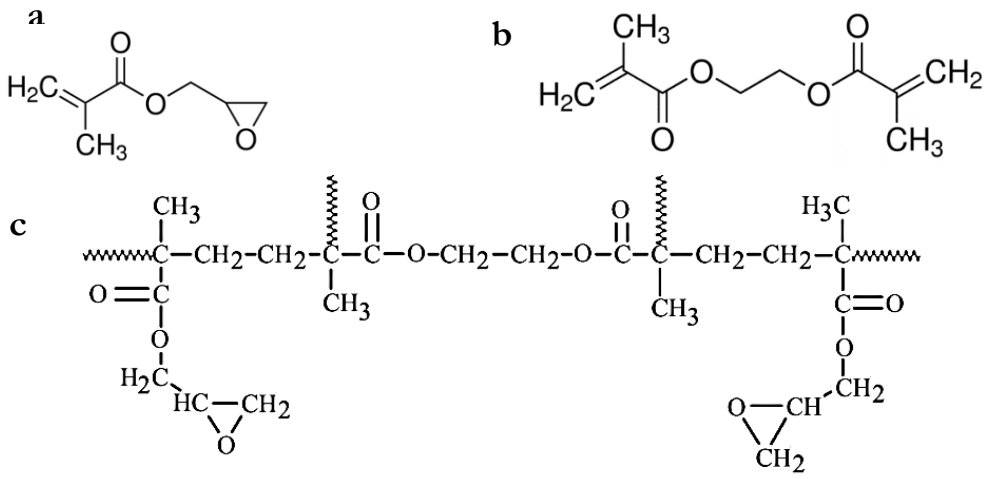

Figure 3-1. Schematic of molecular structure of a) GMA, b) EGDMA and c) poly (GMA-EGDMA).

The development and optimization of a suitable synthesis scheme for GMA-based polyHIPE were investigated and the presence of the porous structure and morphology of pores in the interior of the produced polyHIPEs with different procedures and components were verified experimentally.

3.1 Materials and Methods

3.1.1 Materials

GMA, EGDMA, Pluronic® L-81 or poly(ethylene oxide)-b-poly(propylene oxide)-b-poly(ethylene oxide) (PEO-PPO-PEO), 2,2-dimethoxy-2-phenylacetophenone(DMPA), cyclohexane, toluene and dimethylformamide

(DMF) were purchased from Sigma Aldrich (St. Louis, MO). GMA and EGDMA were passed over basic Al_2O_3 to remove inhibitors prior to use. H2O used was MilliQ grade. Other chemicals including methanol (MeOH) and calcium chloride dehydrate ($CaCl_2.2H_2O$) were supplied from Scharlau (Barcelona, Spain) and J.T.Baker (Center Valley, PA), respectively and used as received.

3.1.2 Fabrication of polyHIPE

Table 1 lists the emulsion compositions and conditions of emulsion preparation of the HIPE systems discussed in this chapter. The polyHIPEs formation procedure was adapted from a method described by Gokmen et al. [24]. An external ("oil") phase in total around 10 mL volume was prepared consisting of GMA and EGDMA as monomers, Pluronic®L-81 as the surfactant, DMPA as the initiator. A separate aqueous solution was prepared, in a 100 ml beaker, consisting of 90 ml water with an excess of $Cacl_2.2H_2O$ (1.3% w/w of aqueous phase) as an electrolyte.

The general polyHIPE synthesis procedure was as follows: The external continuous oil phase formulation comprised GMA monomer (1.53 ml), EGDMA (1.02 ml), surfactant (Pluronic® L-81, 0.5 ml) and initiator (DMPA, 100 mg) mixed in a 50 mL flask using an overhead D-shaped impeller. 10.8 ml

of an aqueous solution ($CaCl_2.2H_2O$, 1.3% w/w) were then added dropwise using a syringe pump under constant stirring at 350–400 rpm. Once addition was complete, stirring was continued (10 minutes) to ensure complete mixing of the HIPE. At this point, the HIPE was removed from the flask and transferred to a glass mould. Photopolymerization of the mixture was carried out by a UV-Handlamp (Dr. Hönle AG UV Technology, Gräfelfing, Germany) with 315–400 nm wavelength and 250 mW/cm² intensity. The distance between the lamp and the sample was 10-15 cm. The UV-exposure time was approximately 10 min. The obtained polymer was washed on a glass filter with warm H_2O and extracted in a Soxhlet apparatus with methanol for 24 h, then dried in a freeze dryer (Labconco, Kansas City, MO) at -47°C and 0.070 mBar overnight.

3.1.3 Physical Characterization

Morphological features of the polyHIPEs were investigated by scanning electron microscope (SEM), using a high-resolution JEOL JSM 7000F field emission SEM (JEOL USA Inc., Peabody, MA) in the Department of Mechanical Engineering at the University of Canterbury. The samples were coated with gold using a sputter coater for three periods of 60 seconds and viewed using an accelerating voltage of 15 kV. The open source image processing software package ImageJ version 1.46 (available at https://imagej.nih.gov/ij/) was used to manually determine the pore and window

sizes of approximately 100 pores per sample. As suggested by Ross et al., the observed average value of the pore diameter was multiplied by 2/(31/2) as a statistical correction factor to obtain a more accurate value of pore and window sizes. This is achieved by evaluating the average of the ratio of the equatorial value of pore diameter and the diameter value measured from the SEM image. [42]. Cameron et al. showed that photo-polymerized HIPEs are a direct template of their parent emulsions, with theoretical porosity (calculated from nominal oil/water ratio) matching well with experimental porosity values (from mercury porosimetry) [54]. Accordingly, we assumed that the porosities of the prepared polyHIPEs were the same as their intended values during HIPE preparation.

Specific surface area was measured with a Micromeritics Gemini VI Surface Area and a Porosity Analyzer (Micromeritics Instrument Corporation, Norcross, GA,) by applying the Brunauer–Emmet–Teller (BET) and Barrett-Joyner-Halenda (BJH) methods to N_2 adsorption/desorption isotherms. Prior to analysis, all samples were degassed for 24 h at 100°C in a Micromeritics FlowPrep 060 Sample Degas System (Micromeritics Instrument Corporation).

3.2 Results and Discussion

3.2.1 Control of the morphology of polymer particles

In the previous chapter, I briefly discussed creating porous structures with the dispersed phase being water and the external continuous phase being a hydrophobic monomer, which can be polymerized to give a porous polymer. These materials can have a porous structure, which consists of closed cells and/or open cells, with the latter referring to a system in which the pores are interconnected. In section 2-1-3, the parameters that can affect pore size, shape and architecture of polyHIPEs according to the literature have been discussed. In the following sections, the morphology and porous structures of GMA-based polyHIPEs prepared with different procedures and components are described, providing a suitable synthesis method for subsequent work.

Table 3-1. Compositions, conditions of HIPE preparation and morphological characteristics of GMA-based polyHIPEs.

Sample	Differentiation in Oil Phase		Internal phase ratio	Mixing procedure	<D>[a] (μm)	SSA[e] (m^2/g)
	Surfactant Concentration (%V)	Porogen				
G-E1-400(78)	17	-	0.78	IKA (400 rpm)	2.4±1.1	13.1± 1.1
SG-E1-400(78)	17	-	0.78	IKA(400 rpm) + Probe sonicator	1.5±0.6	14.5± 0.1
G-E1-2800(78)	17	-	0.78	Silverson (2800 rpm)	5.5±3.4	11.4± 0.5
G-E1-4000(78)	17	-	0.78	Silverson (4000 rpm)	6.5±3.8	9.3±1. 5
G-E2-400(78)	21	-	0.78	IKA (400 rpm)	-	14.7± 0.1
SG-E2-400(78)	21	-	0.78	IKA(400 rpm) + Probe sonicator	-	17.6± 2.3
G-E2-2800(78)	21	-	0.78	Silverson (2800 rpm)	3.1±1.1	11.9± 1.5
G-E3-4000(78)	25	-	0.78	Silverson (2800 rpm)	3.8±2.1	10.5± 0.3
G-E1-400(90)	17	-	0.9	IKA (400 rpm)	-	10.9± 1.2
G-E1-4000(90)	17	-	0.9	IKA (400 rpm)	10.9±3. 9	9.8±0. 6
G-E1(C)-400(78)	17	Cyclohexane	0.78	IKA (400 rpm)	22.1±7. 1	6.95± 0.29
G-E1(T)-400(78)	17	Toluene	0.78	IKA (400 rpm)	18.8±2. 3	7.2±0. 68
G-E1(D)-400(78)	17	DMF	0.78	IKA (400 rpm)	10.3±1 5.5	9.6±1. 05

[a] Average pore diameter. [b] Specific surface area.

3.2.2 Stirrer Variation

A Silverson mixer (Silverson Machines, Inc., East Longmeadow, MA) with an interchangeable tubular mixing unit was used for preparation of HIPEs. For comparison of stirrer variation on HIPE formation, an IKA RW 20 DZM as well as the combination of IKA RW 20 DZM with a Probe Sonic Ruptor 400 (Omni International, NW Kennesaw, GA) for 30 s, at 10/5 s pulses, 100% intensity were also used. Both stirrers were set to the same stirring time (40 min) and with the same length of addition time (30 min) but with different stirring speeds, 4000 rpm and 2800 rpm for the Silverson mixer and 400 rpm for the IKA. For the combination of IKA overhead stirrer and Probe Sonic Ruptor, the sample (SG-E1-400(78)) was prepared by the same procedure as for G-E1-400(78), then further homogenised with the Probe Sonic Ruptor to achieve smaller droplet sizes. SEM images and pore size distribution measured by ImageJ of polyHIPEs formed by different procedures are shown in Figure 3-2. It is obvious from SEM images and Table 3-1 that the smallest pores were associated with the most uniform pore size distribution and highest SSA observed for SG-E1-400(78). Also for comparing the effect of stirrer type, G-E1-400(78) had smaller pores and higher SSA than the polyHIPEs made using the Silverson stirrer. In addition, the range of pore size distribution of G-E1-400(78) was narrower than the range of pores in G-E1-2800(78) and G-E1-4000(78). These show that the

best procedure amongst the other tested procedures for making small pores with a narrow pore size distribution is a combination of the IKA propeller stirrer and the Probe Sonic Ruptor, yet the IKA propeller broke water droplets more intensely than the Silverson, contrary to that expected with the lower intensity of mixing. Comparison between G-E1-2800(78) and G-E1-4000(78) shows that although G-E1-2800(78) had smaller average pore size and its pore size distribution is insufficient intensity and tailed toward larger pores. This suggests that 2800 rpm is not enough intense for making small and uniform water droplets in the emulsion.

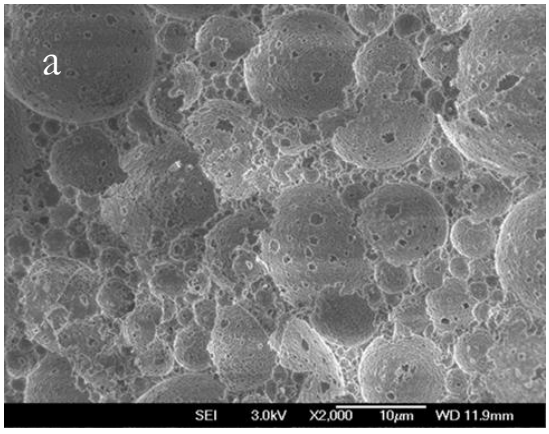

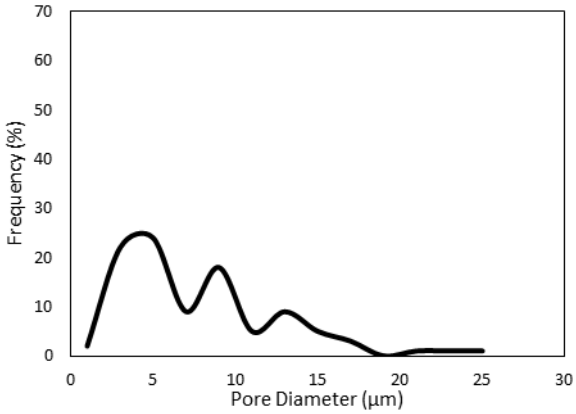

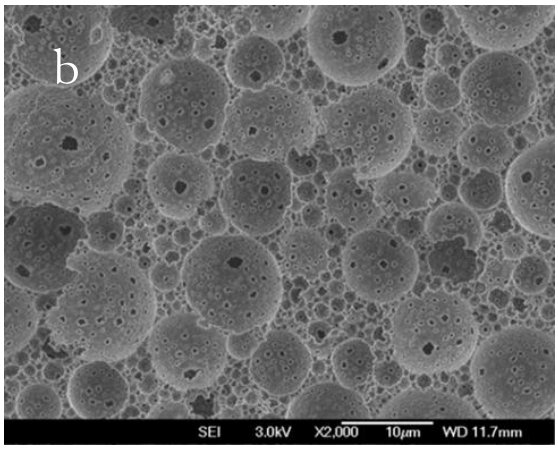
b
SEI 3.0kV X2,000 10μm WD 11.7mm

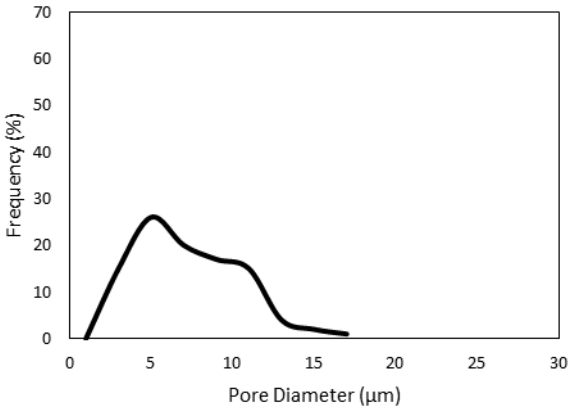
70
60
50
40
30
20
10
0
Frequency (%)
0
5
10
15
20
25
30
Pore Diameter (μm)

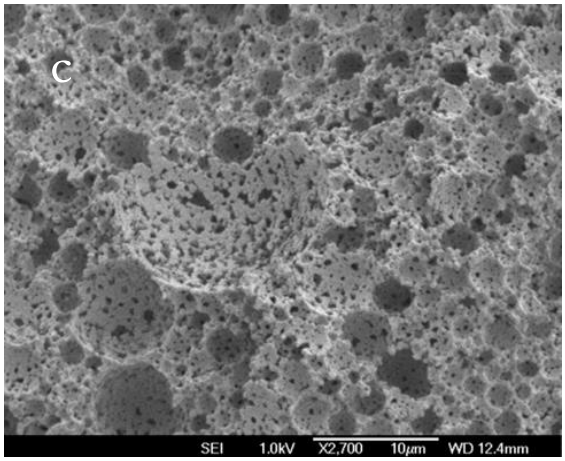
c
SEI 1.0kV X2,700 10μm WD 12.4mm

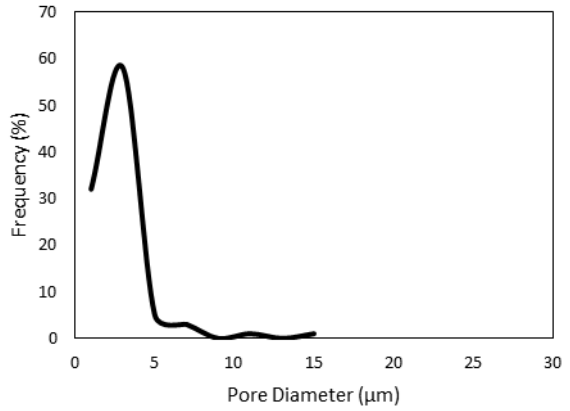
70
60
50
40
30
20
10
0
Frequency (%)
0
5
10
15
20
25
30
Pore Diameter (μm)

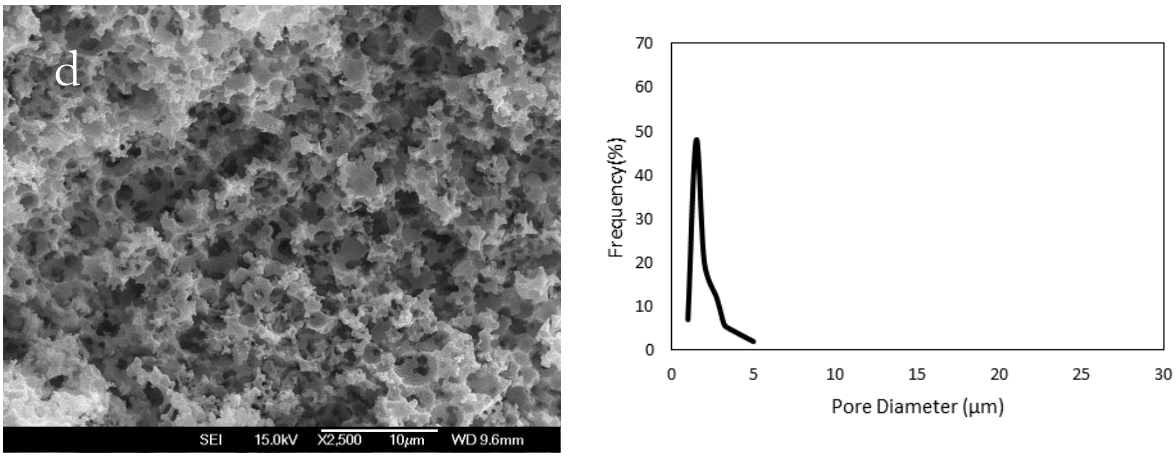

Figure 3-2. SEM Images of produced ployHIPs with different stirring conditions a) G-E1-2800(78), b) G-E1-4000(78), c) G-E1-400(78) and d) G-E1-400(78)-S.

3.2.3 Surfactant Concentration

The concentration of the surfactant in the monomer phase was found to be critical to the formation of a stable polymer foam [84, 85]. Surfactant levels relative to the total oil phase between 20 and 50% were considered to produce open-cell foams with an entirely interconnected microstructures [17]. According to these, Ploranic L-81 (as the surfactant) with three different concentrations including 17%, 21% and 25% relative to the oil phase were chosen to be added at two different stirring intensities with the Silverson mixer to see how it would change pore size and distribution. Electron micrographs of

prepared polyHIPEs are shown in Figures 3-3a-c. As can be seen, there is not a dramatic difference between polyHIPEs in the creation of interconnectivity (windows) between pores as a rsesult of increasing the surfactant concentration and it seems it is more dependent on the intensity of mixing.

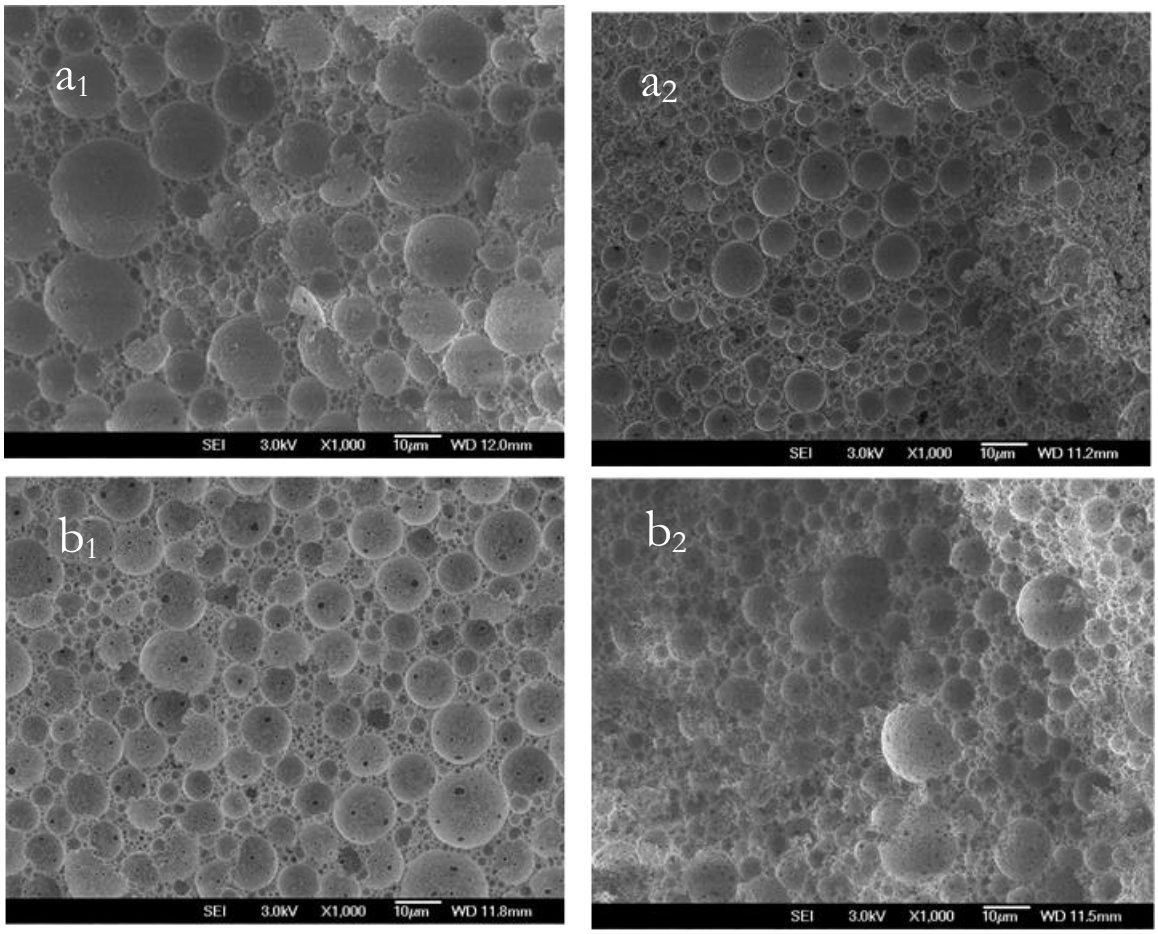

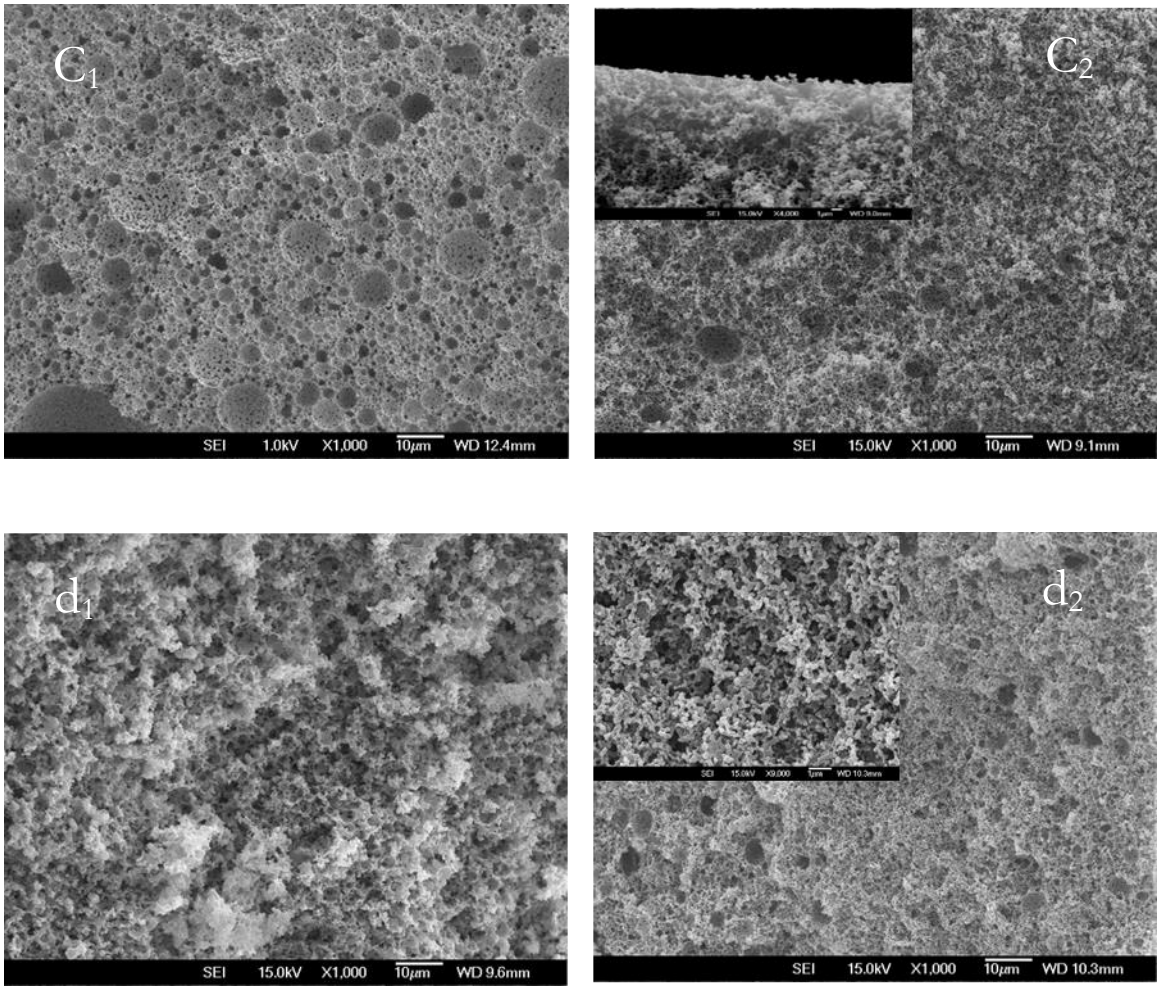

Figure 3-3. SEM images of GMA/EGDMA polyHIPEs with different concentrations of Pluranic L-81: a1) G-E1-2800(78), a2) G-E2-2800(78), b1) G-E1-4000(78), b2) G-E2-4000(78), c1) G-E1-400(78), c2) G-E2-400(78) d1) SG-E1-400(78) and d2) SG-E2-400(78).

For better comparison, figure 3-4 shows average pore size distributionfor the above shown SEM images except 6c and d. It is clear that surfactant with the lowest concentration (17%) produced polyHIPEs with larger average pore size,

5.48±3.4 µm for 2800 rpm and 6.47±3.8 µm for 4000 rpm of mixing intensity. It also shows that 17% surfactant in the emulsion led to a wider pore size distribution and tailing of the distribution towards larger pore sizes for both stirring conditions. These two effects have been associated with droplet coalescence in the emulsion [54]. The presence of a higher percentage of surfactant in the prepared HIPE resulted in smaller pore size and narrower pore size distribution at all stirring intensities (400, 2800 and 4000 rpm). Increasing the surfactant concentration reduced the monomer wall around droplets in the emulsion that accompanied with stirring lead to smaller and more open pore cells. It is noticeable that pore size distribution is wider and it also tailed to larger pore sizes around 16 µm using the most intense mixing (4000 rpm) and highest amount of surfactant (25%). This could be due to decreasing of the wall thickness with more intense mixing as well as higher surfactant concentration that lead to the ripening of droplets and making bigger droplets in the emulsion. Measurements of pore size and pore size distribution of G-E2-400(78) and SG-E2-400(78) were impossible due to its structure. However, BET results show the highest SSAs among other polyHIPEs which indicated smaller pores and a high degree of interconnectivity are for these samples.

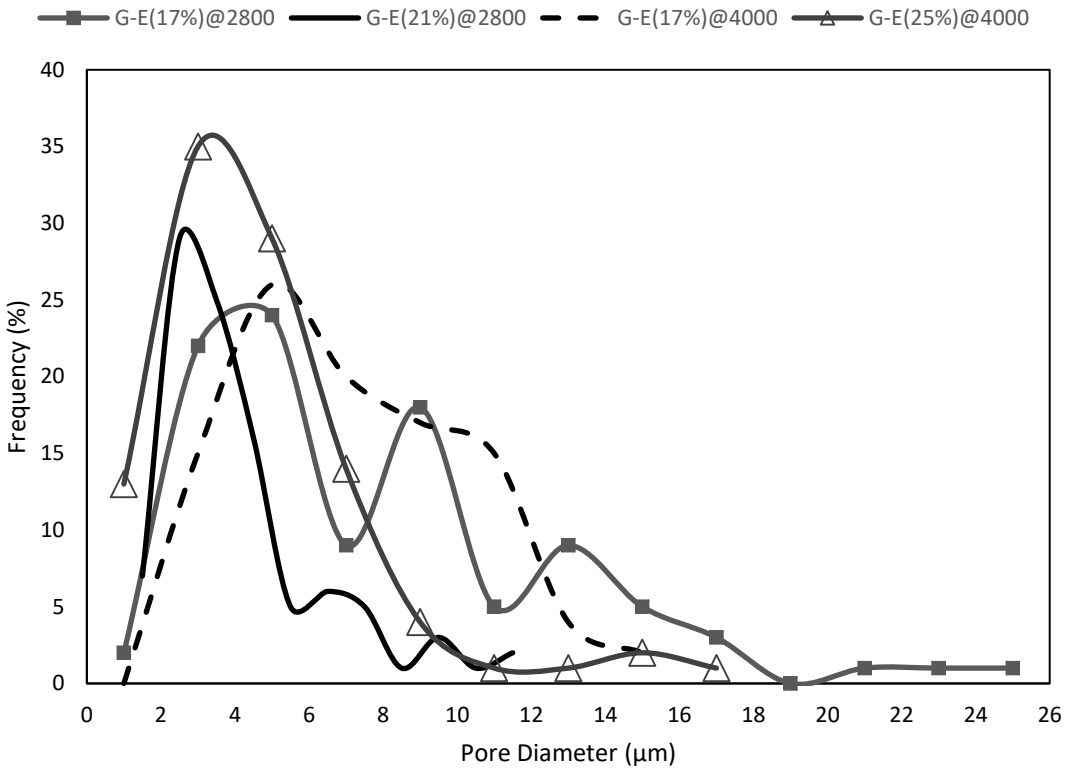

Figure 3-4. Average pore size distribution plots for G-E polyHIPEs materials prepared with different surfactant concentration at two different stirring conditions.

3.2.4 Effect of internal phase volume ratio

As mentioned in different references [17, 35, 84] the ratio of aqueous phase to oil phase is one of the main factors that influence the porous structure in polyHIPEs. Based on this, polyHIPEs with higher internal phase volume (90%) were produced to see how the morphology of foams change. Figure 3-5

compares the structure of G-E1-4000(78) with G-E1-4000(90) as well as G-E1-400(78) with G-E1-400(90), where all had the same preparation conditions but differing aqueous volumes. Figure 3-5(b) also provides a comparison of the pore and window size distribution calculated using ImageJ for G-E1-4000(90) and G-E1-4000(78), as it was not possible to measure window and pore sizes for G-E1-400(90) due to its structure. It can be seen from Figure 3-5(b), average pore diameter (<D>) and interconnecting window diameter (<d>) increased with an increasing volume of the aqueous phase in the HIPE. The average interconnecting window diameters (<d>) for G-E1-4000(90) and G-E1-4000(78) equal 0.5±0.2 and 0.3±0.1, respectively. Barbetta et al. introduced the ratio of <d>/<D> as a reflection of the degree of interconnectivity that is strictly connected with the degree of thinning of the monomer film separating water droplets [41].

A)

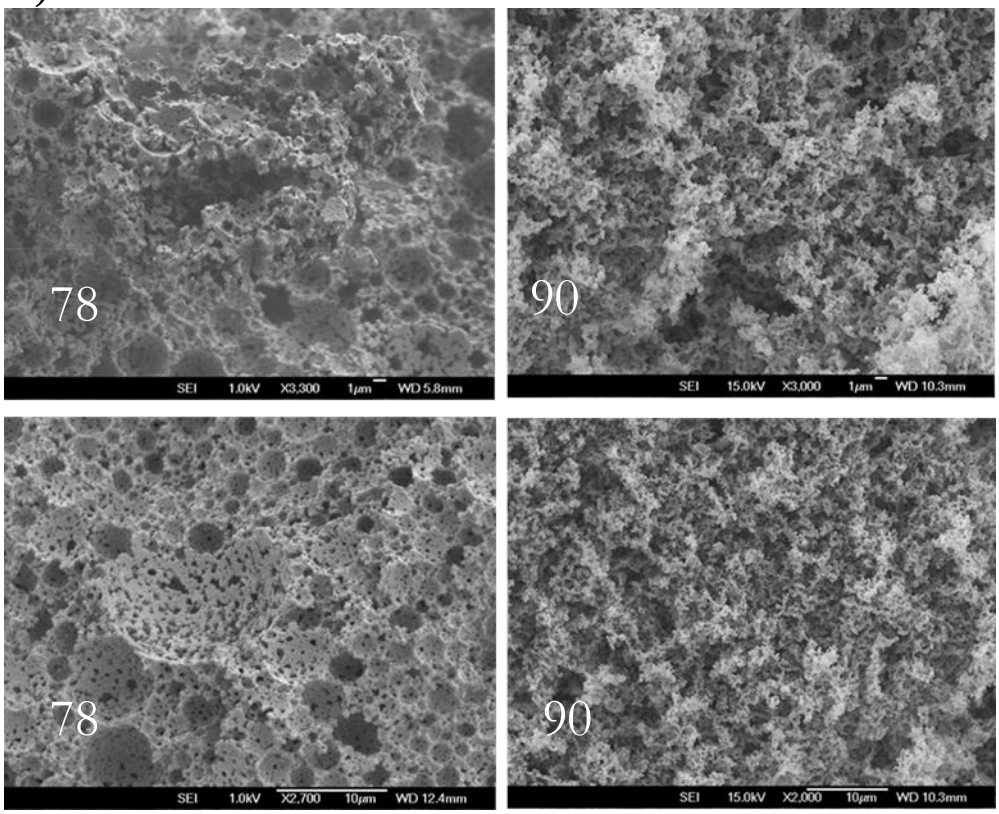
78
SEI 1.0kV X3,300 1μm WD 5.8mm
90
SEI 15.0kV X3,000 1μm WD 10.3mm
78
SEI 1.0kV X2,700 10μm WD 12.4mm
90
SEI 15.0kV X2,000 10μm WD 10.3mm

B)

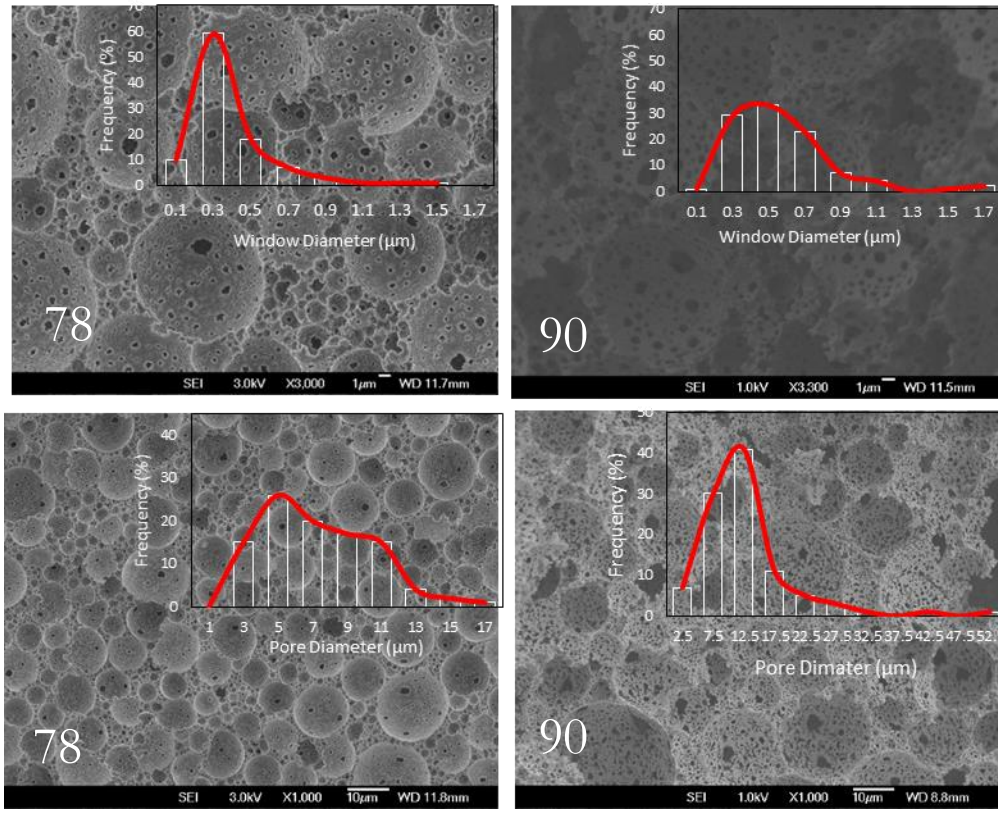

Figure 3-5. SEM images of A) G-E1-400(78) with G-E1-400(90) and B) G-E1-4000(78) with G-E1-4000(90) in different magnifications.

This ratios for G-E1-4000(90) and G-E1-4000(78) equal 0.045 and 0.050, respectively, which shows increasing the amount of internal phase in the emulsion decreases the degree of interconnectivity. This is also supported by a decrease in the specific surface area as a result of increasing the internal phase ratio.

3.2.5 Addition of porogen

Hainey et al. [77] reported that one of the factors that could increase the surface area of polyHIPEs is the addition of an inert diluent (porogen) to the monomer phase. Because applications of porous materials as a stationary phase in chromatography require high surface areas, we decided to investigate the influence of the porogen on the porous characteristics and morphology of the resultant polyHIPE foams. In fact, introducing porogenic solvents during the synthesis of polyHIPE materials affects the formation of secondary pores in the polymer matrix due to phase separation in the polymer matrix during polymerization [86]. Cameron et al. showed that the nature of the solvent has a profound influence on the foam morphology on both a large and small scale [87]. They reported that as the solubility parameter (δ) of the solvent approaches that of the polyHIPE, the structure produced contains a larger number of small microparticles, which results in a higher surface area. For a good porogen, we needed a solvent with a solubility parameter close to that of poly(GMA-co-EGDMA). According to Stanislav Dubinsky et al. [88], the solubility parameter of GMA-EGDMA is around 24 $MPa^{1/2}$. Three solvents with different solubility parameter, including cyclohexane (δ=16.8 $MPa^{1/2}$), toluene (δ=18.2 $MPa^{1/2}$) and DMF (δ=24.8 $MPa^{1/2}$) were chosen to investigate the effect of porogen on morphology and SSA of GMA-based polyHIPEs. Figure 3-6 shows SEM

images as well as pore size distributions of prepared polyHIPEs produced with a (1:1) volume ratio of monomer phase to porogen.

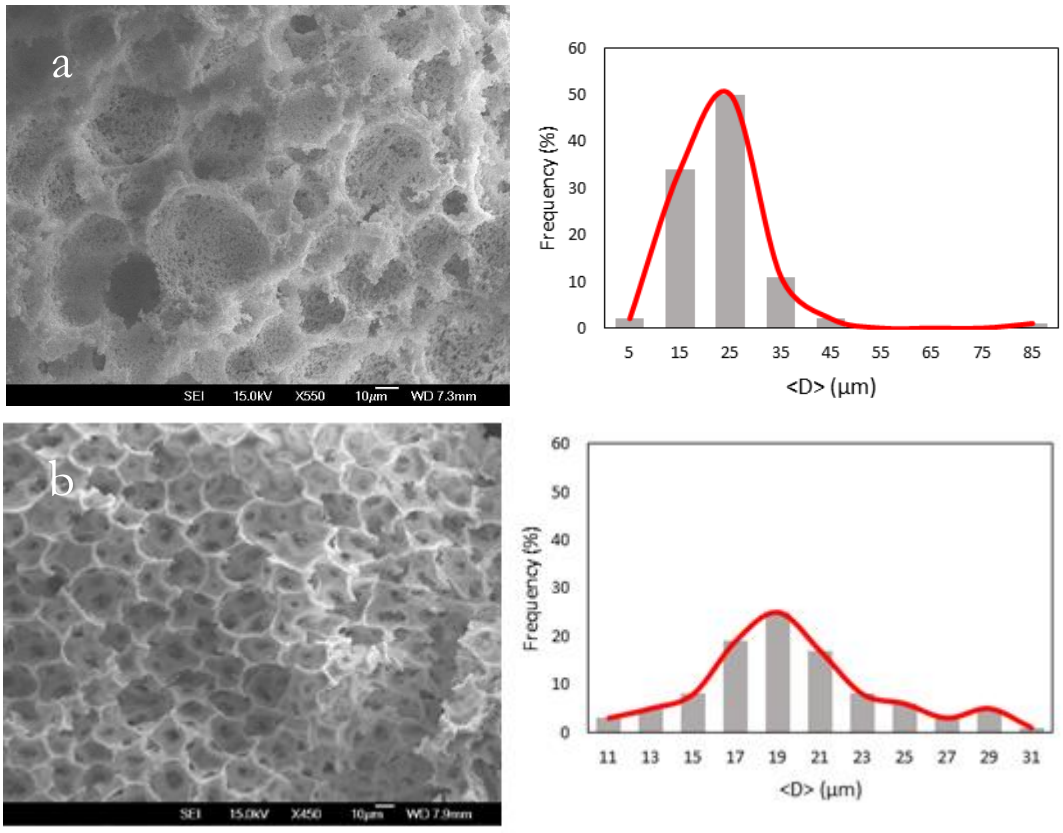

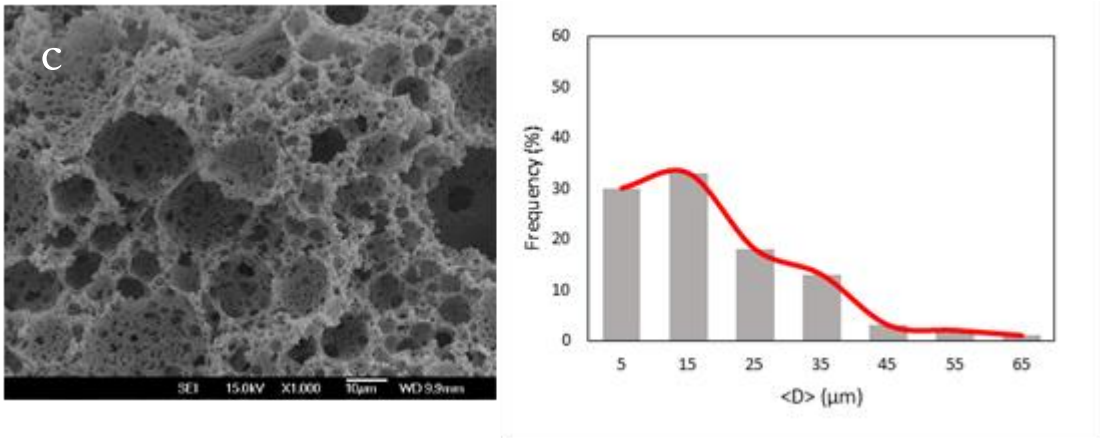

Figure 3-6. SEM images on left and pore size distribution on right a) G-E1-400(C), b) G-E1-400(T) and c) G-E1-400(D).

As it can be seen, the porogen (DMF) with a solubility parameter closest to that of GMA-EGDMA polyHIPE produced smaller pores in comparison with the other prepared polyHIPEs containing porogens with greater differences in solubility parameters from that of GMA-EGDMA. During polymerization in the presence of cyclohexane and toluene, because of greater differences between the values of solubility parameters and thus greater thermodynamic incompatibility between porogens and the polymer, phase separation may occur at the gel point, leading to the formation of larger polymer clusters and the formation of larger pore sizes. Despite the results reported in the literature [77, 86, 87], BET results in Table 1 show that addition of none of the porogens tested led to a higher specific surface area because of the relatively large pore sizes produced in presence of porogenic solvents.

3.3 Conclusions

Polymerization of the continuous phase of HIPEs leads to the successful production of several polyHIPE materials, proving HIPE to be a versatile approach for the production of highly porous polymers from acrylate monomers. It was shown that the IKA propeller combined with a Probe Sonic Ruptor had the best performance amongst the IKA propeller alone, and the Silverson impeller for making the most uniform emulsion and smallest droplets. Addition of 21% surfactant relative to the oil phase resulted in more open and smaller pores with a more uniform pore size distribution. The presence of porogenic solvents and increasing the internal phase ratio led to larger pores and lower specific surface area. According to these results, SG-E2-400(78) was chosen as the main sample for subsequent work.

Chapter 4 Improvement of mechanical properties of GMA-based polyHIPE

As mentioned in Chapter 1, polyHIPEs have been investigated for use in numerous applications. However, the use of polyHIPEs is limited in practice by their mechanical properties, especially low crush strengths (around 0.03 MPa [55]), chalkiness and brittleness. There have been several attempts to increase the toughness of polyHIPEs, including addition of nanoparticles for Pickering emulsion templating or nanocomposites [56, 89], introduction of reinforcing materials such as pullulan [55], introduction of elastomeric co-monomers such as 2-ethylhexyl acrylate (EHA) or methacrylate (EHMA) [67, 90], dicyclopentadiene (DCPD) [91] and methyl methacrylate (MMA) [92], hypercrosslinking reactions using radical initiators [93, 94], reversible addition-fragmentation chain transfer (RAFT) [95], thiol-ene (and thiol-yne) click chemistry [96], and through the use of concentrated emulsions [97]. Whilst these

approaches can improve the mechanical strength of polyHIPEs, other characteristics are compromised. For example, polymerization of Pickering HIPEs normally leads to closed-cell foams with a larger pore size than conventional polyHIPE [98, 99]. Increasing the amount of elastomeric monomers such as EHA decreases the glass transition temperature of the polymer [67, 90]. The use of the RAFT reaction results in residual catalysts, while residual thiol functionalities remains in thiol-ene chemistry and both of these reactions are slow [100]. Post-polymerization hypercrosslinking requires additional processing. Thus, improvements in the mechanical properties of acrylic polyHIPEs are necessary to enable the production of tough supermacroporous materials.

This chapter describes the attempts to improve the mechanical properties of GMA-based polyHIPEs in terms of toughness with fewer drawbacks by using crosslinkers or co-crosslinkers of different molecular weights. To this end, several poly(ethylene glycol) dimethacrylate (PEGDMA) crosslinkers were considered. It is shown that the elastic modulus and crush strength of GMA-based foams can be increased by the use of higher molecular weight crosslinkers. The effect of the molecular weight of the crosslinker or co-crosslinker on the microstructure of the polyHIPEs was also assessed.

4.1 Experimental

4.1.1 Materials

GMA, EGDMA (MW 198 g mol^{-1}), triethylene glycol dimethacrylate (TEGDMA, MW 286 g mol^{-1}), PEGDMA (average MW 550 g/mol), Pluronic® L-81 and DMPA were purchased from Sigma Aldrich. GMA, EGDMA, TEGDMA and PEGDMA were passed over basic Al_2O_3 to remove inhibitors prior to use. MilliQ grade water was used throughout experimental work. Methanol and calcium chloride dihydrate were purchased from Scharlau (Barcelona, Spain) and J.T. Baker (Center Valley, PA), respectively, and used as received.

4.1.2 METHODS

4.1.2.1 Fabrication of PolyHIPE

PolyHIPEs were prepared with different compositions of crosslinkers according to the method described in Section 2.1.3 for G-E1-400(78) sample.

All resulting polyHIPEs contained 60% v/v GMA and 40% v/v crosslinker. Different crosslinker compositions were used in the HIPE formulations, including the three pure crosslinkers, as well as different mixtures of EGDMA/PEGDMA and TEGDMA/PEGDMA. As the reference sample was chosen to be G-E1-400(78), the polyHIPEs are identified in this chapter according to the crosslinker(s) used, i.e. EGDMA(E), TEGDMA(TE),

PEGDMA(PE), and the v/v% of co-crosslinkers in the crosslinker mixture. Thus, G-E(80)/PE(20) indicates a polyHIPE containing GMA, 80% v/v EGDMA and 20% v/v PEGDMA.

4.1.2.2 Physical Characterization

Morphological features of the polyHIPEs including pore and window sizes as well as specific surface area were investigated as described in Section 2.1.4. Degree of openness as the ratio of open surfaces (So) to the total surface of a pore (S_p) was calculated according to the method reported in Pulka et al. [101]. To determine S_o, the average diameters of interconnecting windows were used to calculate the average area ($\pi(\frac{D_w}{2})^2$). This was multiplied by the number of visible interconnecting windows (N), then by 2 as the pore had been cut in half, and by the statistical correction factor as it is not known where the cavity had been bisected. Then, the degree of openness is calculated using Eq. 1.

$$Degree\ of\ Opennes = \frac{N*2*\frac{2}{\sqrt{3}}*\pi(\frac{D_w}{2})^2}{\pi D_p^2} \quad (1)$$

Interfacial tension at the water-oil interface was measured by the pendant drop method using a CAM 200 instrument (KSV instruments Ltd, Helsinki, Finland) and the built-in software CAM 2008 for data processing. For measurements at the interface with the oil phase, a 5–7 µL droplet of aqueous

phase was left hanging from the syringe needle in 2 mL of oil phase within a cuvette. The interfacial energies were derived by fitting the droplet shape by the Young–Laplace method.

Viscosity of the oil phase formulations was measured with a Haake viscometer RV20 with the measuring system CV100. The system consists of a rotating vessel filled with the liquid under study and a cylindrical sensor of Mooney-Ewart type (M15), placed in the center of the vessel. The uncertainty of the viscosity determination was 0.1%. The temperature was maintained constant (20±0.01°C) using a water bath surrounding the vessel. The densities of the polyHIPEs were determined from weight and volume measurements.

The compressive stress–strain curves of the polymeric foams were obtained by testing cylindrical specimens with a MTS Criterion Electromechanical Test System Model C43.104 (MTS, Eden Prairie, MN) equipped with a 500 N load cell. The cylindrical specimens had a diameter and height of 11 mm. Tests were performed at a constant speed of 1.0 mm/min until material failure. A minimum of 15 samples per polyHIPE material were tested. The Young's modulus of the samples was determined from the slope of the initial linear region of the stress–strain curves, while the maximum crush strength was obtained from the maximum compressive stress the sample sustained before fracture.

4.2 Results and Discussion

In this section the improvement of the mechanical properties of GMA-based polyHIPEs and reducing the reported brittleness and chalkiness of these materials is discussed. An investigation was carried out to determine the influence of using crosslinking or co-crosslinking monomers of differing molecular weights on the Young's modulus, crush strength, pore diameter, window diameter and specific surface area of GMA-based photo-polymerised polyHIPE materials. To this aim, three different ethylene glycol-based dimethacrylate crosslinkers with different molecular weights were tested. The structures of GMA and all crosslinkers are shown in Schematic 4-1. All other factors, including water/oil phase ratio, surfactant, and initiator were kept constant in all experiments.

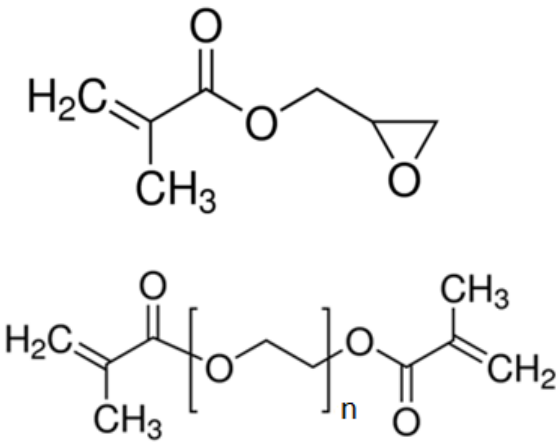

Schematic 4-1. Molecular structure of A) GMA and B) EGDMA (n=1), TEGDMA (n=3) and PEGDMA (n=8).

4.2.1 Poly(HIPE) structure

The final structure of PolyHIPE depends on the form and stability of the parent emulsion and parameters such as curing time and temperature. Tuning the parent emulsion to control emulsion parameters, such as surfactant concentration, interfacial tension and the viscosity of oil phase and aqueous phase and to produce a stable emulsion, with defined pore size, shape and architecture is discussed further in the literature [26, 35, 42]. For investigation of fabricated polyHIPEs morphology, the microstructure was visually observed by scanning electron microscope. The obtained SEM images for polyHIPEs are shown when pure crosslinker was employed in Figure 4-1(a) and in presence of the combination of crosslinkers in Figure 4-1(b).

a)

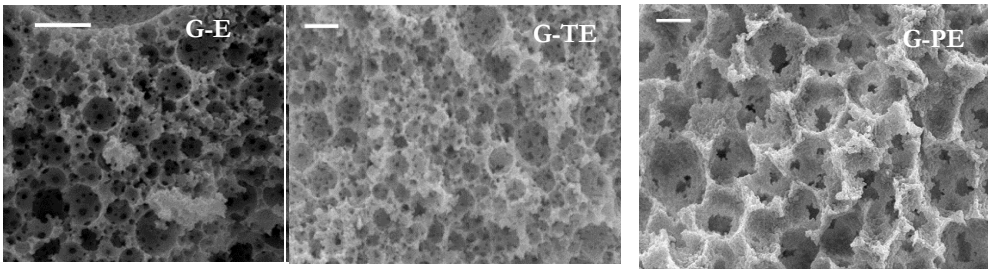

b)

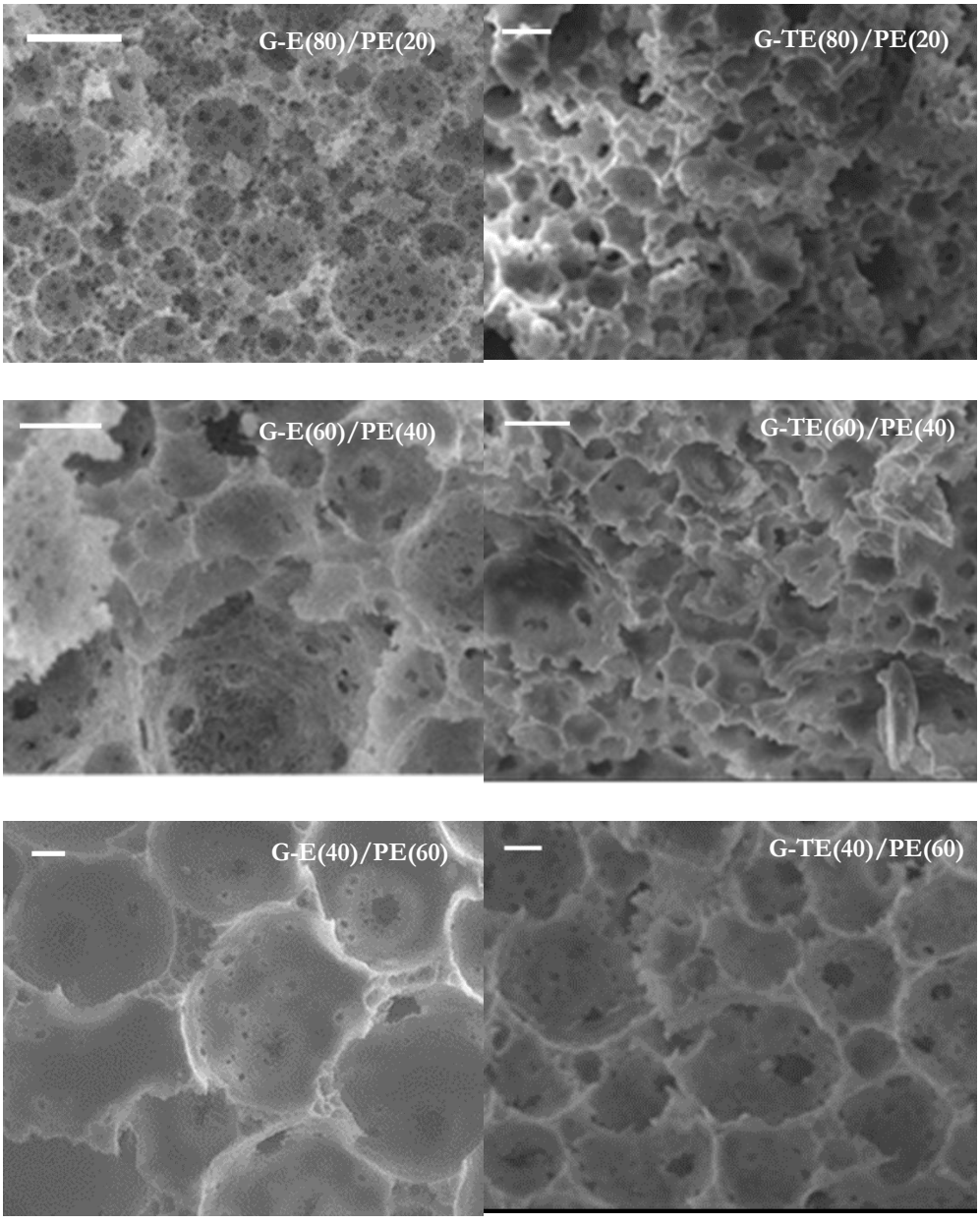
G-E(80)/PE(20)
G-TE(80)/PE(20)
G-E(60)/PE(40)
G-TE(60)/PE(40)
G-E(40)/PE(60)
G-TE(40)/PE(60)

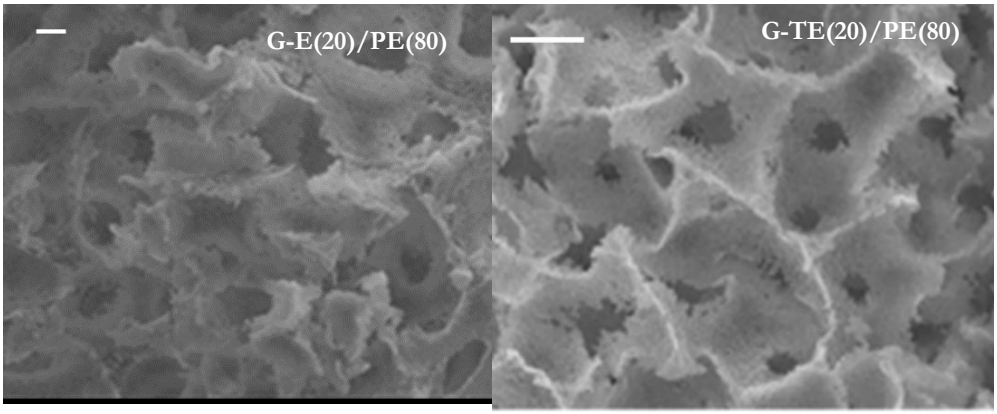

Figure 4-1. SEM images of PolyHIPE materials prepared with crosslinkers with different molecular weights a) pure crosslinkers, b) mixture of crosslinkers. All the scale bars represent 10 μm.

In all cases, the well-known macroporous polyHIPE structure consisting of pores and interconnected windows was obtained. As can be seen, the pore morphology depended upon the particular crosslinker or crosslinker combination used, resulting in either the formation of small, interconnected polyhedral pores or larger, spherical pores with a lower degree of interconnectivity. It is also possible to observe that crosslinkers with higher molecular weight produced polyHIPEs with larger average pore and window sizes. A quantitative analysis of the morphology of the polyHIPEs shown in Figure 4-1 is presented in Table 4-1, as well as the results of specific surface area from N_2 adsorption, viscosity and interfacial tension measurements. In the case of pure crosslinkers (Figure 4-1(a)), the measured average pore diameter, <D>, and average window diameter, <d>, steadily increased with the molecular

weight of the crosslinker. This is particularly apparent for the G-PE sample, endowed with 3-to 4- fold higher pore and window dimensions than those of the G-E and G-TE materials. The pore size distributions, reported in Figure 4-2, show that an increase in the amount of the high molecular weight crosslinker, (PEGDMA), led to broadening of the pore size distribution with a tailing towards larger pore sizes. These two effects have been associated with droplet coalescence in the emulsion [54]. However, the specific surface areas of the foams decreased in the presence of PEGDMA but were in the range of GMA-based polyHIPEs typically reported [53]. Because of polyHIPEs relatively large pore sizes, specific surface areas of polyHIPEs are generally around 5 m^2/g.

Table 4-1. Morphological characteristics of GMA-based polyHIPEs. Top: crosslinker mixtures of G-E/PE; bottom: crosslinker mixtures of G-TE/PE.

Sample	<D>[a] (μm)	<d>[b] (μm)	DOO[c]	SSA[d] (m^2/g)	γ [e] (mN/m)	Foam Density (g/cm3)	Viscosity of Oil Phase (Pa.s)
G-E	3.3±1.2	0.5±0.2	0.26±0.02	14.7	5.8	0.20±0.03	0.0066
G-E(80)/PE (20)	4.1±1.3	0.7±0.2	0.27±0.02	6.2	4.3	0.21±0.04	0.0076
G-E(60)/PE (40)	37.1±6.9	1.4±0.5	0.18±0.08	3.5	3.7	0.23±0.07	0.0091
G-E(40)/PE (60)	45.1±7.6	5.6±1.9	0.19±0.08	3.2	2.8	0.25±0.04	0.0109
G-E(20)/PE (80)	27±7.1	7.2±0.6	0.08±0.02	3.2	2.0	0.27±0.05	0.0131
G-PE	12.7±3.2	2.1±2.6	0.05±0.02	3.2	1.5	0.28±0.06	0.0162
G-TE	3.8±1.4	0.7±0.4	0.17±0.05	5.8	5.5	0.23±0.02	0.0099
G-TE(80)/PE(20)	7.4±1.8	0.9±0.2	0.09±0.02	4.4	4.2	0.24±0.05	0.0105
G-TE(60)/PE(40)	13.9±6.9	1.8±0.6	0.05±0.02	2.7	3.2	0.25±0.03	0.0114
G-TE(40)/PE(60)	22.9±9.4	1.3±0.8	0.04±0.02	1.8	2.6	0.26±0.06	0.0126
G-TE(20)/PE(80)	14.9±4.6	4.3±1.6	0.05±0.02	1.2	1.8	0.28±0.05	0.0141
G-PE	12.7±3.2	2.1±0.6	0.05±0.03	3.2	1.5	0.28±0.06	0.0162

[a] Average pore diameter. [b] Pore diameter polydispersities. [C] Average window diameter. [d] Window diameter polydispersities. [e] Specific surface area, [f] Interfacial tension.

a

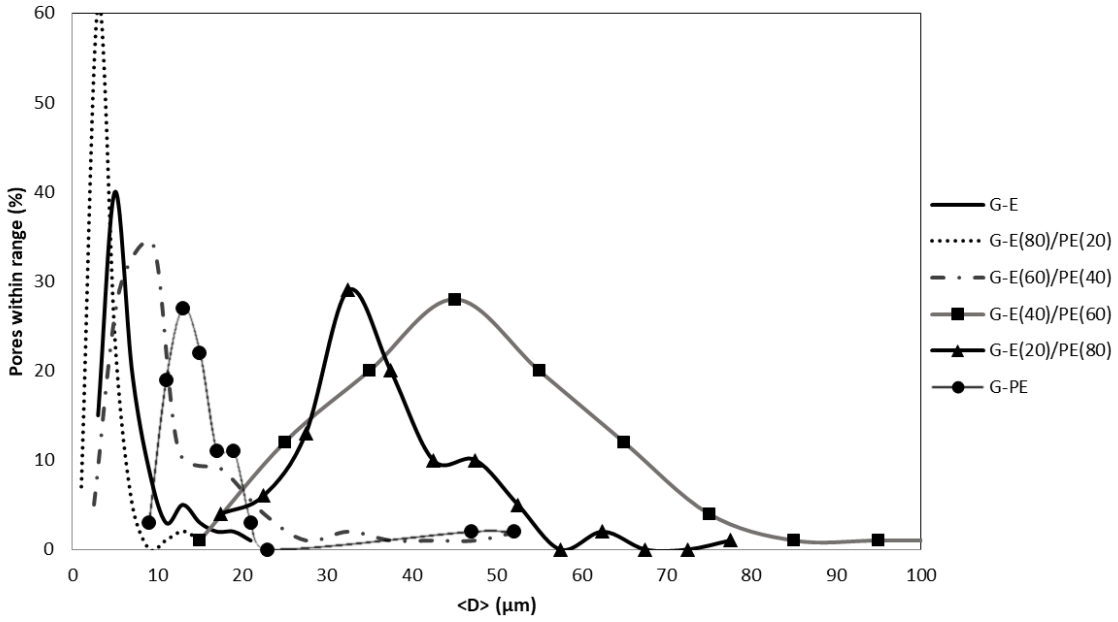
Pores within range (%)
<D> (µm)
0
10
20
30
40
50
60
70
80
90
100
G-E
G-E(80)/PE(20)
G-E(60)/PE(40)
G-E(40)/PE(60)
G-E(20)/PE(80)
G-PE

b

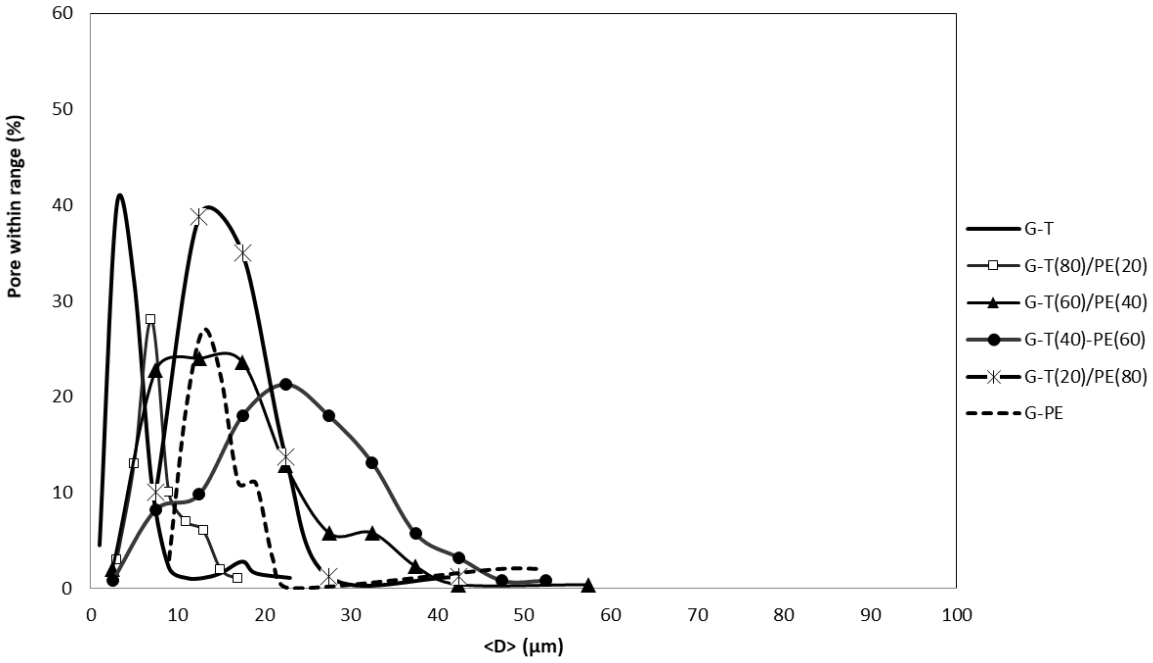

Figure 4-2. Pore diameter distribution plots for a) G-E-PE and b) G-TE-PE polyHIPEs materials prepared with different crosslinkers.

Figure 4-3 provides a better view of the effect of crosslinker on the pore and window size as well as degree of openness accompanied with the changes of interfacial tension and viscosity of oil phase. It is noticeable that the average pore and window diameter sizes reached a peak at 60% PEGDMA in both crosslinkers mixtures with increasing concentrations of PEGDMA. For both G-E-PE and G-TE-PE polyHIPEs, a higher degree of openness was observed at 0% PEGDMA and decreased with increasing percentage of PEGDMA. The final droplet size in the emulsion is the result of an equilibrium between droplet

break-up and coalescence. Highly concentrated emulsions are unstable, so the formed droplets tend to coalesce. It has been shown that the attraction between drops of the water phase significantly increases at low interfacial tension, resulting in flocculation and deformation of droplets, in turn leading to coalescence instabilities [102]. The current results confirm this trend, with the G-E and G-TE samples having similar interfacial tension of approximately 5.5-5.8 mN/m, while the G-PE polyHIPE characterized by a 3.5- to 4-fold smaller interfacial tension of 1.5 mN/m. This behavior, as well as tailing and broadening of the pore size distribution (Figure 4-2), suggests that coalescence was the main mechanism behind the increase in pore size and polydispersity with the incorporation of PEGDMA as a co-crosslinker.

a)

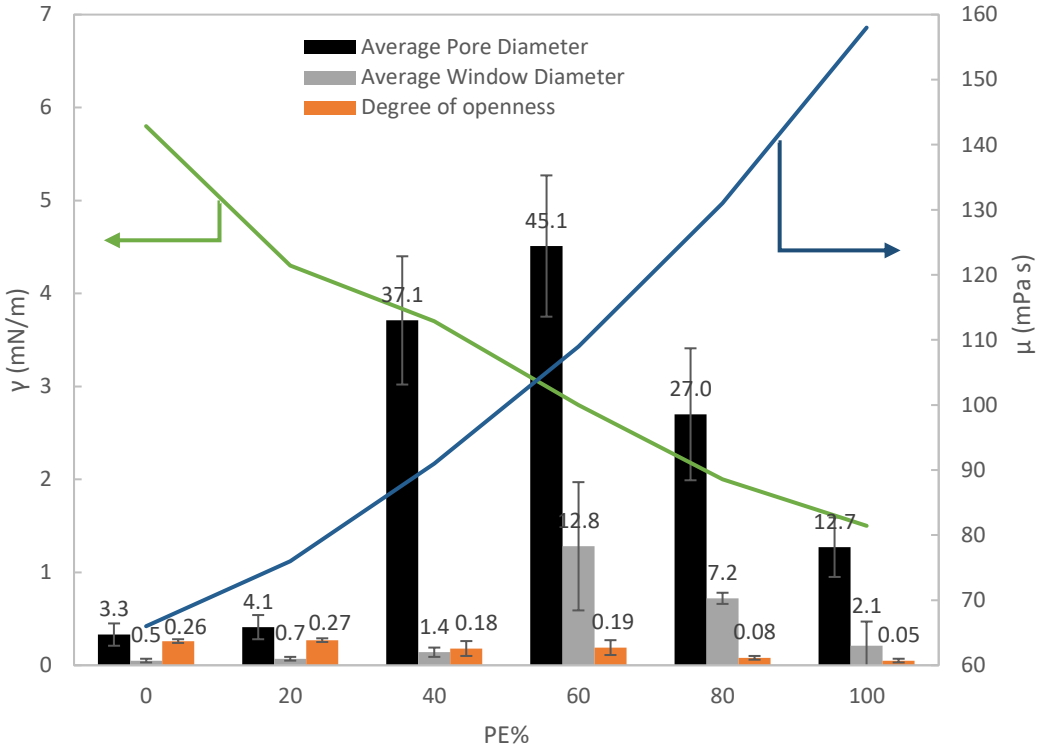
Average Pore Diameter
Average Window Diameter
Degree of openness
γ (mN/m)
μ (mPa s)
PE%
0
20
40
60
80
100
3.3
0.5
0.26
4.1
0.7
0.27
37.1
1.4
0.18
45.1
12.8
0.19
27.0
7.2
0.08
12.7
2.1
0.05

b)

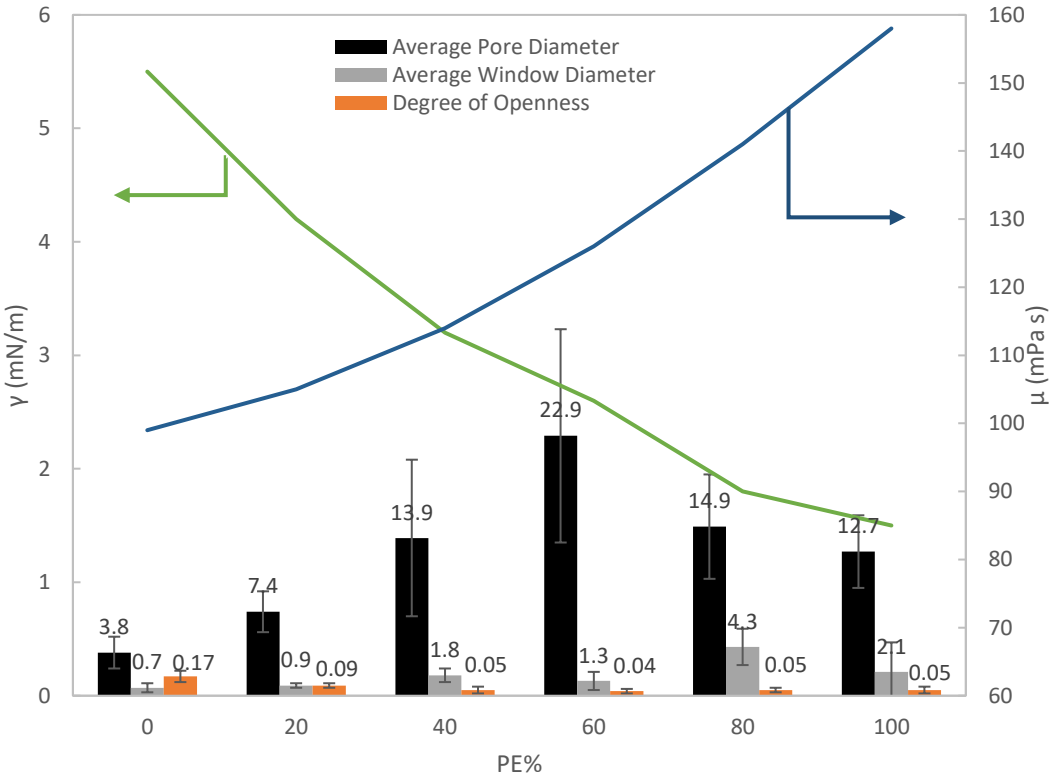

Figure 4-3. Effect of different concentration of PE in crosslinker mixture of a) G-E-PE and b) G-TE-PE on pore and window diameter, degree of openness, interfacial tension and oil phase viscosity.

On the other hand, to avoid droplet coalescence, in addition to using sufficient emulsifier, the emulsion must be stabilized through hydrodynamic effects such as increasing the collision time or increasing the viscosity of the continuous phase. It has been shown that the latter is an effective way to retard the liquid drainage between two colliding droplets, thus pushing the equilibrium towards

retention of individual droplets rather than coalescence [103]. Increasing the average molecular weight in the crosslinker mixture by addition of larger amounts of PEGDMA increased the viscosity of the oil phase in the prepared HIPE (Figure 4-3), resulting in competition between the effects of decreasing the interfacial tension and increasing the viscosity of the oil phase. This resulted in the observed peak in pore and window sizes at 60% PEGDMA.

The positive effect of increasing the continuous phase viscosity is also supported by comparing the range of pore diameters for G-E/PE (3.3–45.1 μm) and G-TE/PE (3.8–22.9 μm). The oil-phase interfacial tensions of G-TE/PE and G-E/PE were essentially equal at each level of added PEGDMA but the viscosities of G-TE/PE, with higher average molecular weights in the crosslinker mixtures, were higher than those of G-E/PE at all PEGDMA levels (Figure 4-3). Thus, the effect of higher viscosity in the oil phase was to drive the equilibrium towards lower coalescence and smaller droplet size. G-TE/PE also showed a narrower pore size range with increasing PE, despite the decrease in interfacial tension.

4.2.2 Mechanical Properties

The mechanical properties of the polyHIPEs investigated were evaluated using compression experiments at room temperature, with the resulting stress-strain curves summarized in Figure 4-4, while the crush

strengths and Young's moduli are reported in Figure 4-5. It is evident that the introduction of PEGDMA into the crosslinker mixture significantly increased the elasticity of the polyHIPEs. The long chain crosslinker also improved the crush strength considerably, with a one order of magnitude gain from EGDMA (or TEGDMA) to PEGDMA. In the presence of 40% PEGDMA in the EGDMA or TEGDMA crosslinker composition, the Young's modulus and crush strength increased 50% and 400%, respectively, with respect to their references samples (G-E and G-TE). With the introduction of 60% and 80% PEGDMA to TEGDMA, the Young's modulus decreased from 3.66 to 2.79 MPa, while no crush or collapse data were obtained because there was complete compression and the samples returned essentially to their initial length after removing the compressive force. However, the incorporation of PEGDMA into GMA/EGDMA led to a small increase in Young's modulus and crush strength. The Young's modulus of GE increased to 3.84 and 4.05 MPa with the introduction of 20% and 40% PEGDMA, respectively. By increasing the percentages of PEGDMA to 60% and 80%, the elasticity increased, and the Young's modulus decreased to 2.26 and 0.82 MPa, respectively. Meanwhile, there was no noticeable change in the crush strength for G-E(X%)/PE(1-X%), except for G-E(20)/PE(80), which showed completely elastic behavior. According to these results, polyHIPEs comprised solely of low molecular weight, short-chain crosslinkers did not produce robust materials. The addition

of PEGDMA with high molecular weight and long polymer chains increased chain mobility during mechanical deformation and the recovery processes to achieve further gains in compressive modulus. Thus, the combination of long- and short-chain crosslinkers is required to achieve the degree of polymer toughness to withstand compressive loads.

a)

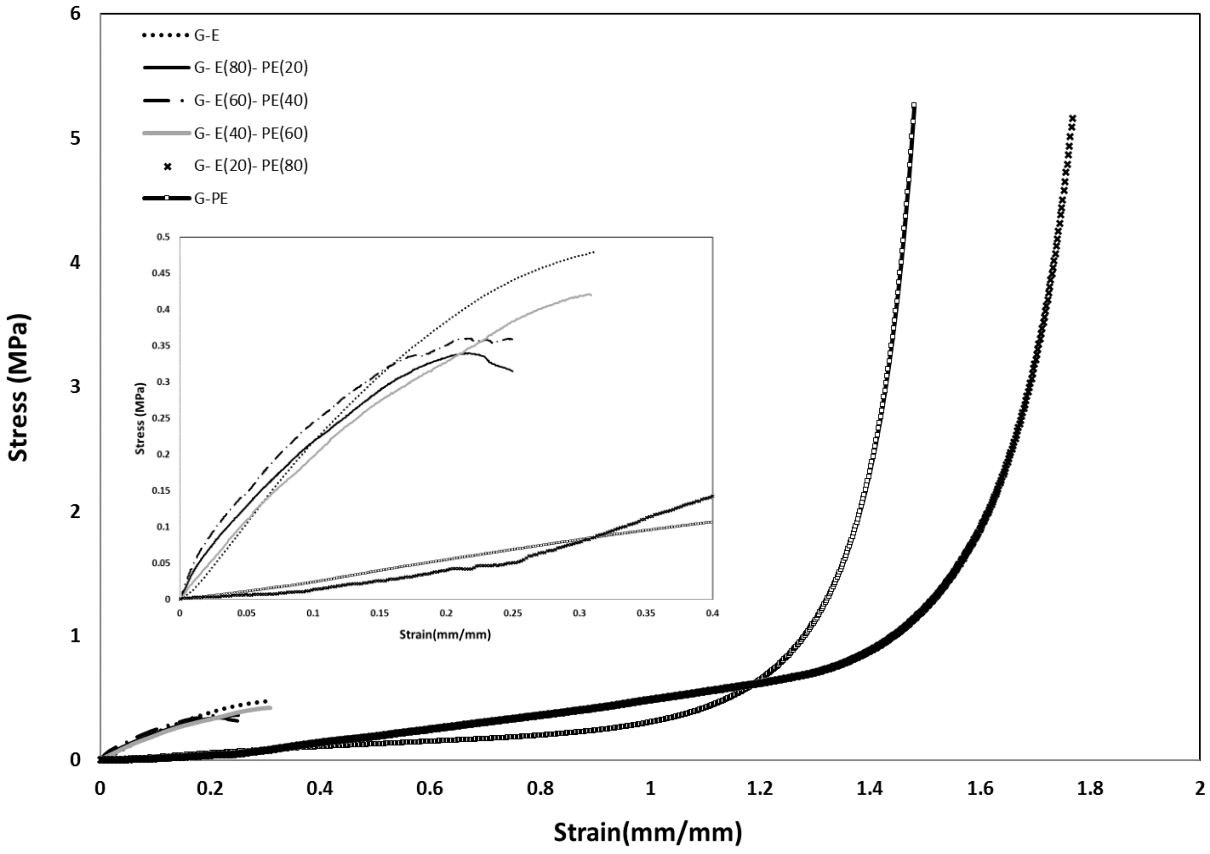

b)

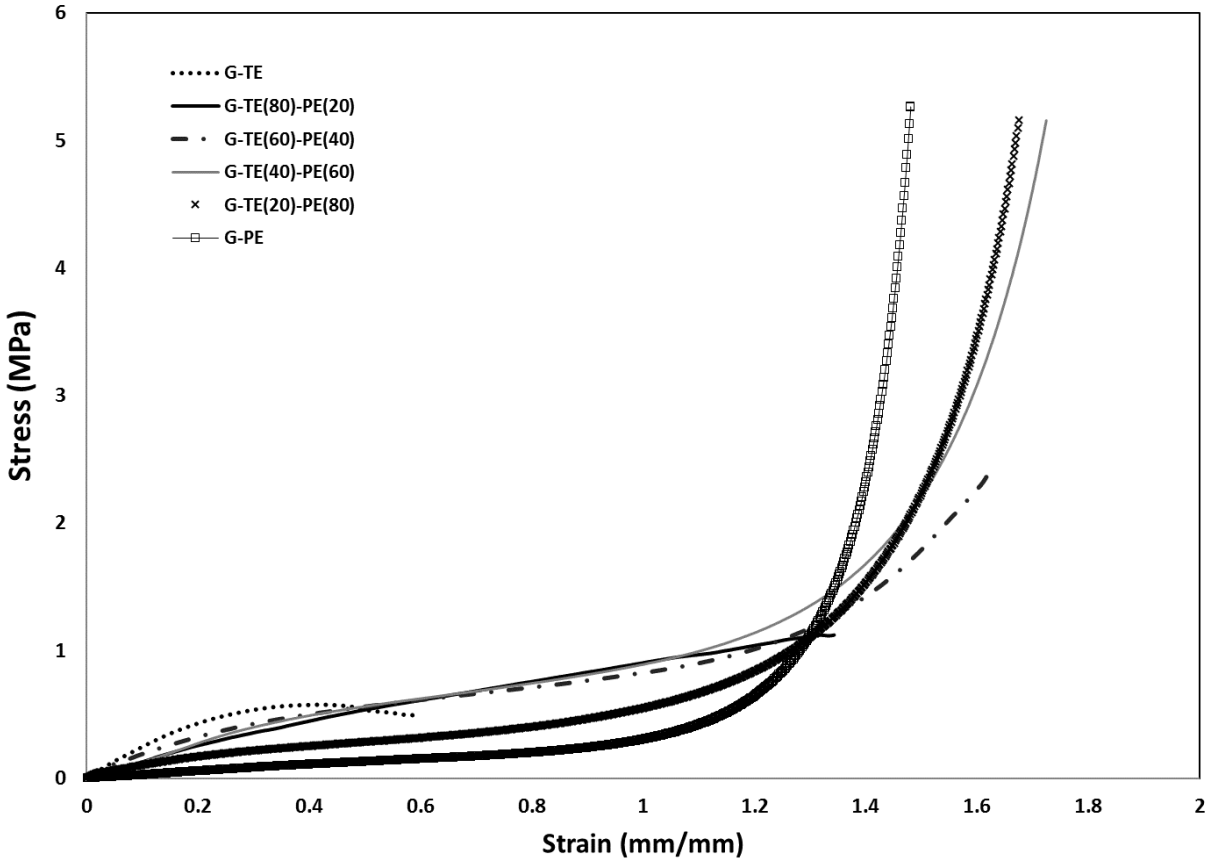

Figure 4-4. Stress-strain curves of the all polymer foam materials under compressive load. a) G-E-PE and b) G-TE-PE PolyHIPEs.

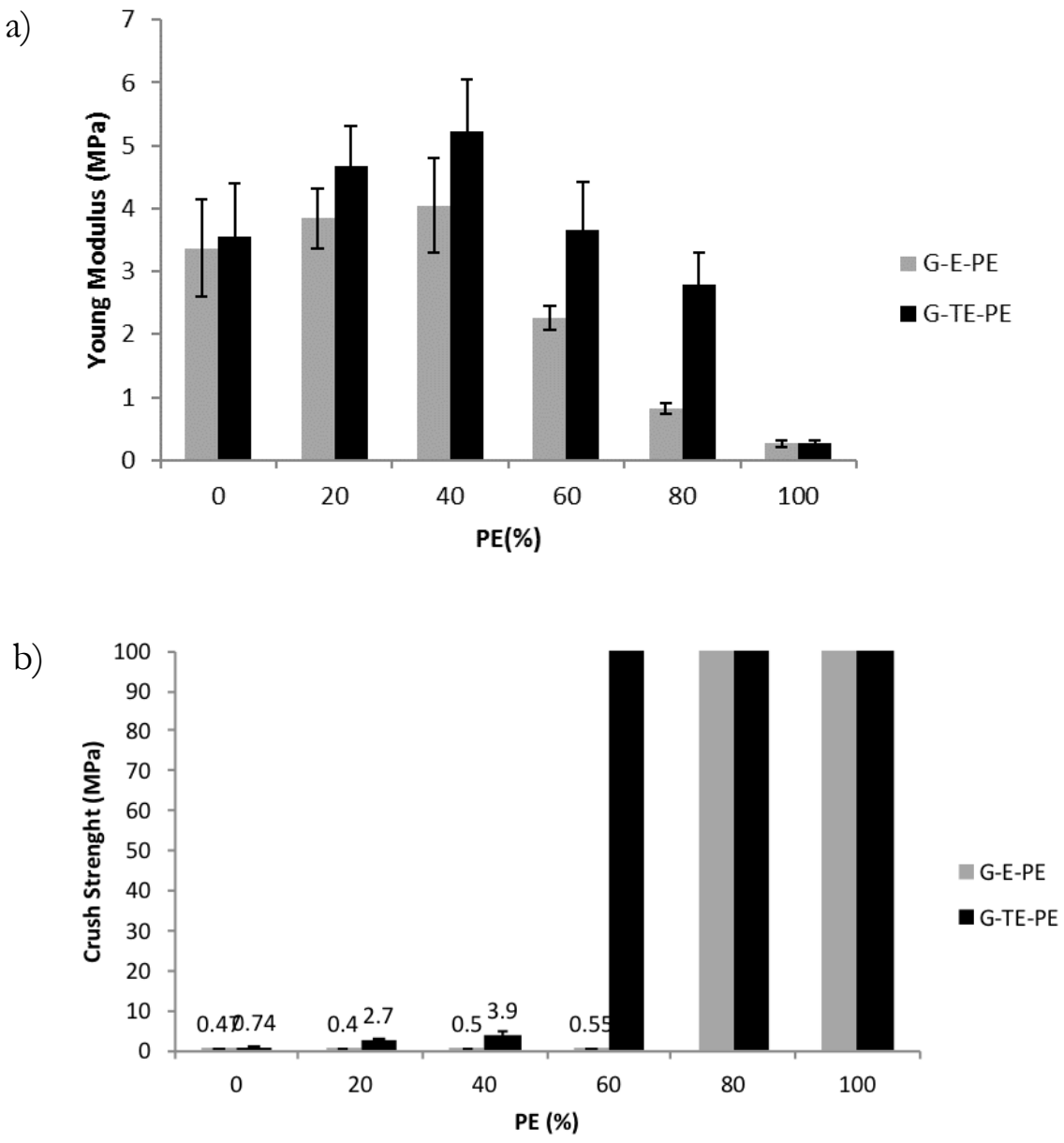

Figure 4-5. The influence of PE concentration in crosslinker mixtures on a) Young's modulus and b) crush strength of polyHIPEs.

As can be seen from Figure 4-5, G-TE/PE polyHIPEs had higher Young's modulus and crush strength than G-E/PE. The differences between these polyHIPEs were their average pore and window sizes as well as degree of openness and densities. From Figure 4-6, it can be seen that the densities of G-TE/PE polyHIPEs were higher than those of G-E/PE samples and that these approximately followed the standard "mixing rule" where the density of the samples equals the proportional contributions of the densities of the mixture components, i.e. density_G-E/PE = (v/v%G-E)×(density_G-E) + (v/v%PE)×(density_PE).

Gibson and Ashby reported that the Young's modulus of a polydisperse polymer foam is independent from pore size, and depends only on its squared relative density, defined as the density of the foam divided by the density of the matrix [103]. Relative density is equivalent to the volume fraction of solid, which in this case was constant for all prepared polyHIPEs. To determine whether the degree of interconnectivity or openness effects the mechanical properties of polyHIPEs, degree of openness values are compared in Table 4-1. It is clear that degree of openness values for G-E/PE were higher than those for G-TE/PE. It has been shown that the higher degree of openness is a result of thinner film layer between droplets at the same surfactant concentration and internal phase volume ratio 42. This is consistent with G-E/PE polyHIPEs having thinner pore walls than G-TE/PE, thus resulting in lower Young's

modulus and crush strength. Furthermore, G-TE/PE polyHIPEs showed a maximum in the Young's modulus and crush strength at 40% added PEGDTA, despite the fact that the foam density increased monotonically with PEGDMA addition. This result, as well as the low degree of openness, suggests that the microstructure may have an influence. With addition of PE to crosslinker mixture, pore size went through a peak, the same trend as for the corresponding Young's modulus. This could be because of thicker walls of larger pores than those in foams with smaller pores.

The compression stress-strain curve for a porous material consists of three different regimes: initial linear elastic, stress plateau and desinification [104]. Upon compression, the pore edge bend initially which corresponds to the initial linear elastic regime. Under continuing compression, the pore collapse progresses by elastic buckling, plastic yielding or brittle crushing, depends on the nature of the solid from which the material is made. Most attempts to improve brittleness of polyHIPE have been done in this regime, mostly using monomers that are naturally stiff materials. Also, their focus was increasing the Young's modulus in the initial linear elastic regime. Many of reports using this approach showed that Young's modulus was increased as much as 30 times compared with reference samples, while crush strength, which is the starting point of pore edge yield and when the opposite pore walls come into contact, was not improved even half as much as the Young's modulus [104].

In this chapter, it has been demonstrated that with addition of PE as the high molecular weight crosslinker, even at 20% in the crosslinker mixture, the brittle crushing behavior of polyHIPE was altered to exhibit a stress plateau and elastic bulking. The crush strength of G-TE(60)/PE(40) also increased over 400%, which is much more than the Young's modulus increment (around 50%). With further the addition of PE there was a crushing in polyHIPEs as they were transformed from completely brittle to completely elastic materials. These results along with the improved compression modulus and strength of G-TE(60)/PE(40), suggests that more attention should be given to this specific blend composition, as it appears to be a good candidate for supermacroporous stationary phases for use in chromatography.

4.3 Conclusion

The mechanical properties of GMA-based polyHIPE materials by using more flexible crosslinkers were improve. Thus, photo-polymerised polyHIPEs based on GMA and containing different crosslinking mixtures containing 0–100% by volume of EGDMA, TEGDMA and PEGDMA were prepared. Morphological investigations showed that the prepared foams possessed the characteristic interconnected pore structure and properties of typical polyHIPEs. Mechanical testing showed that addition of PEGDMA improves the mechanical

stability of polyHIPEs in terms of both compression strength and deformation at breakage and reduced brittleness and chalkiness of the resulting polyHIPEs, compared with those containing only EGDMA as a crosslinker. The Young's modulus and pore size of prepared polyHIPEs showed a maximum with increasing PEGMA composition in the crosslinker mixtures. This behavior suggests that GMA-TEGDMA(60)/PEGDMA(40) is a suitable candidate for use as a membrane or stationary phase in separation science.

Chapter 5 Printing of GMA-based polyHIPE

In this chapter, the design, fabrication and testing of a digital light processing (DLP) 3D printer, to build up a macroscopic complex geometry structure with high shape fidelity is described. A schematic of a DLP 3D printing process is shown in Figure 5-1. The DLP 3D printer was chosen for printing of the HIPE because of its high resolution (up to 10 μm) and its fast printing speed which is suitable for the unstable prepared HIPE. For printing the brittle control samples of GMA-EGDMA polyHIPEs, the printing platform was designed to move up-down so that the platform worked as a support for the cured HIPE. Systematic approaches such as controlling surface properties and light scattering were used to minimize spreading of the printed liquid. I relied on emulsion templating to achieve porous polyHIPE monoliths with hierarchical porosity.

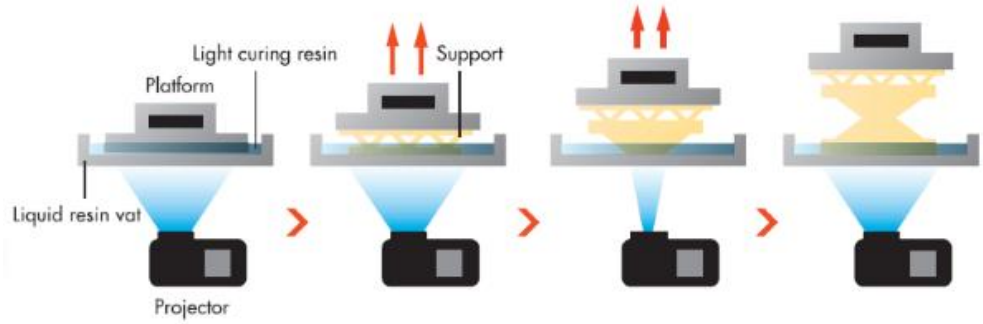

Figure 5-1. A schematic of a DLP 3D printing process.

5.1 Materials and Methods

5.1.1 Materials

All materials used in this chapter were listed in Section 2.1.1 except diphenyl (2,4,6-trimethylbenzoyl)phosphine oxide/2-hydroxy-2-methylpropiophenone, 50:50 blend and Orange 16 that were purchased from Sigma Aldrich and J.T. Baker, respectively, and used as received.

5.1.2 Methods

5.1.2.1 Fabrication of HIPE

HIPEs were prepared with different compositions according to the methods described in Section 2.1.3.

5.1.2.2 Development of DLP 3D printer

Optical Engine

To develop a DLP 3D printer compatible with printing polyHIPE, an optical engine was required. The chosen DLP was a high-resolution and high-brightness Production Ready Optical Engine, called the PRO6500 (Wintech Digital Systems Technology Corp., Carlsbad, CA). The PRO6500 (Figure 5-2) utilizes 0.65” 1080p digital micromirror device (DMD), incorporated into the optical path of a LED light, making maximum optical intensity and resolution. DMDs, consisting of 912 × 1140 Array of aluminum, micrometer-sized mirrors that move individually, offer a method of spatially modulating light that is fast, highly efficient and works over a broad range of wavelengths. Each pixel of the displayed image by DLP corresponds to an individual micromirror, which switches its orientation between ±12 degrees to the beam axis. Using this system, the x-y resolution of the DLP is given by the size of the pixel of the DMD.

Figure 5-2. An image of the PRO6500 optical engine.

The PRO6500 is available for different configurations (Table 5-1) according to the requirements of various application. I chose the PRO6500 with a 405 nm LED dominant wavelength because this wavelength has higher efficiency than 385 nm for curing the HIPE [105].

Table 5-1. Specification of PRO6500 with different configurations.

	PRO6500 LED Dominant Wavelength (nm)					
	385	**405**	**460**	**525**	**613**	**RGB**
Application(s)	3D Printing	3D Printing	3D Printing/3D Measurement	3D Measurement	3D Measurement	3D Measurement/ Display
Min. System Output	2,000mW	2,800mW	2,000mW	600lm	240lm	380lm
Available Projection Lens Working Distances *WD* (mm)	150	150	150 900	900	900	900
Field of View *FOV*(mm)	96x54	96x54	96x54 562x316	562x316	562x316	562x316
Projected Pixel Size (um)	50	50	50 293	293	293	293
Distortion (%)	<0.1	< 0.1	0.1-1	<0.6-1	<0.6-1	<0.6-1

The PRO6500 includes a USB-based application programming interface (API) and host graphical user interface (GUI). To generate machine tool paths and image slices, Creation Workshop toolkit (Envision Laboratories, Inc., Indianapolis, IN) was used. For controlling both the printer hardware and projector simultaneously, GCode programming was used. The user manual for Creation Workshop and GCode programming is downloadable from http://www.envisionlabs.net/.

Design of 3D Printer

According to the selected DLP optical engine, a CAD model of a DLP 3D printer was created using Solidworks by the 3D printing group's technician, Chemical and Process Engineering, University of Canterbury (design details of the DLP 3D printer are provided in Appendix A). First, all the parts required for the assembly were designed using dimensions taken from online information. The model contained different components including the optical engine, a frame, a vat (reservoir to hold the monomer mixture), a sample platform, a stage, and two stepper motors for controlling Z- and Y-axis movements. Because in some formulations, HIPE is a paste-like highly viscous material, a wiper was included in the design to move across the y-axis and spread the HIPE evenly on the surface for each layer prior to irradiation. Table 5-2 shows the list of components purchased for the design, with their specifications. Some of the designed parts, including the stage (stainless steel with 1 mm holes), the sample platform (stainless steel with a coating of epoxy resin on the screws), the wiper (stainless steel) and Z table (aluminum) were built in the Mechanical workshop in Chemical and Process Engineering, University of Canterbury. Other components, such as the belt holder, holder of the stepper motor and vat were printed using a FDM 3D printer (pp3dp, UP, China).

Table 5-2. Purchased components for DLP 3D printer.

Product	Model/Code	Company
2× Stepper motor	NEMA 17	MAKERshop (Auckland, NZ)
Timing Belt GT2 6mm Black Neoprene Rubber (per 100mm)	Belt-GT2-6mm	MAKERshop
Linear Stage	KK4001P-150A1-F3B	Linear Motion Ltd (Auckland, NZ)
Coupling (nema17 shaft is 5mm diameter)	SOH16	Linear Motion Ltd
Angle bracket for 30mm Extrusion - Die Cast Zinc		Autoline (Auckland, NZ)
SlotPro Roll in slot nut M5		Autoline
Sockethead screw 304	M5	Autoline
30 x 30 SlotPro 4 slot standard Profile (600 mm)		Autoline
30 x 30 SlotPro 4 slot standard Profile (250 mm)		Autoline
NSK Linear Guide Assembly LH100120ANK1B01PN1, LH	4979411	RS Components Limited (Auckland, NZ)
Extremely Fine Hex Adjuster M3 x 0.20, 15mm long	F3ES15	Thorlabs Inc (Newton, New Jersey)
Threaded Bushing, Phosphor Bronze, M3 x 0.20, 7mm long	F3ESN1P	Thorlabs Inc

The above components were mounted on a custom frame constructed from aluminum profile. The sample platform distance adjusted to be 15±0.1 mm from the PRO6500 lenses and 0 offset taken as the zero point for the z direction. Figure 5-3 shows the final built 3D printer. The sample platform movements in the z direction were controlled by a computer-activated NEMA 17 stepper motor. The y and z axis stepper motors were controlled using a USB to serial communication link to the control electronics. A similar communication link controlled the PRO6500, allowing the Creation Workshop software to switch the DLP on and control the exposure time, layer thickness and wiper movement.

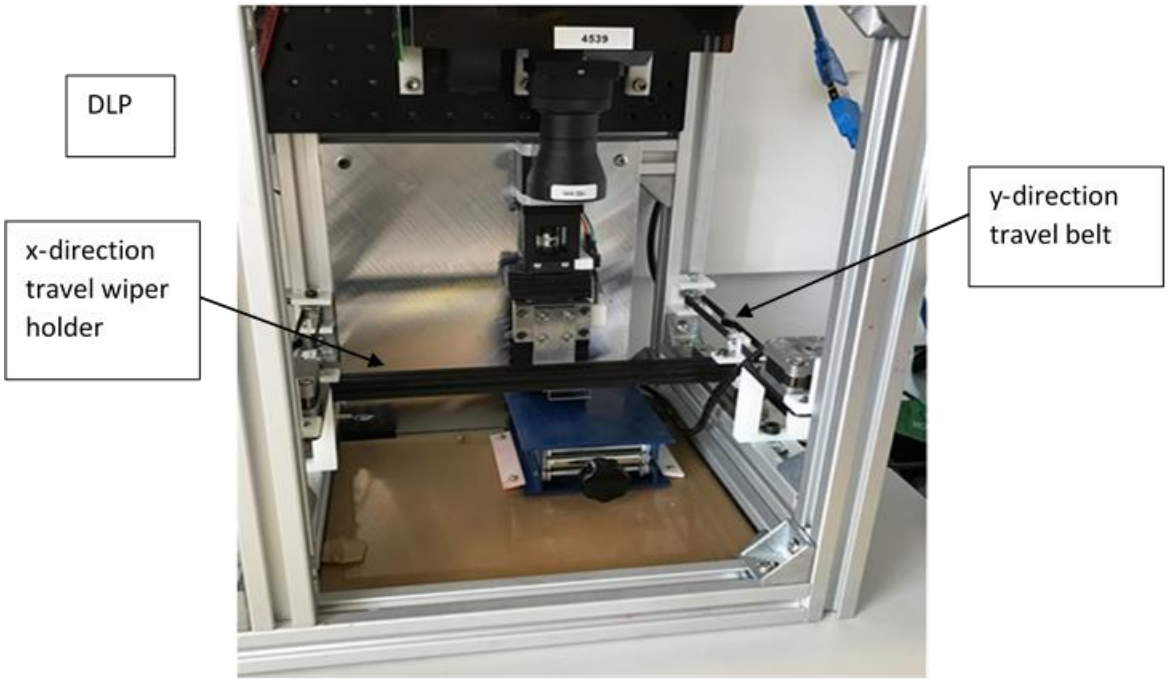

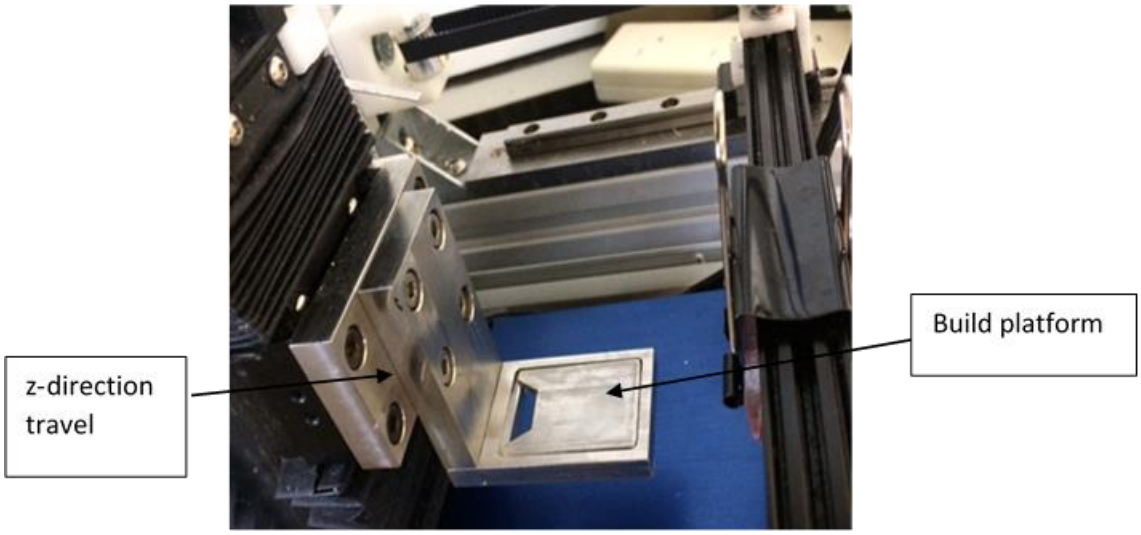

Figure 5-3. Image of fully assembled working DLP 3D printer.

5.1.2.3 Creation of gyroid column designs using Wolfram Mathematica and Solidworks

It has been shown that porous beds modeled on gyroid as one of triply periodic minimal surfaces (TPMS), offer better permeability, structural strength and geometric uniformity in comparison with packed beds [1, 106, 107]. To print a gyroid shape polyHIPE monolith, a unit cell of a network gyroid with 50% porosity was created in Wolfram Mathematica 11.2.0 (Wolfram, Champaign, IL). To create the network gyroid, which has one flow channel, the Mathematica code was created from equation (5-1) [106].

$$\sin(x).\cos(y) + \sin(y).\cos(z) + \sin(z).\cos(z) > G \qquad (5\text{-}1)$$

In the above equation, G defines the void fraction of the gyroid. For a void fraction of ε = 0.5, G = 0. Figure 5-4 shows the created network gyroid unit cell.

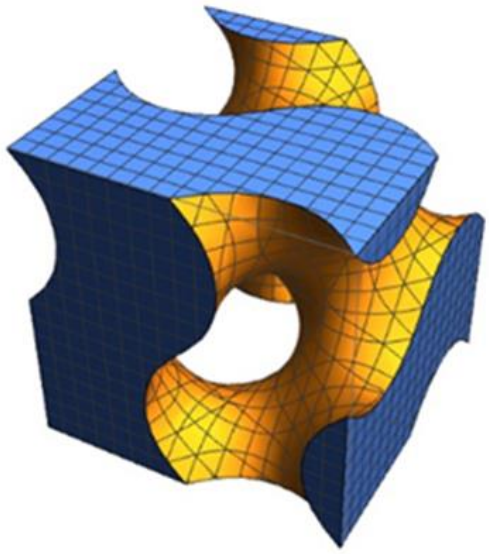

Figure 5-4. 3D plot of a network gyroid unit cell with G=0.

By choosing a void fraction of 0.5 for the unit cell, a monolith with 50% porosity was then made in SolidWorks. For this, an .stl file of the created unit was exported, then a circular layer of the gyroid structure was designed in the SolidWorks 2016 software package (Dassault Systèmes SOLIDWORKS Corp., Waltham, MA), as shown in Figure 5-5.

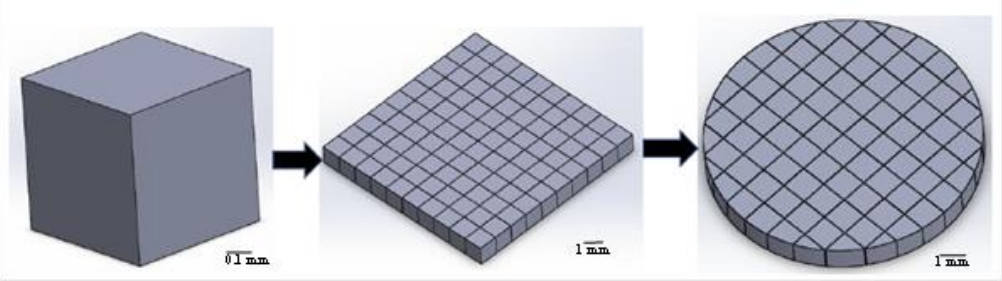

Figure 5-5. Designing a layer part [2].

To turn one gyroid layer into a full column, a linear component pattern in SolidWorks was used and the final gyroid monolith (Figure 5-6) was created and exported to an .stl file for importing to the CreationWorkshop software.

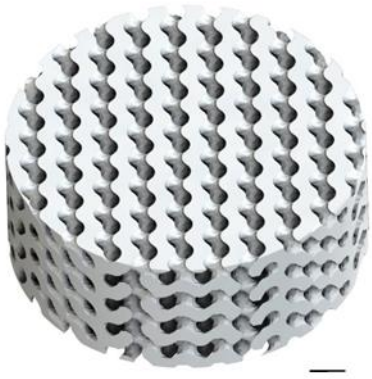

Figure 5-6. CAD Model of Network Gyroid. The unit bar equals to 1 mm.

5.1.2.4 Printing of PolyHIPEs using the DLP 3D Printer

The 3D solid model designed in Solidworks was sliced into horizontal layers of uniform thickness by Creation Workshop. Each layer was then spread in the printer and exposed for a set exposure time to the projected layer image

that using the DLP mounted at a distance of 15±0.1 cm from the substrate. After each layer was printed, the sample platform moved downward by a distance equal to the thickness of the single layer to allow a new layer of HIPE monomer to cover the surface of the object. The platform was then lifted to reach the zero point in the z direction. Next, the wiper moved forward and backward in the y direction to make an even covering of the new layer. The DLP then illuminated the layer for the set exposure time and cured the HIPE and the process was repeated to build up the entire polyHIPE gyroid monolith.

The printed polyHIPEs were washed on a glass filter with warm H_2O and extracted the unreacted monomers and other residual chemicals in a Soxhlet apparatus with methanol for 24 h, then dried in a freeze dryer (Labconco, Kansas City, MO) at -47°C and 0.070 mBar overnight.

5.1.3 Characterization

Contact angles of HIPE over different substrates for the build platform were measured by the sessile drop method using a CAM 200 instrument (KSV instruments Ltd, Helsinki, Finland). For measurements, a 5 µL droplet of HIPE was placed on the substrate. The contact angles were derived by fitting the

droplet shape by the Young–Laplace method using the built-in software CAM 2008 for data processing.

Microscopic images of resulting prints were taken using a Nikon microscope (Melville, NY) using ToupTek photonic instrument (Zhejiang, P.R.China) and the built-in software Top View (version: X86, 3.5.563) for measuring the feature sizes.

Morphological features of the polyHIPEs were investigated by SEM, using a high-resolution JEOL JSM 7000F field emission SEM. SEM images were analyzed using ImageJ software.

5.2 Results and Discussion

Resolution in a DLP-based 3D print is directly related to the interaction of the light beam with the photocurable resin. A number of light phenomena take place in the process, including light propagation and penetration whitin the resin medium, light absorbance due to the UV initiator and/or other UV sensible components in the resin formulation, and light scattering. The latter is particularly relevant in emulsions such as HIPEs, where the dispersed micron-sized water droplets deviate the light beam to different extents and different paths, thus reducing lateral resolution of the 3D prints (i.e. in the x, y and z directions). Layer resolution (i.e. in the z direction) is also a concern in the printing of complex objects such as those presenting overhangs or hollow or

empty features. In fact, the thickness of the printed layers need to be exactly defined to avoid curing resin beyond the nominal “slice”, thus causing deviations between the CAD model and the 3D printed artefact. A common solution to improve both lateral and layer resolution is to include a UV absorber in the formulation of the photocurable resin able to absorb excess UV light. The concentration of the absorber must be finely balanced to avoid excessive competition with the UV initiator, which would lead to inadequately photopolymerized materials. Other ways to improve the resolution and feature sizes are controlling the surface characterization, exposure time and layer thickness.

5.2.1 Controlling the light scattering

5.2.1.1 Addition of UV absorber

As it was mentioned in Section 2.4.3, one of the limitations for 3D printing of HIPEs by DLP 3D printer is the light scattering of the aqueous phase in the emulsion. For this reason, reactive Orange 16 dye was added to the aqueous phase of the HIPE as a UV absorber in this work. Reactive Orange 16 dye has two UV absorbance wavelength at the range of 385 - 410 nm and 491 - 497 nm so it is a proper UV absorber to use with both UV lamp in this work (Hönle UV-Handlamp and Pro6500 LED lamp) [108]. Resolution of printed samples was tested by printing a simple shape (Figure 5-7) using a number of

HIPE formulations containing different concentrations of Orange 16. The prints were performed at a constant layer thickness of 20 μm and 3 s exposure time for each layer to a total of ten layers. The designed model was two crossed lines surrounded by a circle, all with 1 mm nominal width. Figure 5-7 shows the improvements in resolution obtained by increasing the concentration of Orange 16. Printing with no UV absorber (Figure 5-7a) barely shows the designed shape. Presence of 0.5% of UV absorber (Figure 5-7b) helped to make the shape more clear but the width of designed lines and circle were increased 1.5 fold in print, and there were some residual polyHIPEs cured in the middle of the shape. A concentration of 0.15% light absorber (Figure 5-7d) prevented appropriate polymerization of the HIPE and the printed shape lost some parts of the shape. However, addition of 0.1% of the UV absorber gave the best print of the designed shape with a differential width error of 10% between designed and printed width. Therefore, a concentration of 0.1% Orange 16 was used in subsequent work as an appropriate balance between resolution and printability.

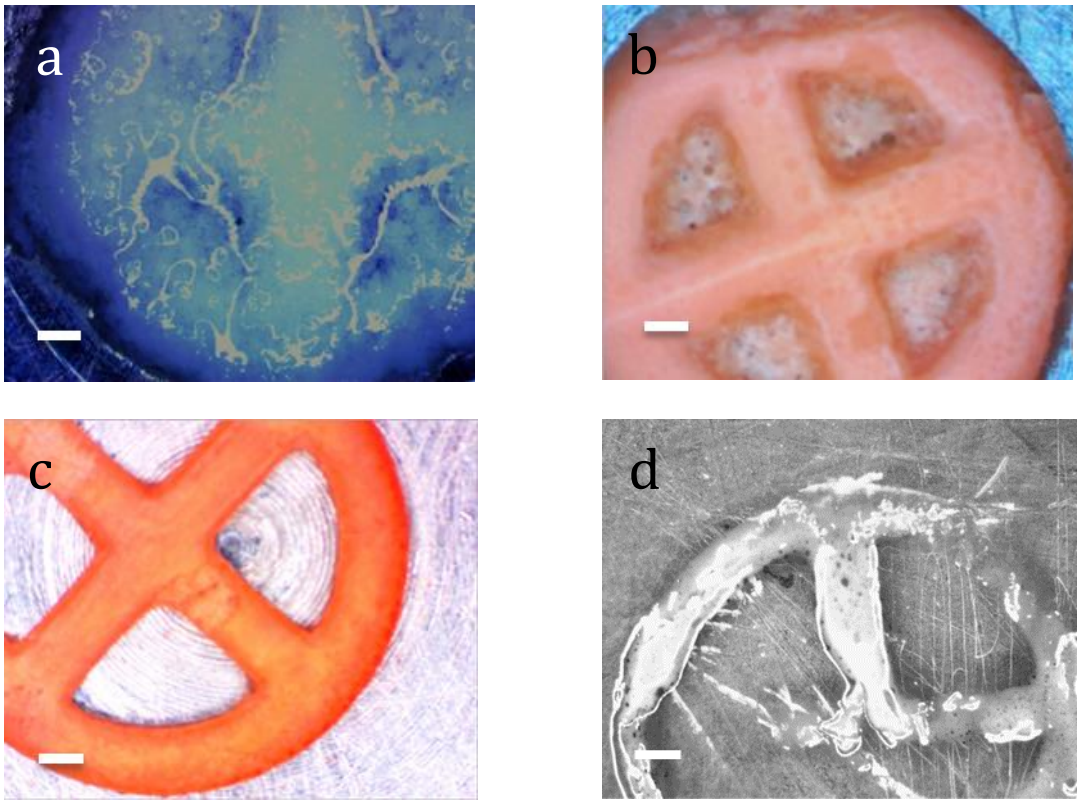

Figure 5-7. Effect of adding a) 0%, b) 0.05%, c) 0.1% and d) 0.15% of UV absorber. All scale bars represent 500 µm.

5.2.1.2 Effect of exposure time and layer thickness

To investigate the effect of exposure time and layer thickness on the control over feature sizes, the exposure time was increased from 2 to 5 s in increments of 1 s and the layer thickness changed from 10 to 40 µm by increments of 10 µm for printing lines with width of 1000, 500 and 300 µm and a total thickness of 2 mm. For all samples, a stainless steel substrate was used. Figure 5-8 shows images of a printed sample of the lines and Figure 5-9

compares the printed line widths with the designed dimensions for all the printed samples with different exposure time and layer thickness. The lines printed at 2s exposure time with differing width and layer thickness consist of discontinuous polyHIPE, suggesting 2 s exposure time is insufficient to completely cure and produce continuous polyHIPE lines. It is clear from Figure 9 that the largest difference between designed and printed lines is seen for printing with 10 and 20 µm layer thickness, regardless of exposure time. It appears that when the layer thickness is close to that of the HIPE internal-phase droplet diameter, HIPE is no longer able to act as an efficient template. It is also interesting to note that the feature size of the printed lines with 10 and 20 µm layer thickness and 300 µm width has increased more than the lines with 500 and 1000 µm width. However, comparing the increment in width during printing shows that the diffusion of scattered light is similar for each exposure time, almost independent of the width of the designed lines. For the lines printed with 30 and 40 µm layer thickness, it is obvious that the difference between designed and printed lines increases with increasing exposure time, indicating that with increasing exposure time, the amount of light scattering by the HIPE material increases, resulting in larger feature sizes. It is also noticeable that for all lines, regardless of width, the optimum printing condition is a 30 µm layer thickness and 4 s exposure. Printing lines with 30 and 40 µm layer thickness and 3 s exposure time also consisted of discontinuous lines, suggesting even 3 s

exposure time is insufficient to cure lines sliced into 30 and 40 µm layer thickness. In addition, with 5 s exposure time there was more time for scattering to occure and the time is more than required to cure HIPE. Accordingly, 4 s exposure time and 30 µm layer thickness is the optimum condition for printing features with controlled size consisting of continuous polyHIPE lines.

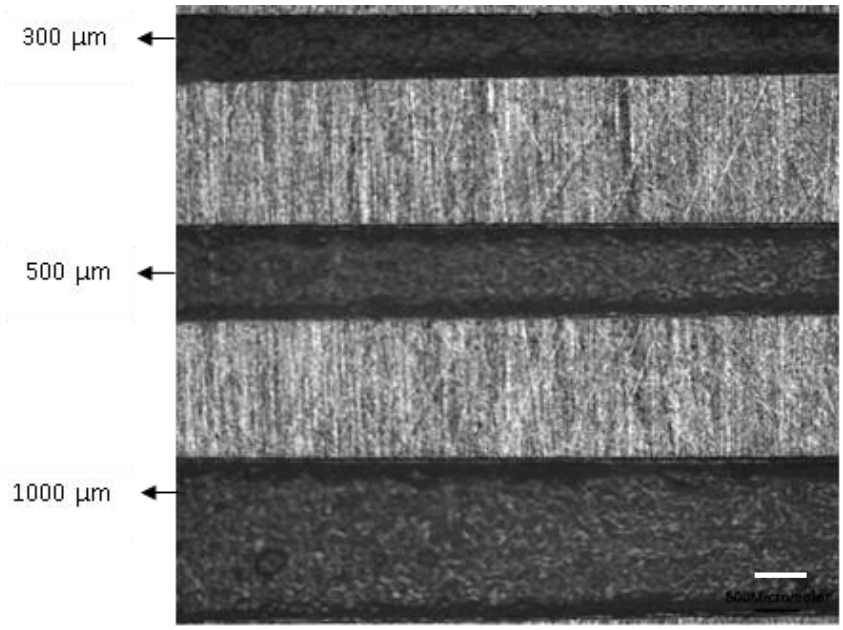

Figure 5-8. A sample of printed lines with different widths with 4 s exposure time and 30 µm layer thickness. Scale bar represents 500 µm.

a

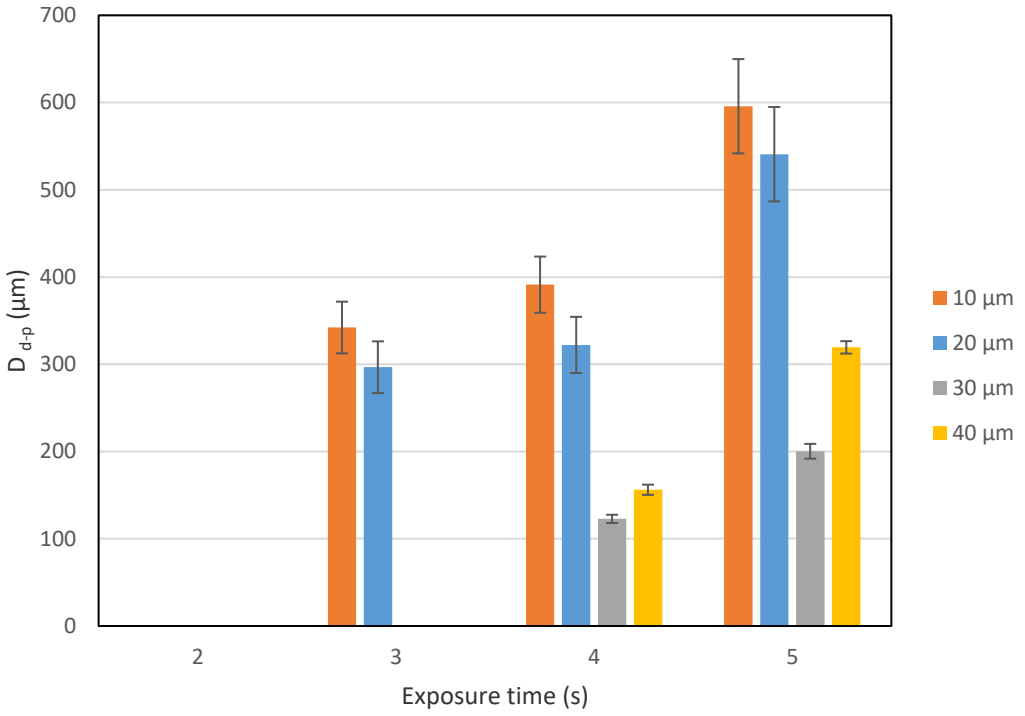
700
600
500
400
300
200
100
0
D d-p (µm)
2
3
4
5
Exposure time (s)
10 µm
20 µm
30 µm
40 µm

b

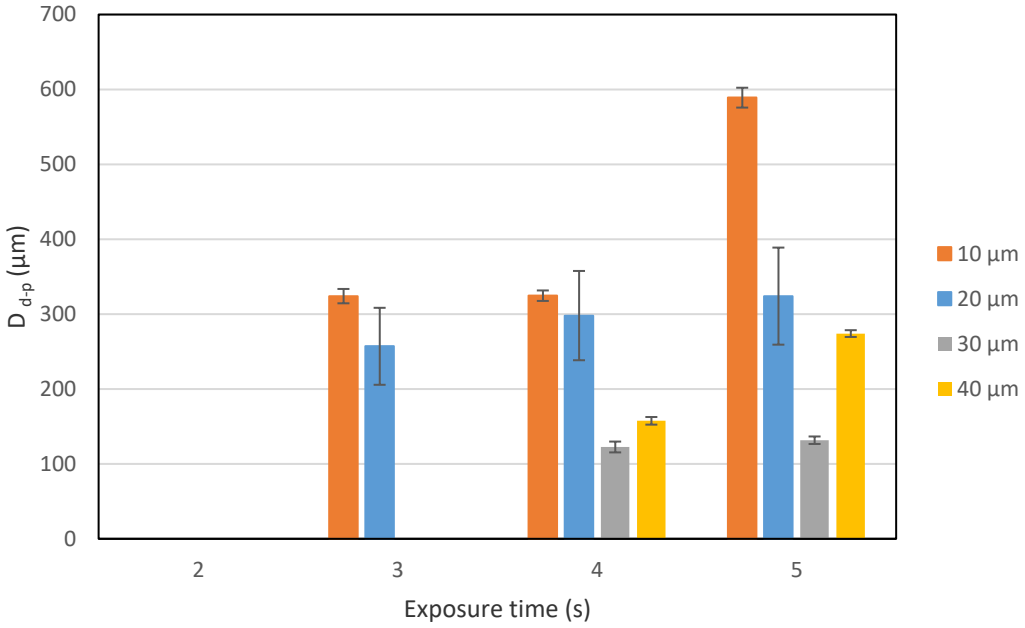
700
600
500
400
300
200
100
0
D d-p (µm)
2
3
4
5
Exposure time (s)
10 µm
20 µm
30 µm
40 µm

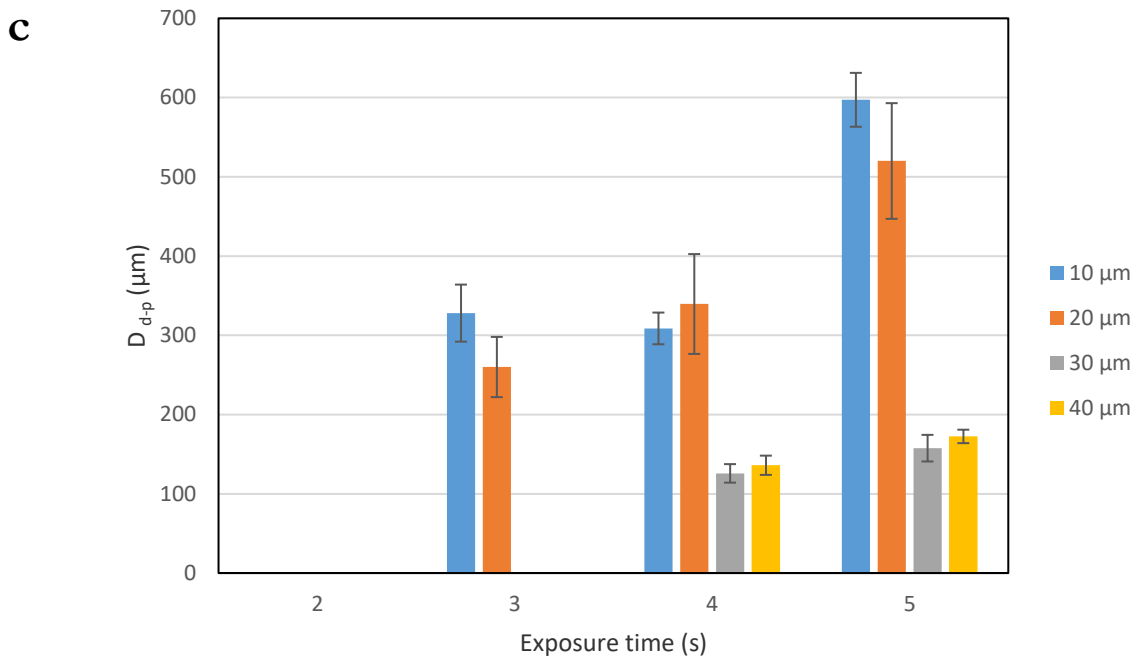

Figure 5-9. Differences between printed and designed line widths for three different widths a) 1000 µm b) 500 µm c) 300 µm. Colored bars represent layer thickness given in the legend.

5.2.2 HIPE printing substrate

The surface characterization of different substrates used for HIPE printing experimentally. Surface wettability of prepared HIPE on different substrates was measured using a static contact angles analysis. The contact angle determines the wettability of a HIPE droplet on the substrate surface and depends on the surface energy of the solid–liquid–air interface. It can be seen from Table 5-3 that all measured contact angles on different substrates were

smaller than 90°, even though around 80% of the prepared HIPE comprises water. HIPE contains a hydrophilic (water phase) component, which tends to advance the angle, and a dispersed hydrophobic component (oil phase), which tends to recede the angle. A low contact angle implies high wettability and high surface energy, whereas a large contact angle (>90◦) implies poor wettability and low surface energy [14, 15]. The results show that wetting of the surface of all the selected substrates is favorable for HIPE but there were differing degrees of spreading over the substrate surfaces. With complete wetting, when the contact angle is 0°, the liquid has a strong affinity for the solid and the droplet forms a flat puddle. HIPE had the lowest affinity to Teflon and highest affinity to a glass substrate. A high affinity would result in greater spreading of the HIPE on the glass substrate compared with other substrates and particularly Teflon. Consequently, greater spreading of the HIPE on the substrate would result in limited controlling the printing resolution because of penetration of light in the spread HIPE on the substrate.

Table 5-3. Contact angles for HIPE on various substrates.

Substrate	Stainless steel	Teflon	Acrylic	Glass
Contac Angle (◦)	32.2±1.3	45.3±1.2	21.2±1.7	10.6±0.9

To investigate the effect of surface wettability on printing, I carried out printing of designed lines of width 200, 300, 500 and 1000 µm. Figure 5-10 shows the difference of measured width of printed lines and the size of designed lines on four different substrates. It can be seen that the width of lines on the acrylic substrate increased 200 micrometer in the case of the 1000 µm designed line, 300 µm for the 500 µm designed line and more than two-fold compared with the designed width for 200 and 300 micrometer lines. Stainless steel showed the same trend as acrylic but with a smaller difference between print and design width. With the exception of Teflon, the spreading of printed lines at 300 and 200 µm was significantly larger than the spreading for wider lines. This trend could limit printing at 300 or 200 µm feature resolution and would result in decreasing resolution of printing on stainless steel and acrylic substrates. The lowest spreading of the printed HIPE was on Teflon substrates. All of these trends were entirely consistent with the results of contact angles and wettability. A low contact angle (high wettability), the printed lines spread on the surface to form relatively large features, while a lower wettability reduces the width of printed lines through higher contact angles.

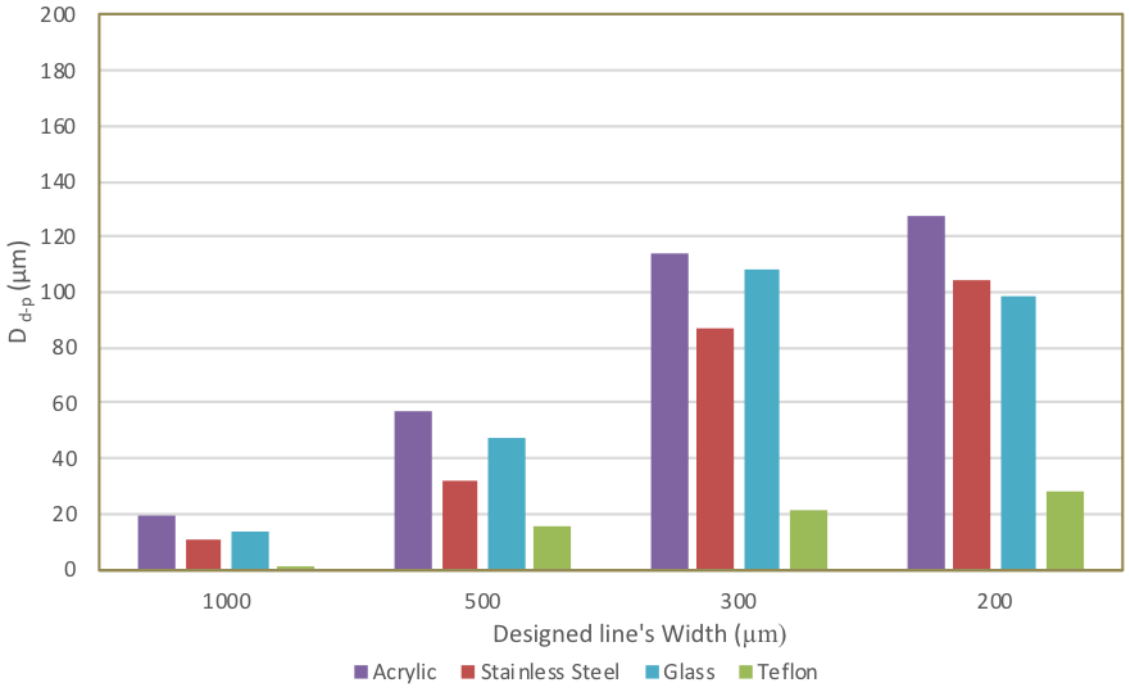

Figure 5-10. The width of printed continuous lines on different substrates.

5.2.3 Printing of HIPE gyroid monoliths

As explained in Section 5.1.2.3, to print HIPE gyroid monolith, a unit cell of a network gyroid with 50% porosity was created using Mathematica, and after importing the unit cell .stl file into Solidworks, a monolith 10 mm in diameter and 3 mm in height was created. Using Creation Workshop software (Gcodes in Appendix B), the monolith structure was printed with the optimized

UV exposure time and layer thickness, 4 s for each layer and layer thickness of 30 µm on the various substrates as discussed in Section 5.2.1.2.

Figure 5-11 shows images of the resultant prints on different substrates, Teflon, stainless steel and acrylic substrate. Glass did not produce adhesion to the polyHIPE, resulting in movement of the printed layers, destroying the print shape (Fig. 5-11 (d)). Measuring the dimensions of printed columns shows that the column printed on Teflon has the highest height amongst the samples (Table 5-4). A tentative explanation for this observation would be that the low wettability of the HIPE on the solid substrate would cause the printed lines to pull themselves together and create lines with high contact angle on the bottom layers. High cured lines act as a scatterer for the UV irradiation, which would make the consecutive layers thicker resulting in printing higher columns. This explanation is consistence for all three printed columns with the design height of 3 mm, however when the first printed layer is higher, then it makes higher

consecutive layers and finally higher printed column than the designed column, resulting in the prints column with the order twice the designed height.

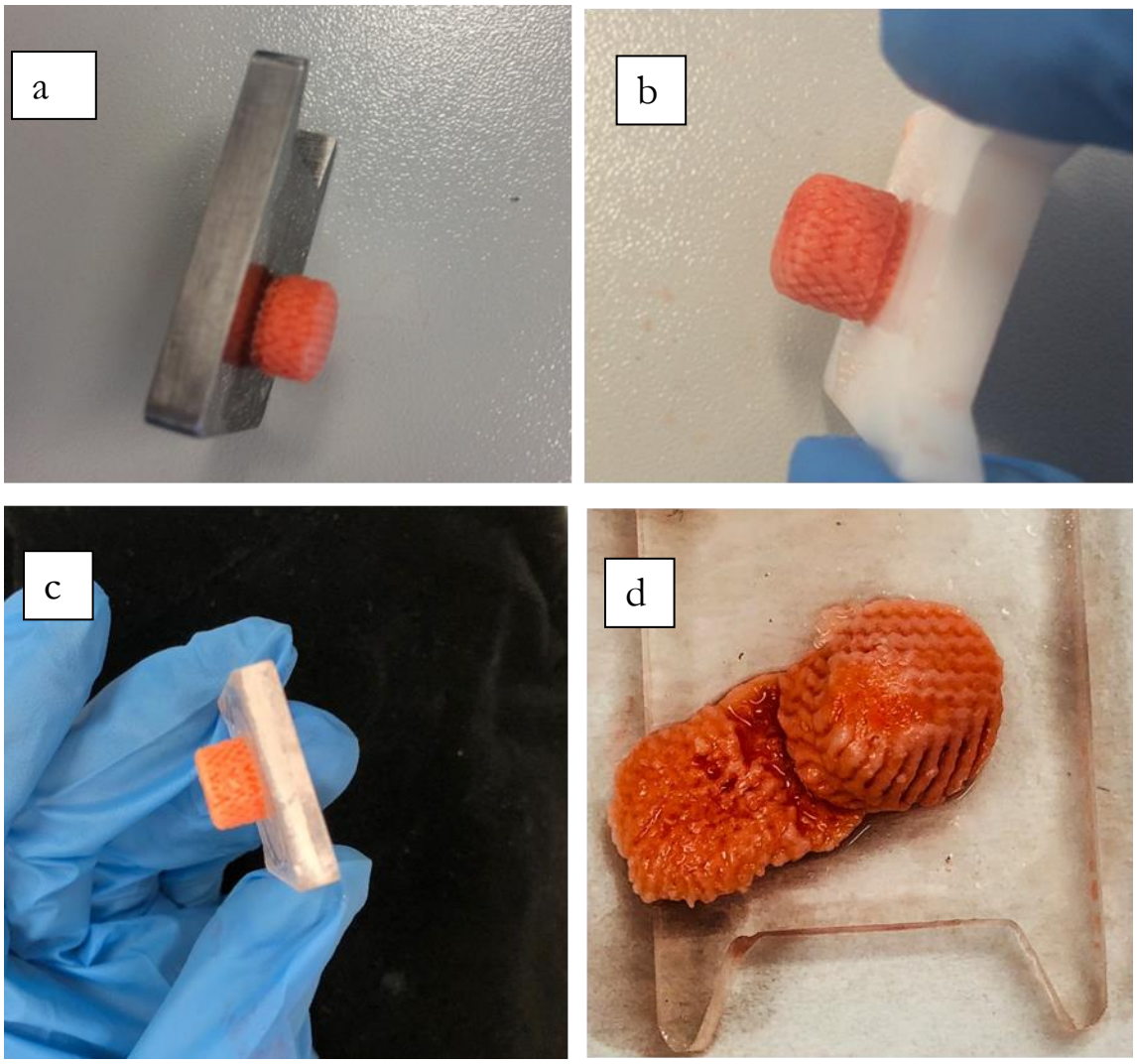

Figure 5-11. The images of the printed monoliths on a) stainless steel, b) Teflon, c) acrylic and d) glass.

Table 5-4. The measured height of printed columns on different substrates.

Substrate	Stainless steel	Teflon	Acrylic	Glass
Height (µm)	6545±166	7080±146	5718±64	---

To show the fidelity of the printed HIPE in the gyroid geometry, the width of the channel sizes in the monolith were determined using ImageJ 1.50 and are compared with the designed channel size (500 µm) in Table 5-5. It is clear that the column printed on Teflon substrate had the highest fidelity with the design dimensions, which can be attributed to the lowest wettability of HIPE.

Table 5-5. Comparing the width of the columns printed on different substrates.

Substrate	Stainless steel	Teflon	Acrylic	Glass
Width of channels (µm)	670±80	567±58	811±98	---

Figure 5-12 compares images of the bottom layer and top layer of all the printed columns. The top layers of all the samples had a relatively similar structure, but the bottom layers differed especially that printed on acrylic, which had the highest higher wettability and adhesion of HIPE on the substrate. Although in the DLP printer, the bottom layers are sacrificial and removed after the print, in this work they clearly influenced the structure of other layers. In

addition, the application of the printed columns is to act as a monolith for chromatography and the same structure is required in the bottom and top layers. Therefore, the Teflon substrate with highest fidelity and lowest difference between top and bottom layer was chosen for subsequent work (Fig. 5-13).

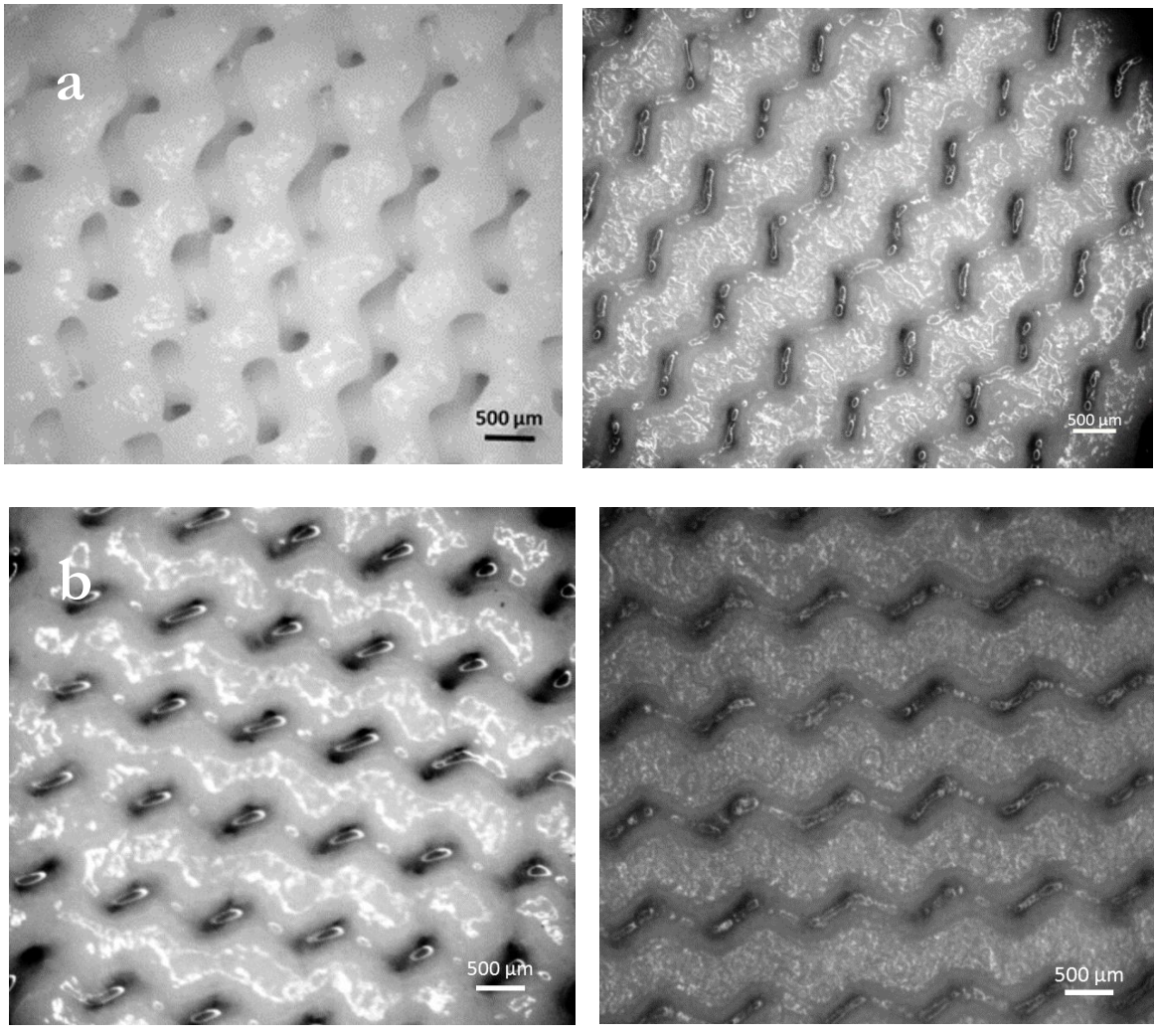

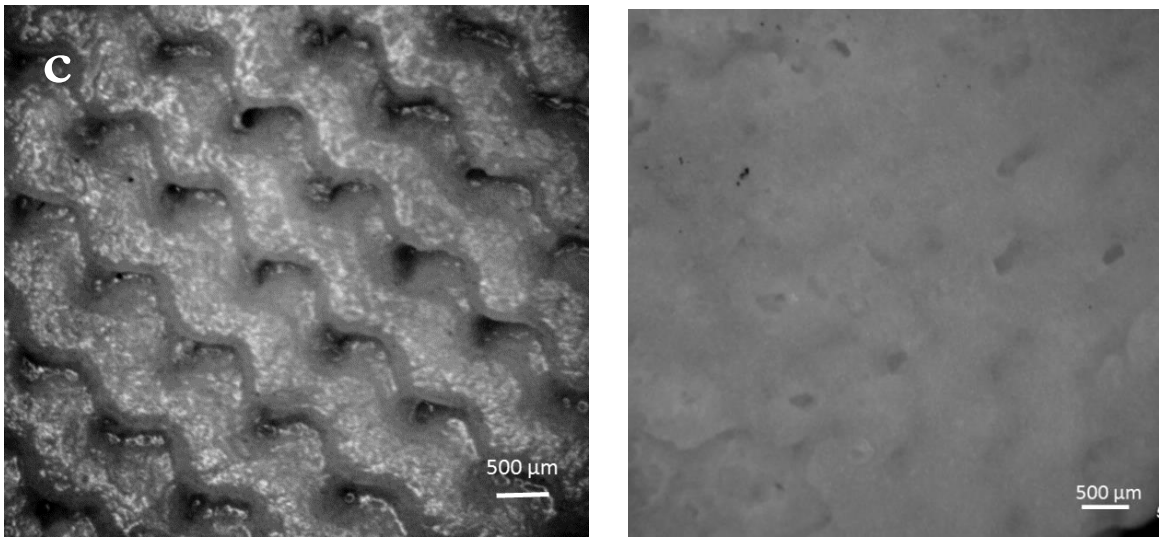

Figure 5-12. Images of top (left) and bottom (right) layer of columns printed on a) Teflon, b) stainless steel and c) acrylic.

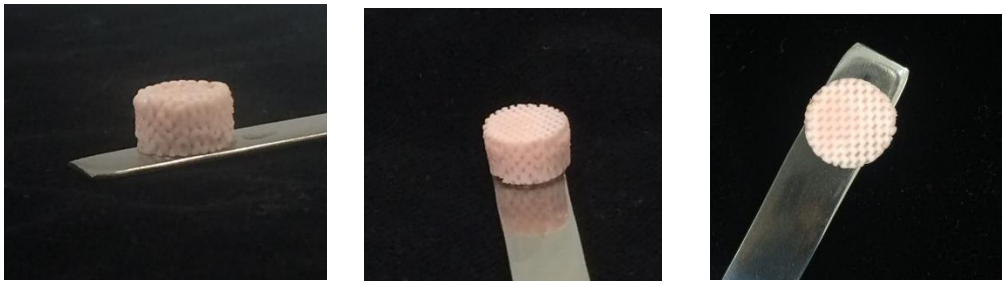

Figure 5-13. Print of a network gyroid monolith after washing and soxhlet extraction with methanol from different views. The scale bar equals 10 mm.

5.2.4 Morphology of a printed gyroid polyHIPE monolith

Scanning electron microscopy (SEM) was used to investigate the internal morphology of the printed structure. As mentioned in Section 3-3-2, measurements of pore size and pore size distribution in SG-E2-400(78) that was chosen as the basic formula in this work, was impossible because of its structure, so G-E1-400(78) was chosen to investigate the effect of the printing process on the average pore size and pore size distribution. Figure 5-14 compares SEM images of the cross-sectional areas of the printed monolith and the bulk photopolymerized HIPE and Figure 5-15 compares the average pore size distribution of both samples. The samples were all shown to have approximately the same average pore diameter and printing did not significantly affect this. However, the comparison of average pore size distributions show broadening and tailing towards a larger pore size for printed G-E1-400(78), which suggests coalescence of some droplets occurred in the reservoir during the printing process.

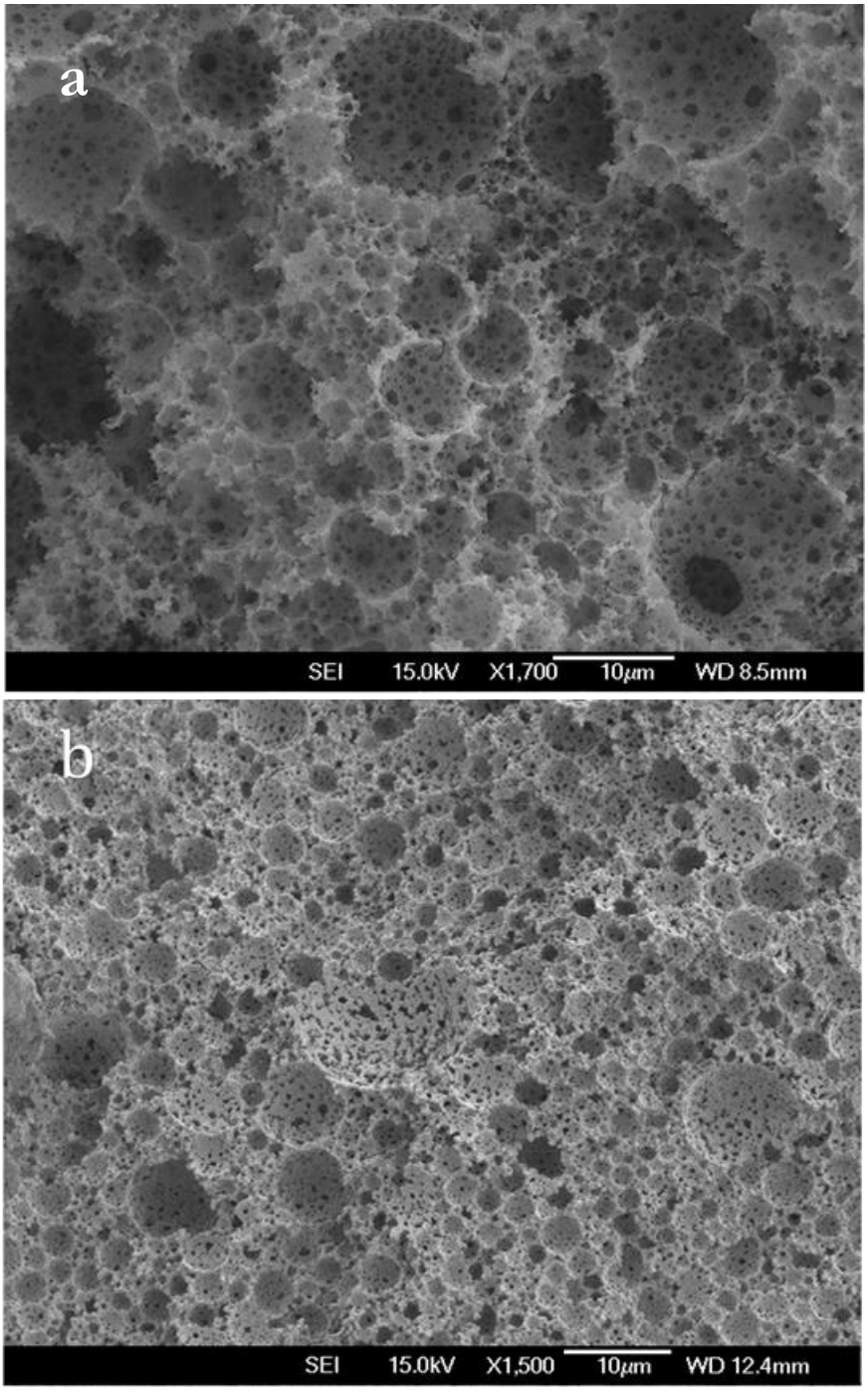

Figure 5-14. SEM images and pore size distribution of a) printed and b) bulk cured polyHIPE.

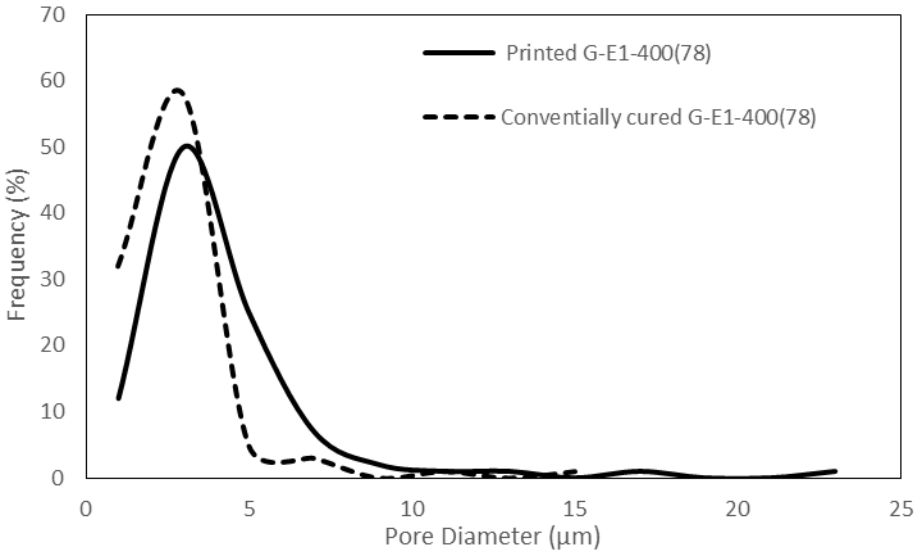

Figure 5-15. Pore size distribution of printed and bulk cured polyHIPE.

5.3 Conclusion

DLP 3D printing was successfully applied to the polymerization of high internal phase emulsions by controlling the UV scattering, light penetration and surface control methods. Using 0.1% reactive Orange 16 dye as a UV absorber was effective as a method of reducing scatter of UV light. Adjusting the UV light exposure time and layer thickness to 4 s and 30 µm, respectively led to controlling of printed feature size. The substrate with lowest wettability as measured by contact angel resulted in lowest spreading of the HIPE and led to the highest fidelity of a feature print. These controlling resulted in printing of porous materials with a complex geometry with consistent dimensions compared with the design dimensions. The material morphologies were found

to be consistent with those obtained from the bulk photopolymerisation of HIPE materials.

Chapter 6 Printed GMA-based polyHIPE as an anion exchanger

In this chapter, an anion exchange GMA-based polyHIPE, 3D printed monolithic column was developed by incorporating diethylaminoethyl (DEAE) functionality, a weak anion exchanger covalently attached to the backbone of the polymer. The static binding capacities of SG-E2-400(78) polyHIPE and mechanically improved GMA-TEGDMA(60)/PEGDMA(40) polyHIPE for Bovine Serum Albumin (BSA) were measured and compared. The chromatographic performances of the printed SG-E2-400(78) and GMA-TEGDMA(60)/PEGDMA(40) monolithic columns were evaluated, in terms of dynamic binding capacity, BSA recovery, dependence of backpressure on flow rate and separation of protein mixtures under gradient elution conditions.

6.1 Materials and Methods

6.1.1 Materials

All materials used in this chapter to prepare HIPEs are described in Sections 2.1.1 and 5.2.1. Diethylamine (DEA) was purchased from Sigma and used without chemical modification to functionalize printed GMA-based polyHIPE.

BSA was sourced from MP Biomedicals (Auckland, New Zealand). Cytochrome C and Myoglobin were purchased from Sigma and used without further purification.

Tris-HCl binding and elution buffers were prepared from Trizma (Sigma), HCl (Fisher Scientific, Loughborough, UK) and NaCl (Acros Organic, NJ). NaOH was purchased from VWR International Ltd. (Lutterworth, UK) and used for preparation of 1M NaOH for washing the columns. All buffer solutions were prepared using deionized (DI) water.

1-ethyl-3-(3-dimethylaminopropyl) carbodiimide hydrochloride (EDAC), N-hydroxysulfosuccinimide (Sulfo-NHS) and ethanolamine hydrochloride solution were purchased from Bio-Rad Laboratories (Hercules, CA, USA) and used for activation and deactivation of carboxylic groups on the backbone of the polyHIPE polymer.

6.1.2 Methods

6.1.2.1 Functionalization of polyHIPE with DEAE

Following methods described in the literature [109-111], printed monoliths or small pieces of GMA-based polyHIPE were functionalized with DEAE by immersion in 50 ml of DEA for 20 h at 40°C. Functionalized PolyHIPEs were extensively washed with ethanol and distilled water before usage.

6.1.2.2 Characterization of DEAE-functionalized polyHIPEs

Fourier-transform infrared spectroscopy (FTIR) was used to investigate the ring-opening of the epoxy groups that originated from the GMA monomer to introduce amine groups. The FTIR spectra measurements were carried out on a Bruker Alfa (Bruker, Billerica, MA, USA) in absorption mode.

6.1.2.3 Chromatographic characterisation of DEAE-polyHIPEs

6.1.2.3.1 Equipment

Axial-flow experiments were performed on an AKTAexplorer^{TM} 10XT (GE Healthcare Life Sciences) fast protein liquid chromatography (FPLC) system comprising a Pump P-903 unit with the flow rates up to 10 ml/min and pressures up to 25 MPa, a multi-wavelength UV-Vis monitor, and a combined monitor for on-line conductivity and pH monitoring. The system also included a fraction collector Frac-900 allowing up to 175 fractions to be collected. The whole

system was fully automated and controlled by Unicorn 5.31 software (GE Healthcare, Sweden).

6.1.2.3.2 Static Binding Capacity (SBC)

A known mass (dry basis) of polyHIPE pieces was equilibrated by immersion in binding buffer, 10 mM Tris-HCl pH 7.4 for 24 hours. Equilibrated polyHIPEs were then incubated with a series of initial protein (BSA) concentrations in Eppendorf tubes. BSA is a common model protein used in anion exchange chromatography studies, with a molecular weight of 66 kDa and an isoelectric point (IP) of 5.4. PolyHIPE pieces and the liquid were gently mixed by inversion for at least 12 h to achieve equilibrium binding. The Eppendorf tubes were then spun in a microcentrifuge (1730R, Gyrozen, Gyeonggi-do, Republic of Korea) at 17000 rpm for 5 min at 4°C and the protein concentrations in the supernatant assayed by spectrophotometer (as described below). Next, the supernatant (adsorption solution) was discarded and replaced with elution buffer. Elution was carried out by inversion mixing for another 12 h at room temperature and then eluted protein concentration was determined as described above. Triplicates were performed for each protein concentration. All experiments were run at room temperature.

To determine concentration, a calibration curve was first prepared by measuring the UV absorbance of a series of protein standards at 280 nm using a Thermo

Scientific™ NanoDrop spectrophotometer (Thermo Fisher Scientific Inc.). A linear relationship between the UV absorbance and the protein concentration was established for the buffer condition. Final protein concentration was thus determined from the calibration curve using UV absorbance at 280 nm. The binding capacity of each sample was determined by difference between initial and final solution protein content per mass of polyHIPE pieces (dry basis). The protein recovery was calculated as the percentage of total protein mass in the elution fraction relative to protein bound on the polyHIPE.

6.1.2.3.3 Dynamic binding capacity (DBC)

The printed polyHIPE monolith was fitted into a SNAPGlass Column 10 mm ID x 125 mm (Essential Life Solutions Ltd., Stoughton, MA) and the column was connected to the FPLC. The dead volume of the monolith was 3.38±0.21 mL, determined by measuring the change in conductivity of 0.1 M NaOH at a flow rate of 2 mL/min. The UV detector was set at 280 nm and the response time was set to 2.56 s. After washing all the lines with 20% ethanol solution and deionized water, each line was flushed with corresponding buffers at a flow rate of 10 mL/min to prepare the lines for determination of the absorbance of feed protein. The chromatographic steps included an equilibration step that prepared the column for binding by exposing it to 10 mM Tris-HCl buffer with pH 7.4 (5 mL), not shown in chromatograms. The binding step exposed the column to

protein solution (2 mg/mL BSA in 10 mM Tris-HCl buffer, pH 7.4) that was continuously fed through the column using an open loop for 10 mL protein solution. The washing step washed off protein that was weakly bound on the column surface using 5 mL of the same buffer as that used in the equilibration step. The elution step eluted the adsorbed protein using buffer at higher ionic strength, 10 mM Tris-HCl, 1 M NaCl, pH 7.4 (10 mL). The cleaning (washing) step removed all bond materials, including residual proteins using 1 M NaOH (20 mL). The column was then re-equilibrated in 10 mL of the start buffer before starting the next run. Figure 6-1 shows a chromatogram from a axial-flow experiment with a 6 ml/min flow rate.

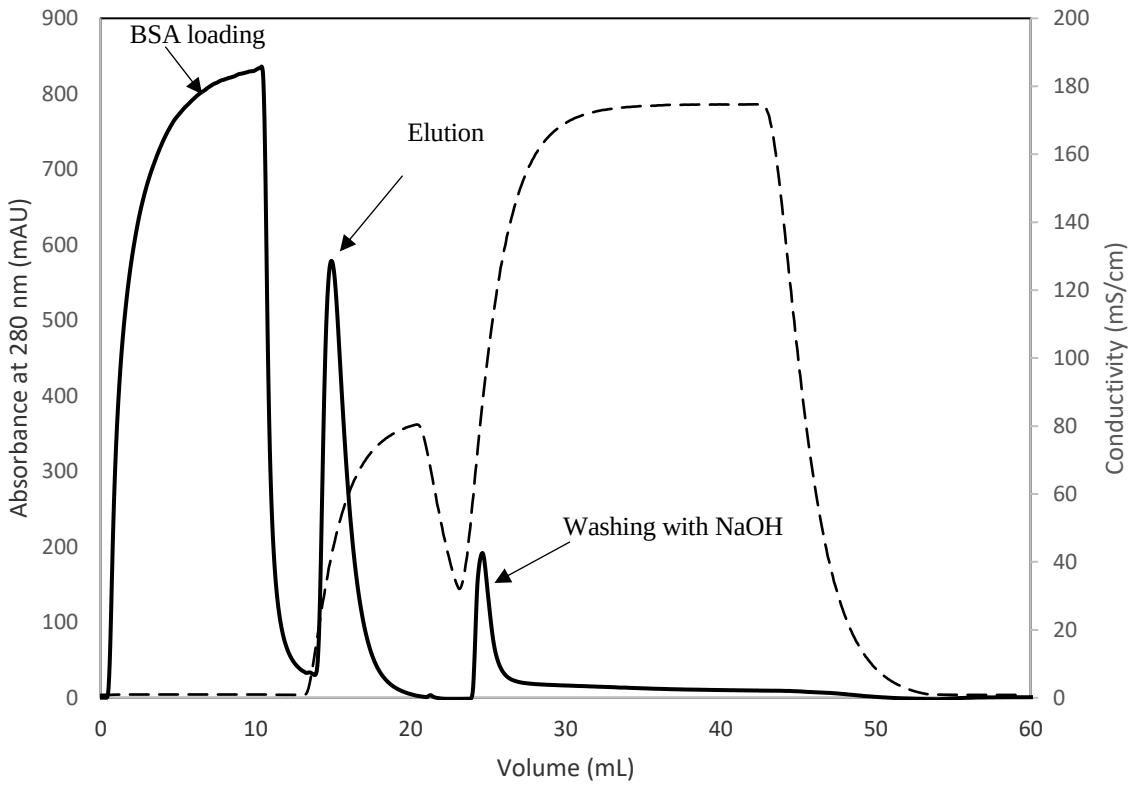

Figure 6-1. Chromatogram of 10 mL of 2 mg/mL BSA loaded on a printed SG-E2-400(78) polyHIPE column at 6 ml/min. The solid line represents the UV absorbance value and the dotted line represents the conductivity in the column.

The volume of protein solution needed to saturate the column was measured by a breakthrough curve, which could be recorded directly by monitoring the UV absorbance. Frontal analysis was first performed in the column by-pass position to obtain the elution profile of the protein solution under non-retained conditions (Figure 6-2). The area under this elution curve represents the mass of the protein flowing through the system, non-retained. The same experiment was then performed on the printed polyHIPE monolith to obtain the breakthrough curve.

In this case, the area under the curve represents the mass of the protein left after binding onto the monolith. The difference in the areas between the two breakthrough curves is the amount of adsorbed protein on the monolith, which can be calculated through the integration of the area under the two curves and taking their difference. Protein mass recovery was determined by a direct comparison of the protein peak areas obtained with and without the monolithic column.

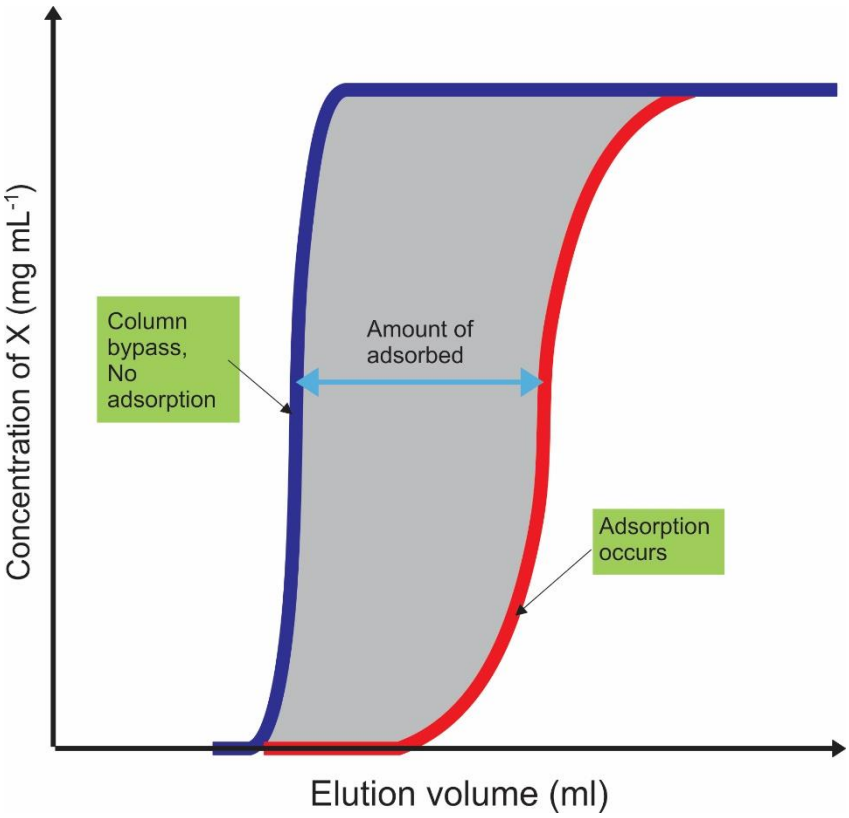

Figure 6-2. Adsorption capacity from frontal analysis. The area between the two curves is equal to the amount of protein adsorbed on the column.

6.1.2.3.4 Protein Separation

Protein separation on printed GMA-based polyHIPE monoliths was performed using a mixture of BSA /Myoglobin and BSA/Cytochrome C. The mixture of these proteins was prepared by dissolving them in binding buffer (10 mM Tris-HCl, pH 7.4) at a concentration of 3 mg of protein/mL. The protein absorbance at 280 nm was monitored during the test protocol. After 5 mL of column equilibrium with binding buffer, 100 µL of the protein solution was manually injected into the column. After washing the column with 10 mL binding buffer, a step gradient elution was then applied as follows: 15 mL, 20% elution buffer (B); 15 mL, 70% B. After elution step, the column was held at 100% B for 5 mL and then washed with 10 mL 1 M NaOH, followed by 5 mL of re-equilibrium with binding buffer. Fractions (2 mL) were collected in Falcon tubes during the adsorption and elution steps.

6.1.2.3.5 Gel electrophoresis

Sodium dodecyl sulfate polyacrylamide gel electrophoresis (SDS-PAGE) is a commonly used analytical technique to separate proteins according to their molecular weights. This analytical tool was used as a supplementary method to identify the collected proteins in the fractions.

The SDS-PAGE was run using a NuPAGE® Novex® 4-12% Bis-Tris Midi Gel from Invitrogen (Carlsbad, CA, USA) under reducing conditions. Protein samples were mixed with NuPAGE LDS 4X (Invitrogen, Waltham, MA, USA) sample buffer and NuPAGE Reducing Agents 10X (Invitrogen), and heated at 80ºC for 10 minutes. The gel was mounted into an XCell4 SureLock™ Midi-Cell (Invitrogen), filled with NuPAGE MES SDS (Invitrogen) running buffer and connected to PowerPac™ HC (BioRad Labrotories) power supply. 10 µL of Novex Sharp Pre-stained (Invitrogen) protein standard was used as a protein marker and 10 µL of sample was loaded in each well. The gel was run for 40 minutes at a constant voltage of 200 V. Proteins were stained with Coomassie Brilliant Blue R 250 (Sigma), 0.125% (w/v) in 10% acetic acid and 40% methanol. Destaining was carried out in a solution of 10% acetic acid and 20% methanol in water. The gels were scanned using a Stratagene Cheme Genius 2 (Syngene, Cambridge, UK).

6.1.2.3.6 Capping of carboxylic groups on the GMA polyHIPE backbone

The most common approach for capping of carboxylic groups is to use an aqueous mixture of N-hydroxysulfosuccinimide (sulfo-NHS) and 1-ethyl-3-(3-dimethylaminopropyl) carbodiimide hydrochloride (EDAC) to firs activate carboxyl groups to yield amine reactive esters and then to cap the NHS esters with a methyl group using ethanolamine. In this regard, 7.5 ml of deionized

water was added to EDAC (0.575 g) powder to dissolve it. This made a 10× 400 mM EDAC stock solution. To prepare a 10× 100 mM S-NHS stock solution, 7.5 ml deionized water was added to the sulfo-NHS (0.163 g) powder. The activation solution (20 mM EDAC/5 mM sulfo-NHS) was injected for 1 to 5 minutes through the monolithic column. Finally, 150 µl of ethanolamine hydrochloride solution is injected to covalently cap the residual NHS esters and thus neutralize the carboxyl groups.

6.2 Results and Discussion

6.2.1 Functionalization of polyHIPE with DEAE

The modification of GMA-based polyHIPE with DEAE was described in Section 6.2.2.1 (Figure 6-3). The FTIR spectra of the GMA-based polyHIPE is given in Figure 6-4. The absorption bands at 908 and 844 cm^{-1} were assigned to the deformation bands of the epoxy ring. The broad band at 1730 cm^{-1} is characteristic of the carbonyl group (C=O) in the acrylate group. The epoxy ring-opening reaction through the nucleophilic addition of amine leads to the disappearance of the deformation band of the epoxide ring and concomitantly to an increase in the characteristic bands at 2800 cm^{-1} for the DEAE.

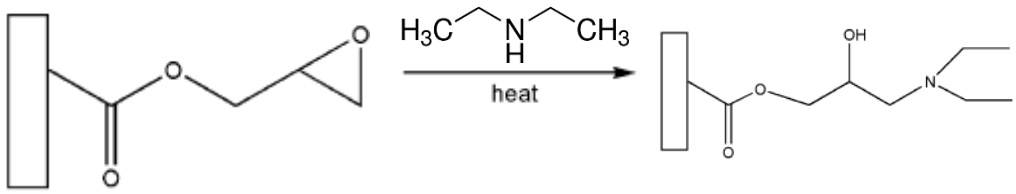

Figure 6-3. Schematic of functionalization of GMA-based polyHIPE with DEAE.

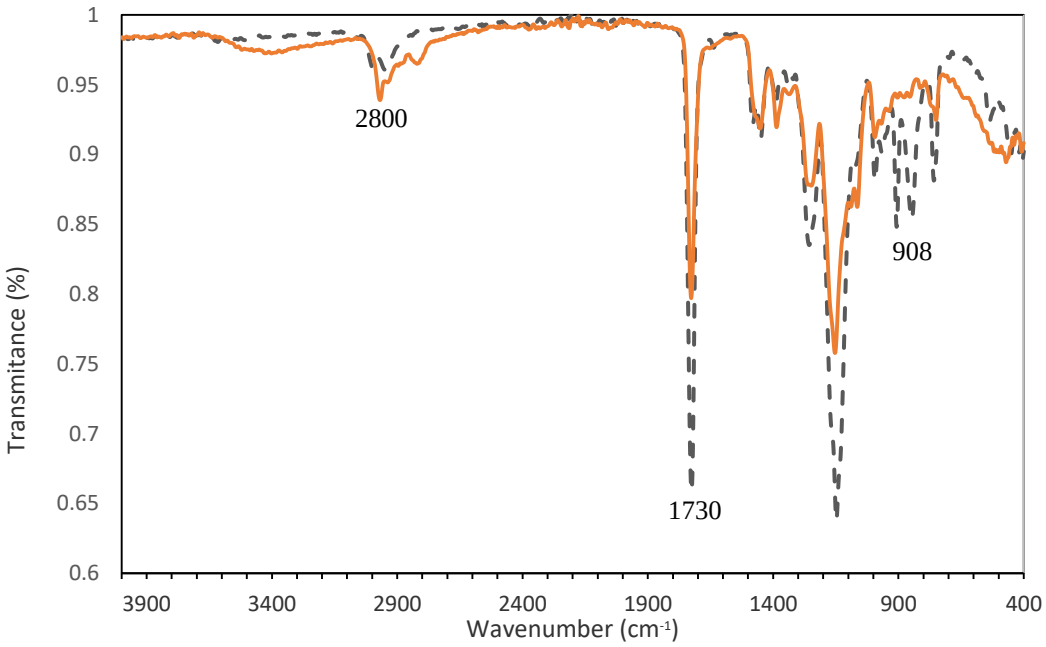

Figure 6-4. The FTIR spectra of the SG-E2-400(78) (dashed line) and functionalized SG-E2-400(78) (solid line) monoliths.

As is clear from the FTIR spectra of the SG-E2-400(78) polyHIPE, epoxy groups remained intact during the polymerisation of GMA-EGMD, but during post-modification they reacted with DEA and resulted in a DEAE-

functionalized SG-E2-400(78) monolith, generating a weak anion-exchange media.

6.2.2 Chromatographic performance of SG-E2-400(78)

6.2.2.1 Protein binding capacity of SG-E2-400(78)

Adsorption isotherms reflect the amount of protein bound to the surface of the resin (q) (mg g^{-1}) as a function of the concentration (C, mg mL^{-1}) under equilibrium conditions at a constant temperature [32]. Therefore, static (equilibrium) binding capacity is the most common method used to obtain the adsorption isotherms. Figure 6-5 shows a comparison between adsorption isotherms of functionalized SG-E2-400(78) and G-E2-400(78). Both polyHIPEs produced isotherms that were similar in shape to the type I adsorption isotherm, which can be described by the Langmuir equation. As can be seen, the equilibrium adsorption capacity for G-E2-400(78) was improved dramatically by sonicating of HIPE before polymerization. By sonicating, the equilibrium binding capacity increased from about 100 mg BSA g^{-1} polyHIPE to 160 mg BSA g^{-1} polyHIPE. The binding capacity depends on many factors including the availability of ion-exchange ligands for interaction with the biomolecules in the mobile phase. This result suggests that a higher specific surface area of SG-E2-400(78) produced using sonication gives a greater

contact area between the polyHIPE and the solution and better utilisation of the solid part of the bulk monolith volume.

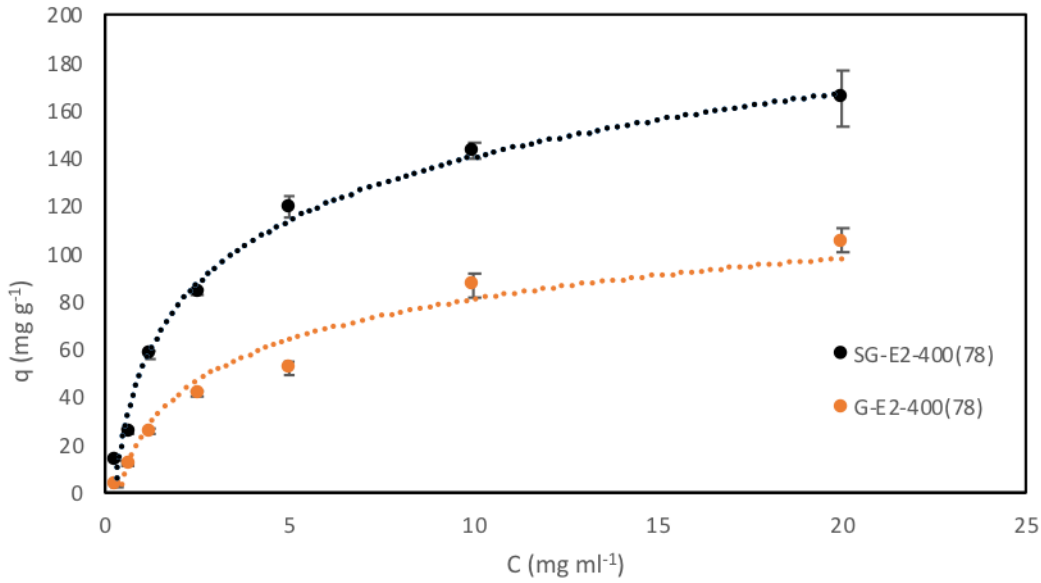

Figure 6-5.Static binding capacities of functionalized SG-E2-400(78) and G-E2-400(78) for BSA. All measurements were at pH 7.4 and room temperature (20ºC). Error bars are ± one standard deviation from triplicate measurements.

6.2.2.2 Elution experiments

1 M NaCl was used to desorb bound BSA from the SG-E2-400(78). Figure 6-6 shows the binding capacity of BSA on the anion exchange polyHIPE and the percentage of the bound BSA recovered during 1 M NaCl elution. The recovery results show that all the recovery values are over 80% and they increase to over 90% with increasing protein concentration. This indicates that an elution buffer

(buffer B) comprising 1 M NaCl was an effective eluent buffer for SG-E2-400(78) resin. Therefore, 1 M NaCl was adopted as the eluent in subsequent experiments to ensure high recovery of bound protein.

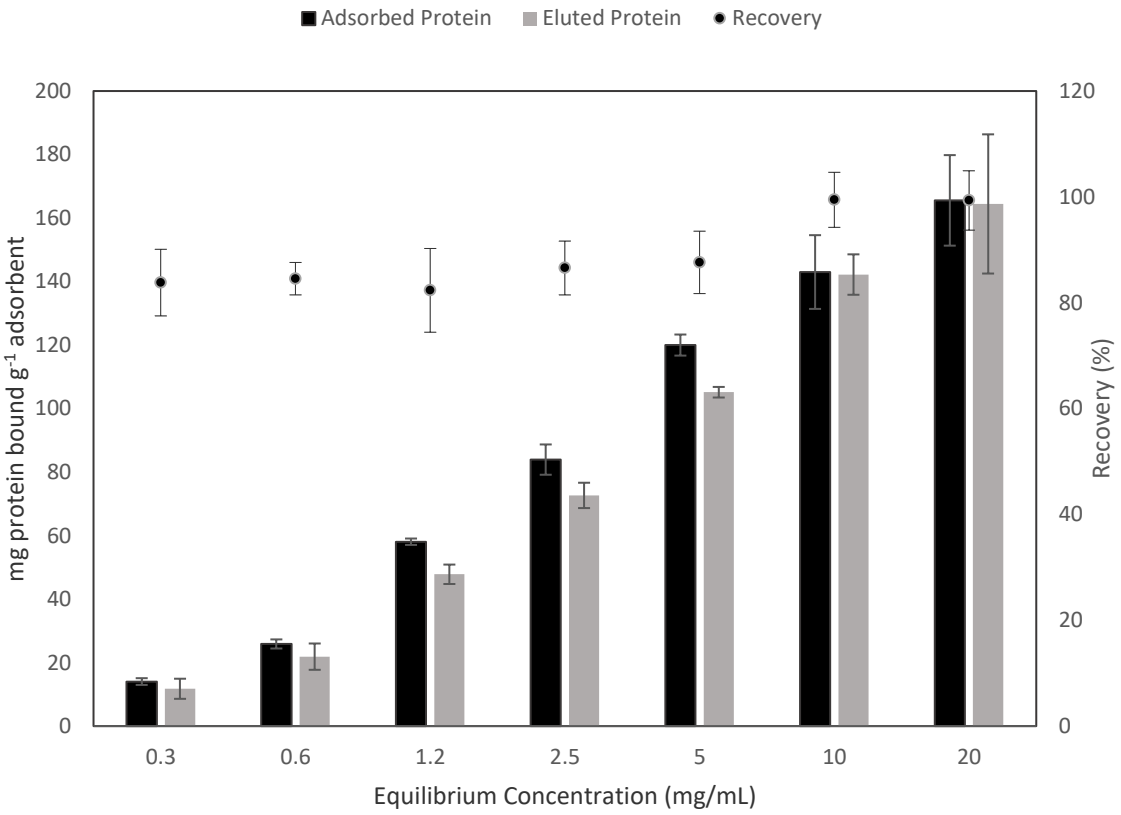

Figure 6-6. Adsorption and desorption of BSA on DEAE-functionalized SG-E2-400(78) polyHIPE at various concentrations. A triplicate sample was used for each resin. Error bars are ± one standard deviation.

6.2.2.3 Controlling the BSA absorbance on the polyHIPE anion exchanger at different flow rates

As stated in Section 6.2.2.3, a value for the binding capacity of an ion exchanger can be estimated by calculating the area between the two breakthrough profiles obtained when the system was run with and without an ion exchange column. For accurate determination of the capacity of functionalized polyHIPE (for N+ ions), a stream of mobile phase containing 2 mg mL^{-1} BSA in running buffer (10 mM Tris-HCl, pH 7.4) or in elution buffer (10 mM Tris-HCl 1 M NaCl, pH 7.4) was continuously fed through the DEAE functionalized and non-functionalized column until breakthrough was observed. The effect of the volume flow rates on BSA loading was also investigated by feeding the above mentioned mobile phase through the printed column at 0.50, 1.0, 2.0, 4.0, and 6.0 mL min^{-1}. To ensure the accuracy of the calculated adsorption capacity, the BSA binding capacity of the printed columns was also evaluated based on the recovered amount of BSA, represented by the elution and NaOH washing peak areas, so that the sum of the recovered and un-absorbed amount of BSA equals the loading mass of BSA, which was 20 mg in each cycle. Figure 6-7 shows the absorbance traces for all the steps in a cycle at 0.5 and 6 mL min^{-1} flow rates. The chromatograms for other flow rates are reported in Appendix C. The quantitative analysis of the BSA adsorption capacity of the printed column is presented in Table 6-1. As expected, the lowest binding of BSA to the printed

column occurs on un-functionalized monoliths with elution buffer as the mobile phase, suggesting that even without DEAE functionality and in the harsh high salt condition there was some affinity between the GMA-based polyHIPE monolith and BSA protein. Changing the mobile phase from high salt elution buffer on un-functionalized column to the running buffer increased the amount of bound BSA, especially for the weak binding which eluted during the elution step. With the use of DEAE-functionalized column in high salt mobile phase, more BSA protein bond to the column in comparison with the non-functionalized column. This binding appeared to be strong as there was no elution peak in the elution step and the bound protein desorbed only with passing NaOH. The highest binding of BSA was observed using running buffer and the functionalized monolith, as it expected. This behaviour was observed at all flow rates, although the amount of bound BSA decreased slightly with increasing flow rate because it effects the residence time of the protein solution inside the column.

a)

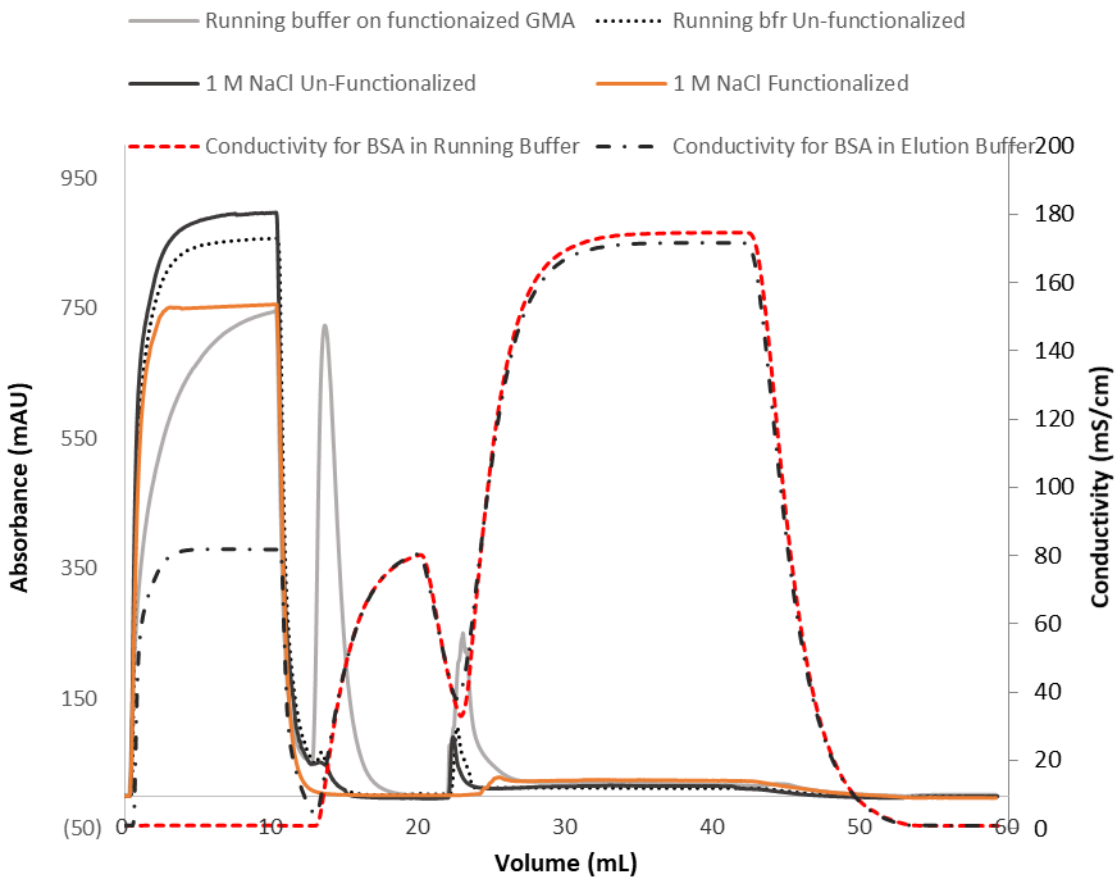
Running buffer on functionaized GMA
Running bfr Un-functionalized
1 M NaCl Un-Functionalized
1 M NaCl Functionalized
Conductivity for BSA in Running Buffer
Conductivity for BSA in Elution Buffer
Absorbance (mAU)
Conductivity (mS/cm)
Volume (mL)
950
750
550
350
150
(50)
200
180
160
140
120
100
80
60
40
20
0
0
10
20
30
40
50
60

b)

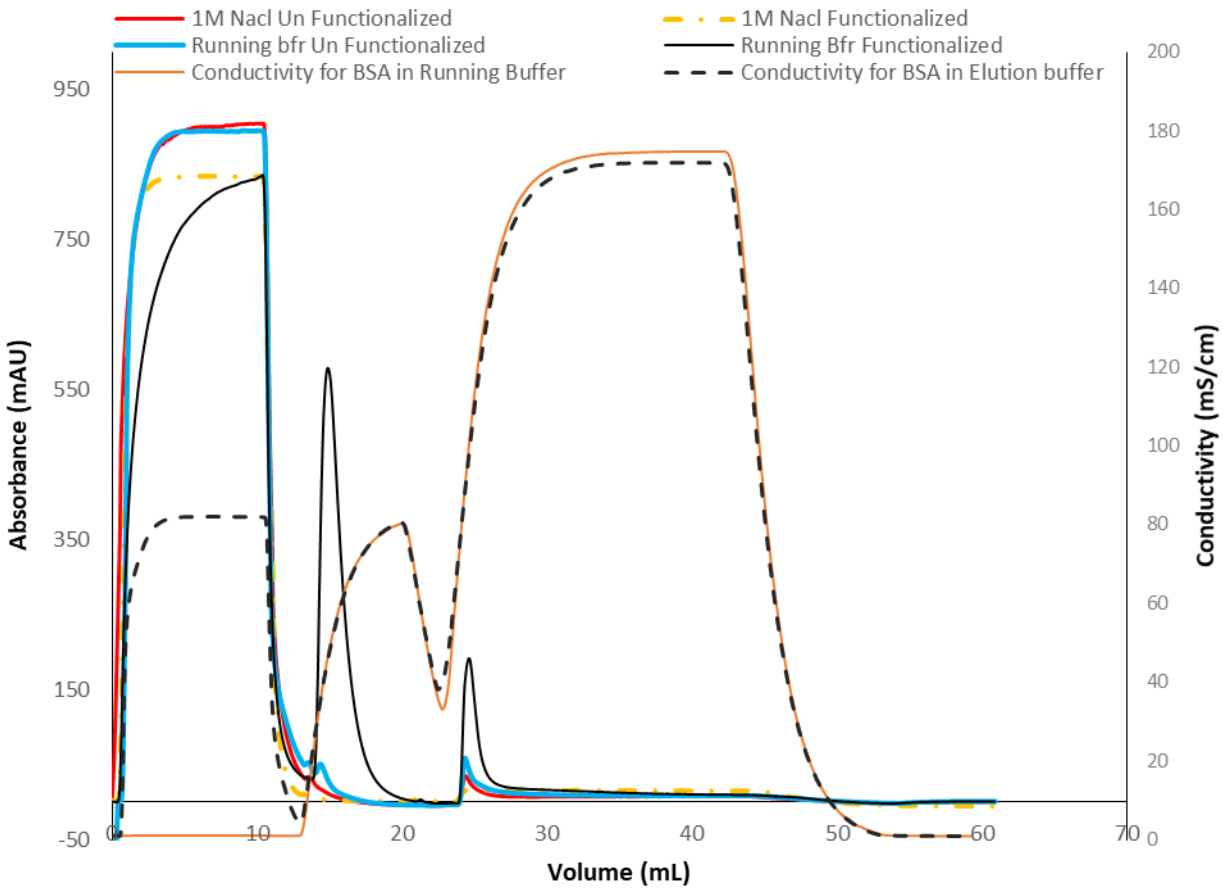

Figure 6-7. Chromatograph for 2 mg mL^{-1} BSA absorbance on printed SG-E2-400(78) column at a) 0.5 and b) 6 mL min-1 flow rates.

Table 6-1 shows the amount of BSA bound on the printed SG-E2-400(78) column and recovered in elution and NaOH washing steps at different flow rates. Recovery was defined as the percentage of the mass of BSA in the elution (elution and washing with NaOH) fraction per mass of the BSA in the feed solution. The BSA bound on the DEAE functional anion exchanger was

calculated from the difference between the absorbed BSA on the functionalized and un-functionalized columns. It can be concluded from the data presented in Table 1 that over 85% of bound BSA occurred on the DEAE anion exchange functionalities. It is also clear that by increasing the flow rate by a factor of 12×, the amount of absorbed BSA dropped by around 50%. This would be caused by slow protein diffusion from the liquid phase preventing access the whole of the monolith's surface with decreasing residence time, even though there might be improved mass transfer at higher flow rates as a result of higher shear rates [112, 113]. It is also noticeable that the BSA recoveries in the elution step and the combination of elution and washing steps increased with flow rate, which could have resulted from operation at higher shear rates.

However, the total recovered BSA in the eluted and washing with NaOH steps was greater than the BSA adsorbed during in the adsorption step, which might be due to the presence of other impurities from insufficient cleaning of monolith after synthesis in the system appearing in the UV adsorption signal.

Table 6-1. Average binding capacity and recovery for printed SG-E2-400(78) column in different flow rates.

Flow Rate (mL/min)	Mass of absorbed BSA (mg)		Mass of BSA in elution fraction (mg)	Mass of BSA in washing NaOH fraction (mg)	Total mass of BSA in washing and eluting fractions (mg)	Recovery (%)	
	Total absorbed	Absorbed on DEAE functional groups				Elution	Elution+washing with NaOH
0.5	5.46±0.32	5.16±0.41	2.96±0.11	2.53±0.27	5.49±0.38	54±1	100±1
1	5.22±0.24	4.88±0.25	2.84±0.18	2.44±0.19	5.28±0.37	54±1	100±2
2	5.01±0.14	4.37±0.13	2.82±0.2	2.22±0.21	5.04±0.41	56±2	100±5
4	3.61±0.08	2.9±0.10	2.64±0.11	1.74±0.09	4.38±0.20	73±1.5	121±3
6	3.31±0.16	2.84±0.15	2.55±0.12	1.48±0.13	4.03±0.25	77±0.5	121±1

6.2.2.4 Dynamic Binding Capacity

A closer view of the all chromatographs obtained in the previous section is shown in Figure 6-8 as the full breakthrough curves as a function of volumetric flow rate. Breakthrough occurs when the concentration of the chromatogram profile rises above zero that is the start of flow of the unbound protein through the column. Protein binding in dynamic mode minimizes mass transfer limitations by convection but reduces residence time, which results in lower binding than equilibrium binding.

From the breakthrough curve at arbitrary values of 10% or 50% protein breakthrough, the dynamic binding capacity (DBC) is found. The curves for 10% and 50% breakthrough are presented in Figure 6-9. The volume at which breakthrough occurred is expected to be lower with increasing flow rate. However, in the breakthrough curves presented in Figure 6-9, it can be seen that there is a little effect of flow rate on the breakthrough that might be because all the adsoption happens by convection at the monolith surface.

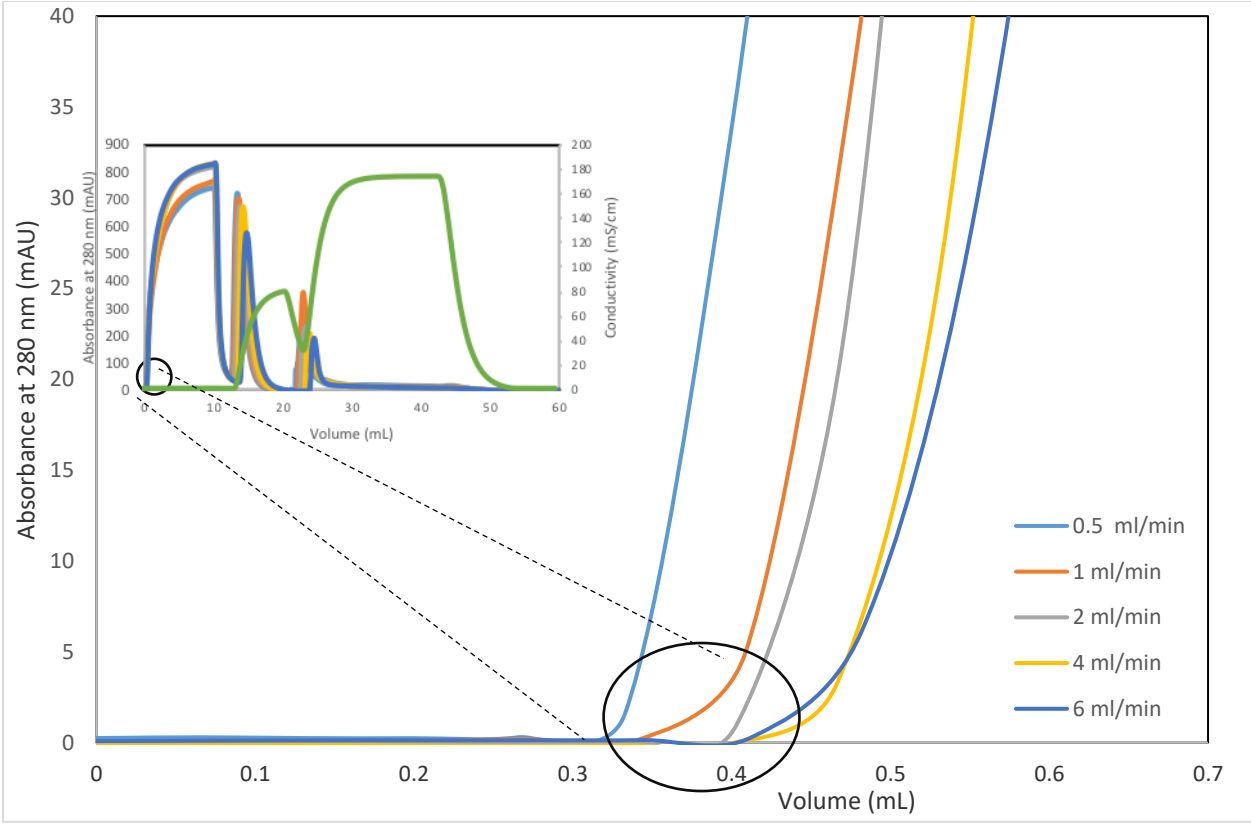

Figure 6-8. Breakthrough curves at different flow rates.

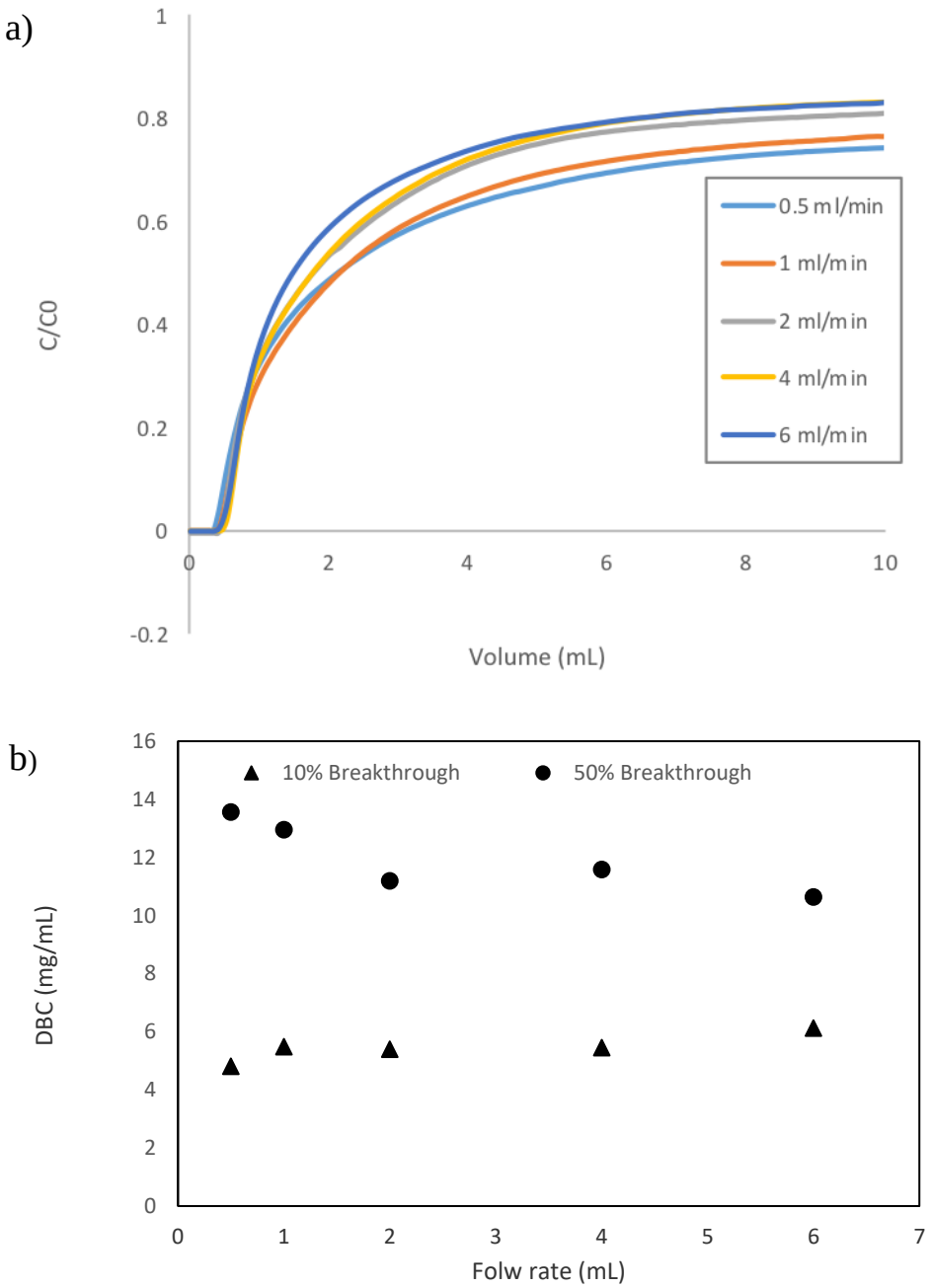

Figure 6-9. a) Breakthrough curves and b) determined dynamic binding capacity for 2 mg/ml BSA at different flow rates.

The DBC values for the printed SG SG-E2-400(78) monoliths were measured and are presented in Figure 6-9(c). These data are comparable with the DBC values that have been reported in the literature for various monoliths. The DBC of the DEAE-functionalized GMA-EGDMA polyHIPE monolith developed by Krajnc et al. [111] was 9 mg/mL at 50% breakthrough. Wang et al. [114] reported BSA binding capacity around 14 mg/mL at 10% breakthrough on polyethyleneimine (PEI) modified weak ion-exchanger based on a poly(GMA-co-EDMA) monolith. For commercial CIM-DEAE disks from BIA Separations, the BSA binding capacity at 3 mg/mL BSA and 1 mL/min flow rate was more than 21 mg/mL [115]. For other commercial weak anion exchange monoliths such as Toyopearl DEAE 650M and MacroPrep DEAE support, DBC values of 20 and 16 mg/mL was reported, respectively [116]. Although the DBC values measured for the printed SG-E2-400(78) monolith in this work were higher than the value reported by Krajnc et al. [111], they were lower than for other commercial or developed monoliths. Considering that flow rate, column size and protein concentration are very important for determining the binding capacity of a column [113, 117], it seems that the printed column in this work could be compared with commercial CIM-DEAE disks from BIA Separations that have almost the same size (diameter 12 mm and thickness 3 mm) and functionality (DEAE). For the comparison, the DBC of functionalized SG-E2-400(78) was measured at 1 mL min^{-1} flow rate loaded with 10 ml of 3 mg mL^{-1}

BSA solution. The resulting DBC was 15 mg BSA g^{-1} polyHIPE, which is lower than the reported value for commercial CIM-DEAE disks (21 mg BSA g^{-1} resin). On the other hand, the lower DBC value for the printed monolith could be due to the lower amount of solid phase in the column. For this particular print, 50% of the column volume is empty and thus the total mass of solid is approximately half that of the commercial one. Because the structure of polyHIPE has 78% inner porosity, only 20% to 30% of the bulk volume of material is solid, therefore less surface area is available to provide ion exchange sites. In comparison, in a bed of ion exchange resin beads 60% to 70% of the bulk volume is occupied by solid material, with significant internal porosity, providing more sites for ion exchange. In addition to the high porosity of polyHIPE, the total printed flow channel fraction of the designed monolith is 50% which means around just 10 to 15% solid material. Printed polyHIPEs therefore have potential for higher capacity than commercial or other reported monoliths that will be shown in Section 6.3.9.

6.2.2.5 Protein Separation

The chromatographic evaluation of the printed GMA-based polyHIPEs was performed with two dual protein mixtures containing myoglobin, BSA, and cytochrome C. The isoelectric points of these proteins are 7, 4.7 and 9.6, respectively. With the pH of the binding buffer equal to 7.4, the net charge of

myoglobin is approximately zero, BSA is negatively charged and cytochrome C is positively charged.

The first attempt to separate BSA/Cytochome C or BSA/myoglobin was conducted using a gradient elution of 0-100% buffer B over 30 minutes. Figure 6-10 shows that there were a clear and a ghost like elution peaks for the BSA/cytochrome C binary protein mixtures in these conditions.

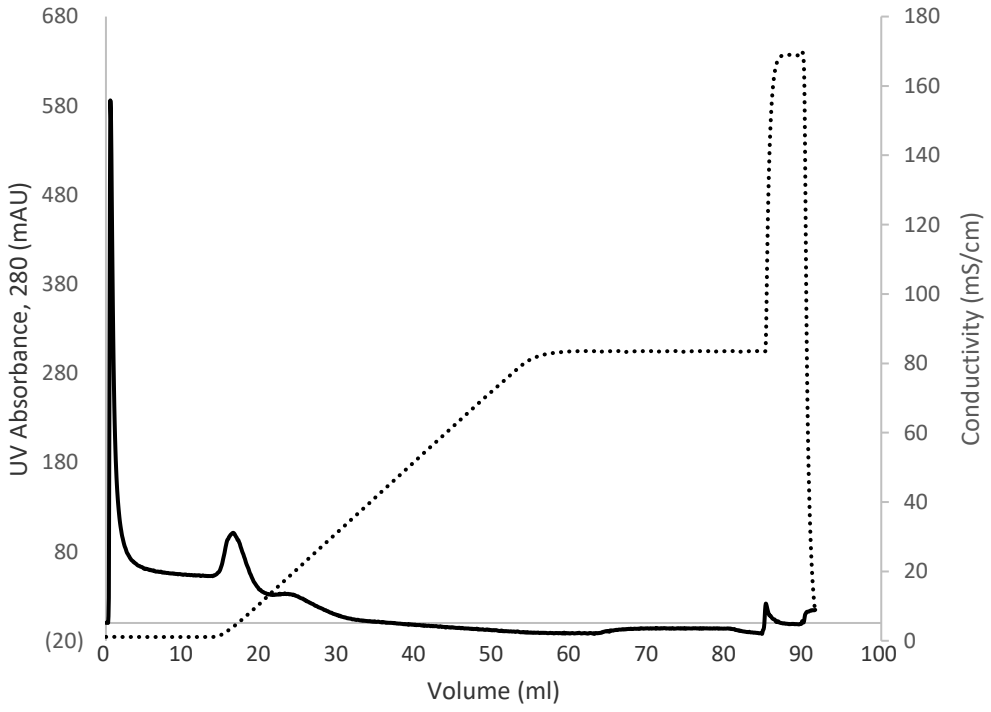

Figure 6-10. Linear gradient separation of a BSA/Cytochrome C (both at 3 mg/ml) protein mixture on a SG-E2-400(78) printed monolithic column. Conditions: mobile phase: buffer A: 10mM Tris–HCl buffer, pH 7.4; buffer B: 10mM Tris–HCl buffer+1M NaCl, pH 7.4; flow rate: 2 ml/min; linear gradient: 0-100% buffer B over 30 minutes.

However, elution using a step gradient, as described in Section 6.2.2.2.4, showed the two expected peaks from both mixtures. Figure 6-11 shows a chromatogram for the binary protein mixtures of BSA/myoglobin and their individual protein peaks. As expected, myoglobin, with zero net charge at pH 7.4, does not bind on the positively charged DEAE functionalized printed monolith. This result in an efficient separation of the binary mixture of BSA/Myoglobin, with a step gradient elution protocol. An SDS gel image of the binary mixture of BSA/myoglobin in the fractions collected during the chromatography run that is also shown in Figure 6-11(d), confirming good separation of BSA from myoglobin during elution, as there was no myoglobin detected in the elution fractions.

a)

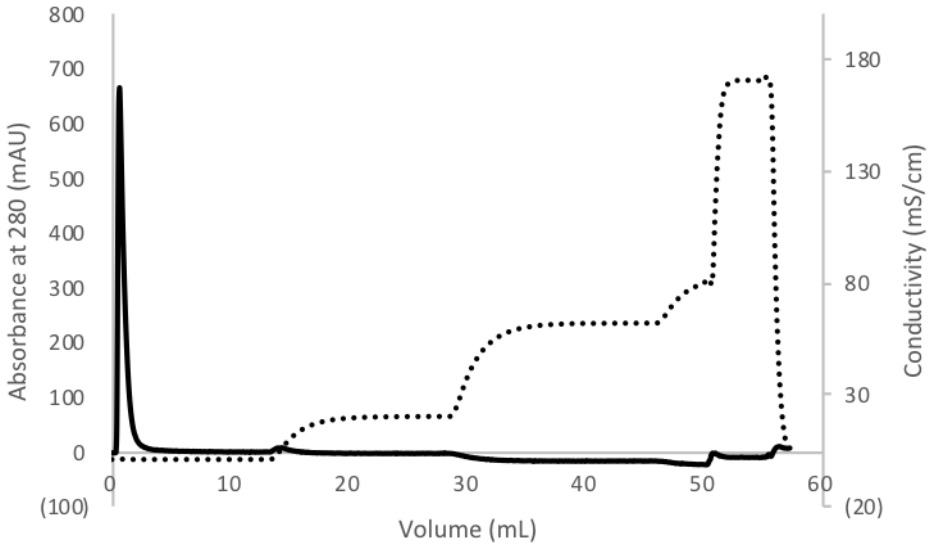

b)

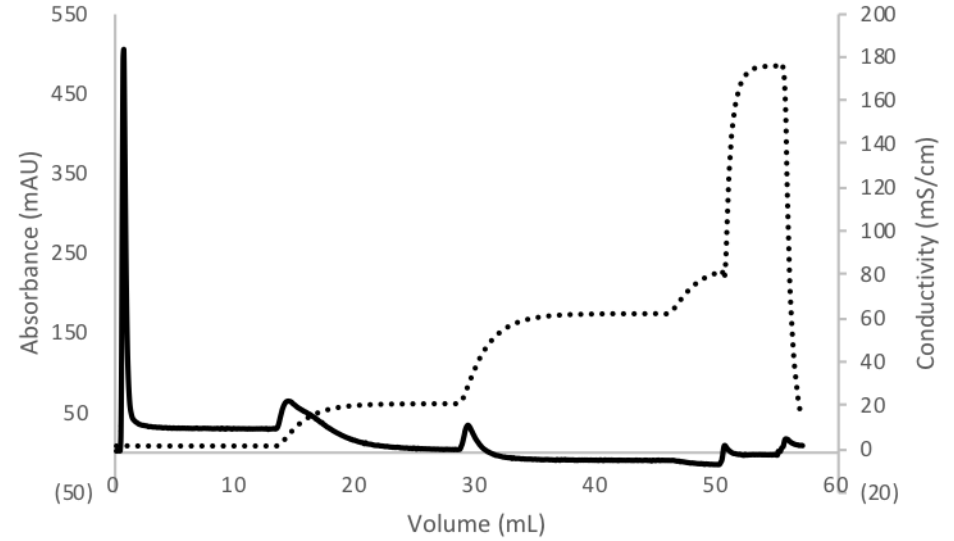
550
450
350
250
150
50
(50)
Absorbance (mAU)
0
10
20
30
40
50
60
Volume (mL)
200
180
160
140
120
100
80
60
40
20
0
(20)
Conductivity (mS/cm)

c)

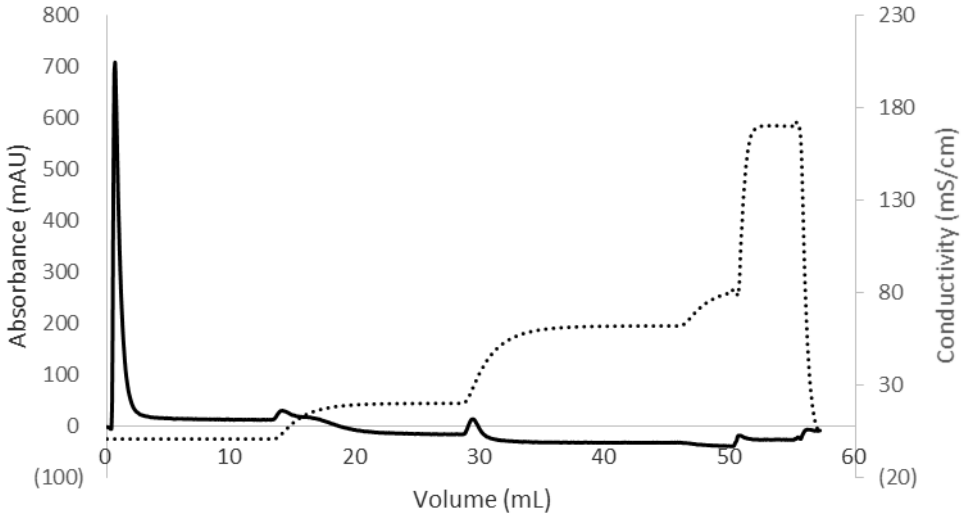
800
700
600
500
400
300
200
100
0
(100)
Absorbance (mAU)
0
10
20
30
40
50
60
Volume (mL)
230
180
130
80
30
(20)
Conductivity (mS/cm)

d)

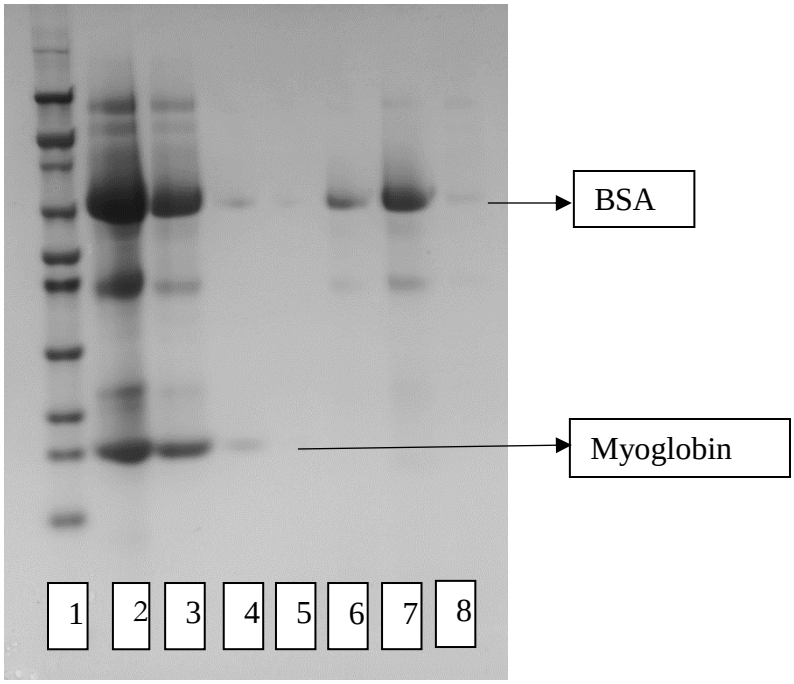

Figure 6-11. Chromatogram for a) BSA b) myoglobin and c) BSA/myoglobin mixture on printed SG-E2-400(78) polyHIPE monolithic columns. Conditions: mobile phase: buffer A: 10mM Tris–HCl buffer, pH 7.4; buffer B: 10mM Tris–HCl buffer+1M NaCl, pH 7.4; flow rate: 2 ml/min; step gradient: 20% buffer B, 70% buffer B. d) SDS-PAGE gel of selected fractions from BSA/myoglobin separation experiment. Lane 1: marker, Lane 2: feed solution, Lane 3: loading, Lanes 4, 5: washing step; Lanes 6, 7 and 8: elution steps.

However, the printed DEAE functionalized SG-E2-400(78) polyHIPE monolith did not show a good separation of BSA/cytochrome C, as shown in the chromatograms presented in Figure 6-12 and the SDS-PAGE gel in Figure 6-13. The result of SDS-PAGE gel shows that most of the loaded cytochrome C weakly bound to the DEAE functionalized monolith despite the positive charge of the weak anion exchange monolith. This is not in the agreement with the expected separation of BSA/Cytochrome C on an anion exchanger at pH 7.4, as

cytochrome C (PI> 7.4) is positively charged at pH 7.4 and consequently, the anion exchange SG-E2-400(78) with positive charges on the surface, should repel cytochrome C due to the electrostatic interactions. The weak binding of the cytochrome C on the DEAE functionalized monolith was confirmed with an experiment using 20% B as the binding buffer (Figure 6-14).

a)

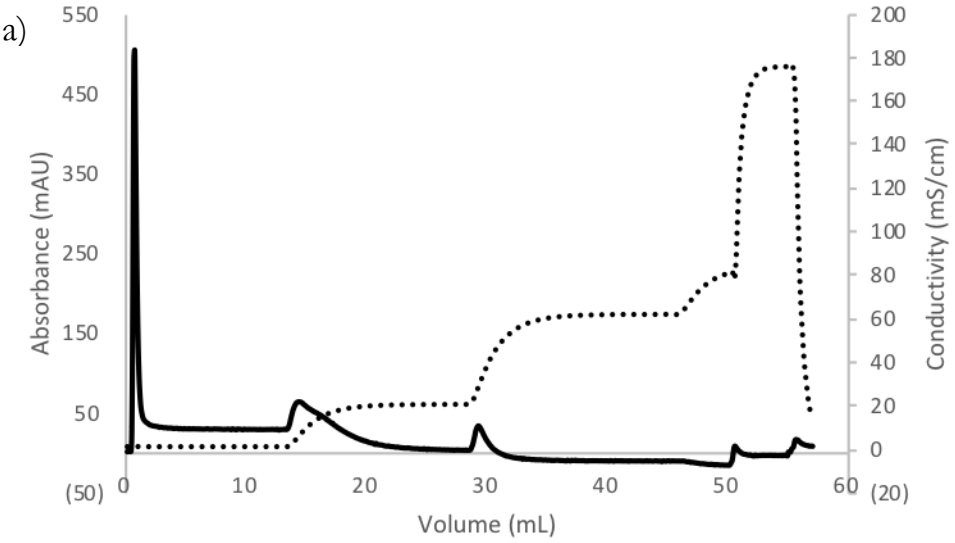
Absorbance (mAU)
550
450
350
250
150
50
(50)
0
10
20
30
40
50
60
Volume (mL)
200
180
160
140
120
100
80
60
40
20
0
(20)
Conductivity (mS/cm)

b)

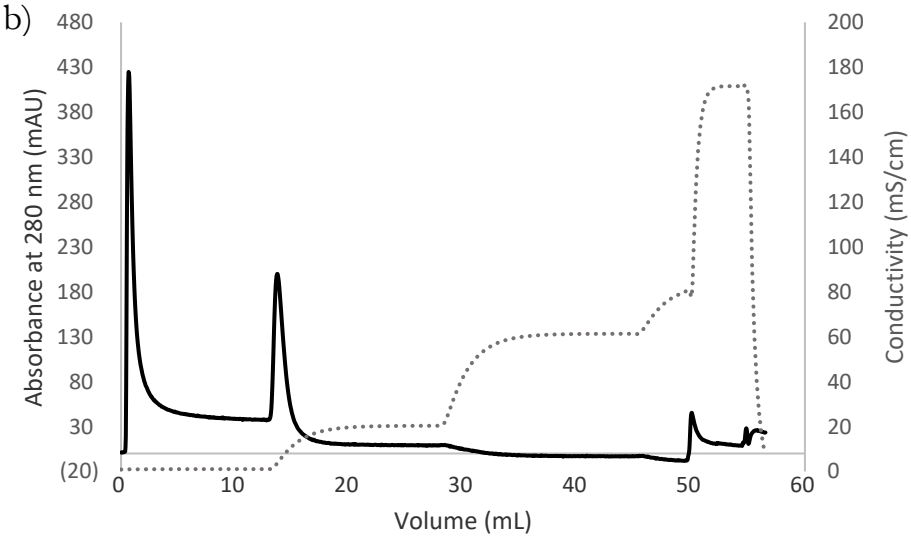
Absorbance at 280 nm (mAU)
480
430
380
330
280
230
180
130
80
30
(20)
0
10
20
30
40
50
60
Volume (mL)
200
180
160
140
120
100
80
60
40
20
0
Conductivity (mS/cm)

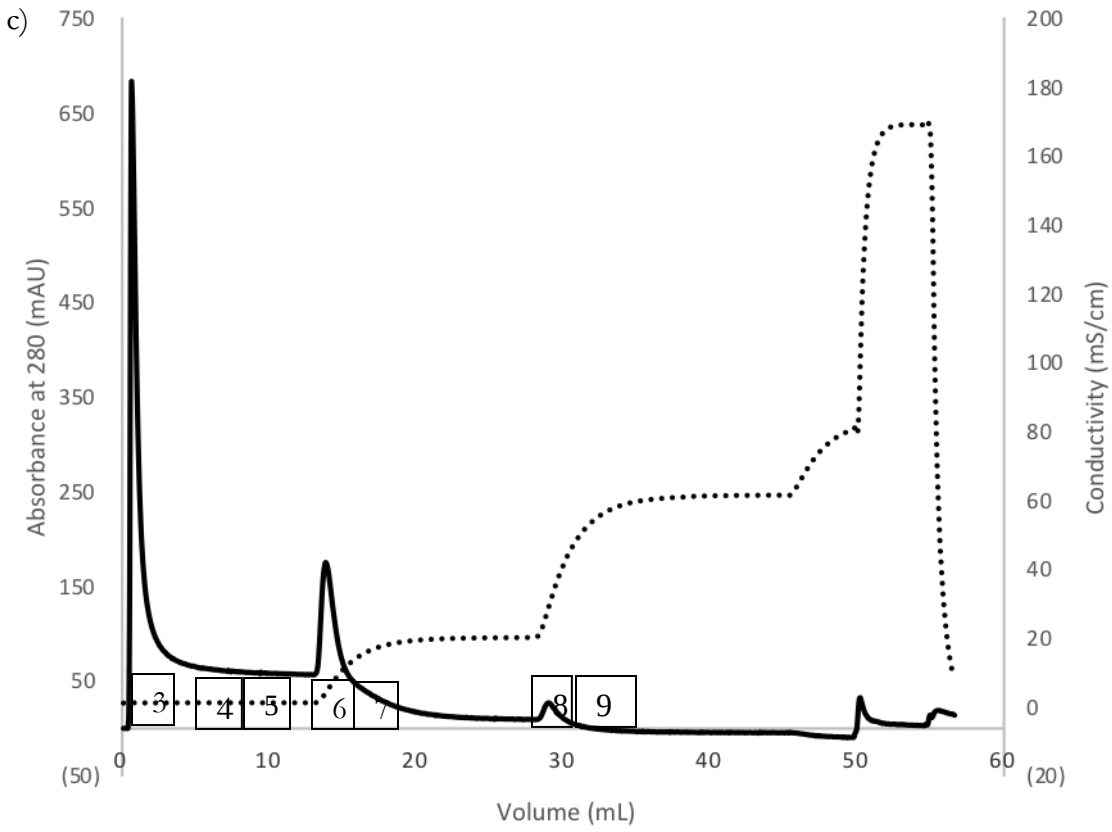

Figure 6-13. Chromatogram for a) BSA b) cytochrome C and c) BSA/cytochrome C mixture on printed SG-E2- polyHIPE monolithic columns. Conditions: mobile phase: buffer A: 10mM Tris–HCl buffer, pH 7.4; buffer B: 10mM Tris–HCl buffer+1M NaCl, pH 7.4; flow rate: 2 ml/min; step gradient: 20% buffer B, 70% buffer B. The fractions taken for SDS-PAGE gel were shown on the chromatogram.

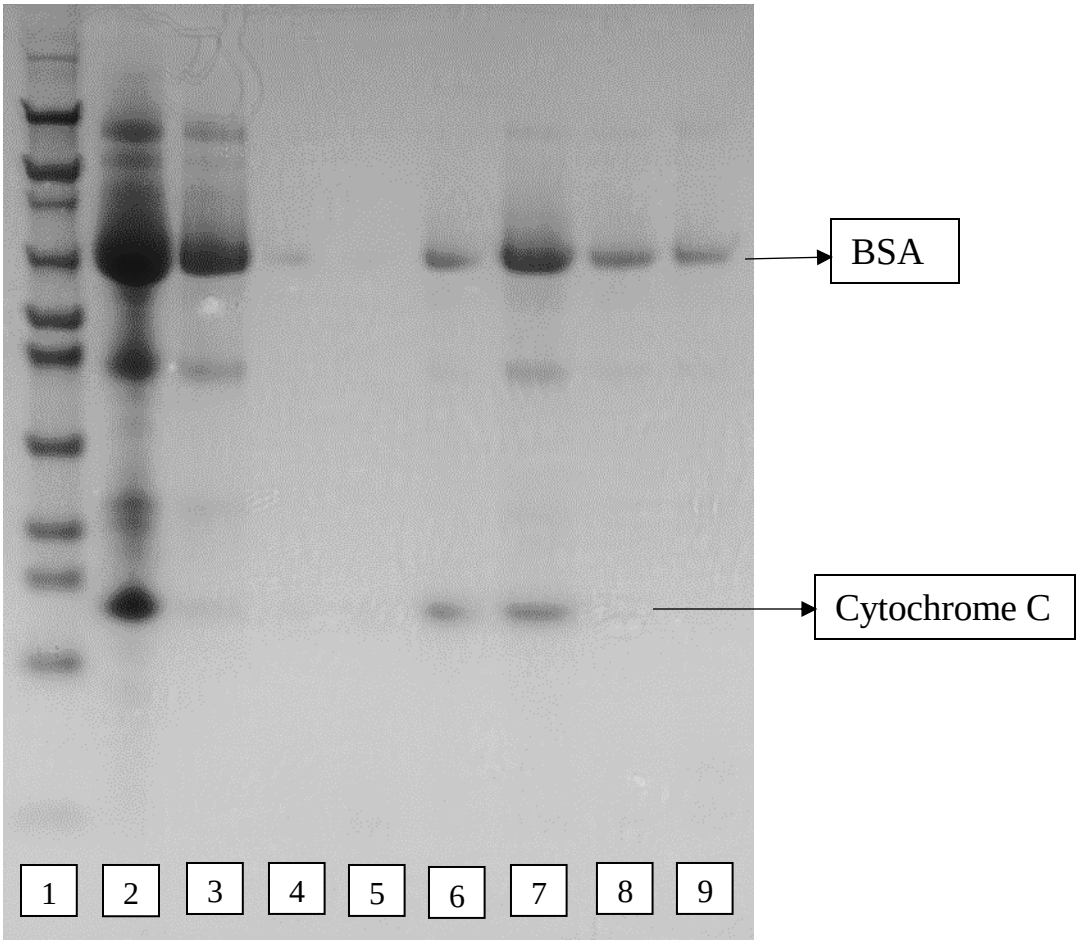

Figure 6-14. SDS-PAGE gel of selected fractions from BSA/cytochrome C separation axial-flow experiment. Lane1: marker, Lane 2: feed protein mixture solution, Lane 3: loading, Lane 4, 5: washing step; Lane 6, 7: elution step at 20% B; Lane 8, 9: elution step at 70% B.

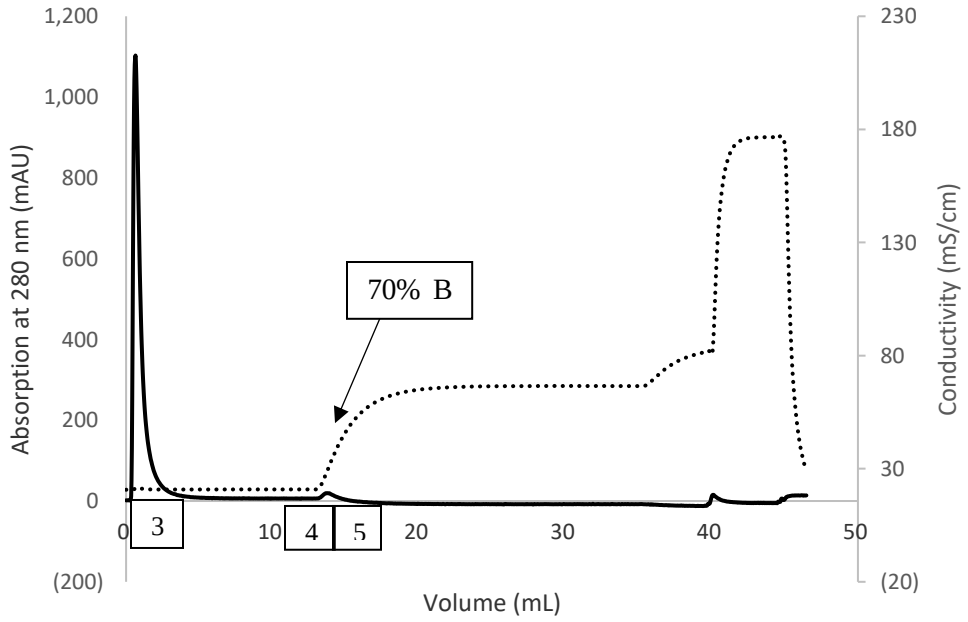
1,200
1,000
800
600
400
200
0
(200)
Absorption at 280 nm (mAU)
230
180
130
80
30
(20)
Conductivity (mS/cm)
70% B
0
10
20
30
40
50
Volume (mL)
3
4
5

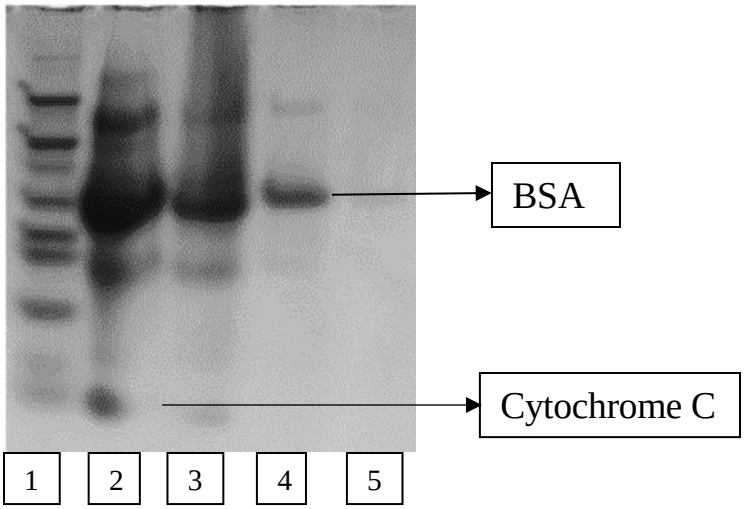
BSA
Cytochrome C
1
2
3
4
5

Figure 6-15. (a) Chromatogram for BSA/cytochrome C mixture with 20% buffer B (10 mM Tris-HCl, 1 M NaCl, PH 7.4) as binding buffer on printed SG-E2-400(78) polyHIPE monolithic columns, Conditions: mobile phase: buffer A: 10mM Tris–HCl buffer, pH 7.4; buffer B: 10mM Tris–HCl buffer+1M NaCl, pH 7.4; flow rate: 2 ml/min; step gradient: 70% buffer B (b) related SDS-PAGE gel represent a maker (Lane 1), feed protein mixture solution (Lane 2), fraction after loading (Lane 3), elution step at 70% B (Lane 4 and 5).

The weak binding of cytochrome C despite its positive charge suggests that there were some residual carboxylic groups with negative charges on the monolith surface. Considering these results, the active carboxylic groups on the printed SG-E2-400(78) polyHIPE monolith were deactivated according to the procedure described in Section 6.2.1.1.6. After deactivation, 3 mg/ml cytochrome C was injected onto the monolith to determine whether there was any absorption. Figure 6-15 compares the chromatogram for adsorption of 3 mg/ml cytochrome C on the carboxylic group-deactivated SG-E2-400(78) with the former column and indicates that there was a very small amount of cytochrome C bound on the deactivated monoliths, which could be caused by the van der Waals interactions between the monolith and the protein. Thus, residual carboxylic acid groups were likely responsible for the binding of cytochrome C on the original column, and then deactivation by capping with ethanolamine eliminated that binding.

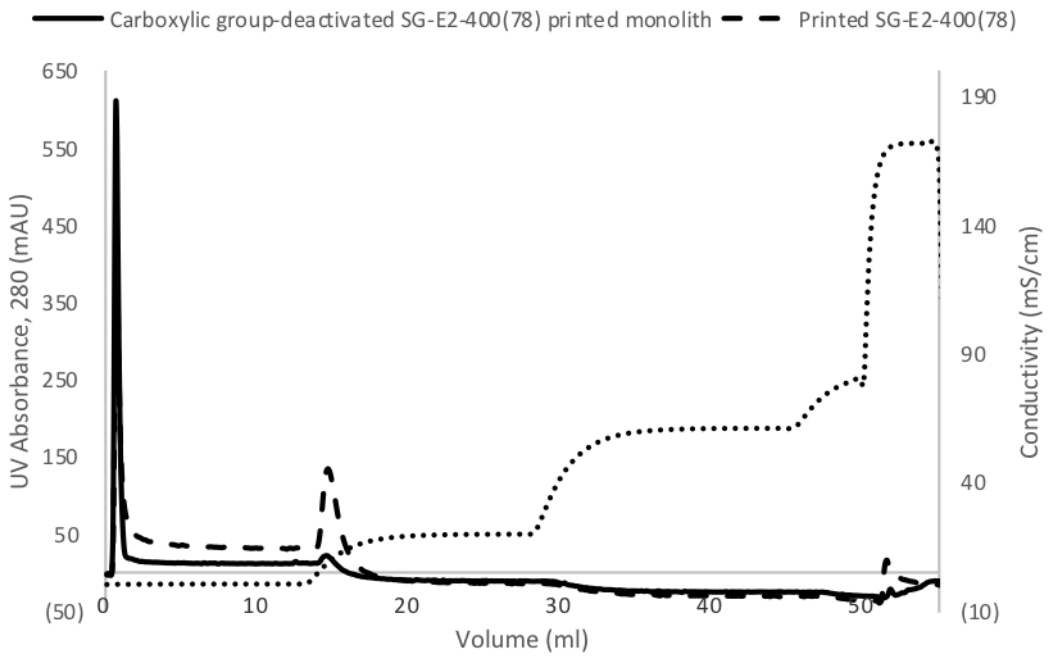

Figure 6-16. Comparison of cytochrome C adsorption on carboxylic group-deactivated SG-E2-400(78) and SG-E2-400(78) printed monoliths. Conditions: mobile phase: buffer A: 10mM Tris–HCl buffer, pH 7.4; buffer B: 10mM Tris–HCl buffer+1M NaCl, pH 7.4; flow rate: 2 ml/m

Following this, a binary mixture of BSA/cytochrome C was injected onto the carboxylic group-deactivated SG-E2-400(78) monolith and the chromatogram and SDS-PAGE gel results are presented in Figure 6-16, showing a complete separation of these proteins.

a)

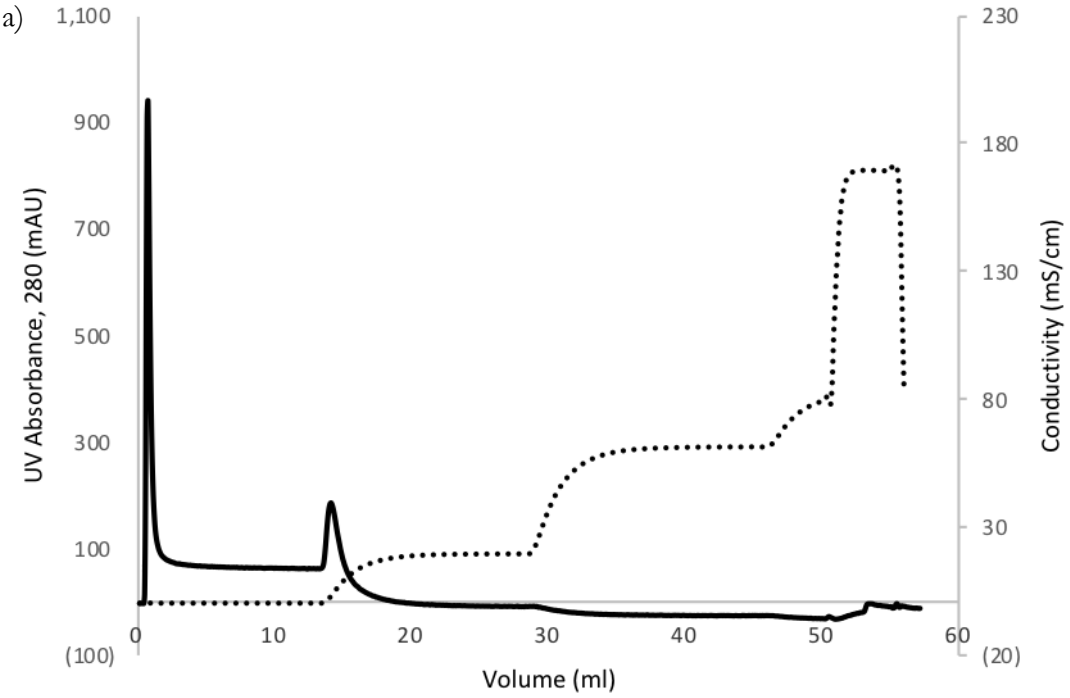
1,100
900
700
500
300
100
(100)
UV Absorbance, 280 (mAU)
230
180
130
80
30
(20)
Conductivity (mS/cm)
0
10
20
30
40
50
60
Volume (ml)

b)

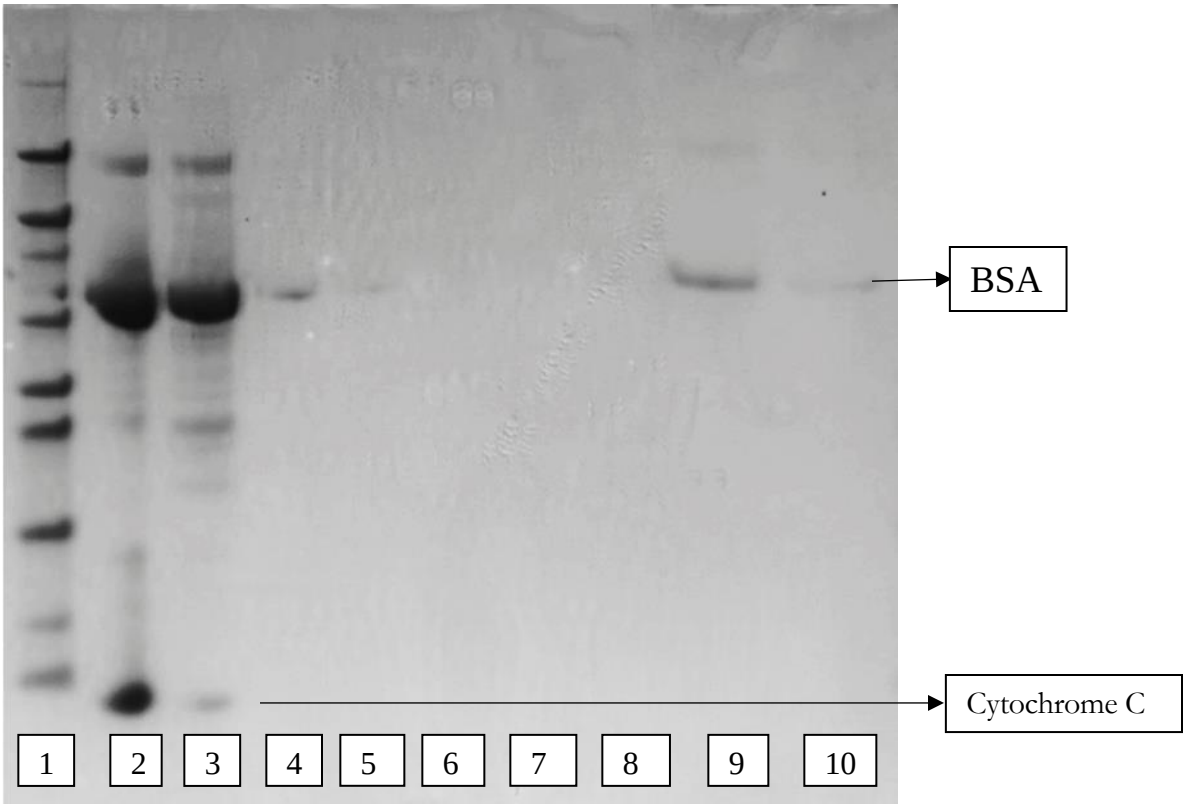

Figure 6-17. (a) Step gradient separation of BSA/cytochrome C binary mixture on carboxylic acid de-activated printed PolyHIPE monolithic columns. Conditions: mobile phase: buffer A: 10mM Tris–HCl buffer, pH 7.4; buffer B: 10mM Tris–HCl buffer+1M NaCl, pH 7.4; flow rate: 2 ml/min; step gradient: 20% buffer B, 70% buffer B (b) related SDS-PAGE gel represent a maker (Lane 1), feed protein mixture solution (Lane 2), loading the protein mixture (Lane 3,4 and 5),: washing step (Lane 6,7 and 8), elution step at 20% B (Lane 9 and 10).

6.2.3 Chromatographic performance of GMA/TEGDMA(60)/PEGDMA(40)

6.2.3.1 Static binding capacity of GMA/TEGDMA(60)/PEGDMA(40)

BSA binding to DEAE-functionalized GMA-TEGDMA(60)/PEGDMA(40) was assayed at different initial protein concentrations. Figure 6-17 shows the mechanically improved polyHIPE capacity plotted with increasing initial protein concentration on the x-axis. Comparison of Figure 6-17 with Figure 6-5 indicates that replacing the basic crosslinker (EGDMA) with higher molecular weight crosslinker (60% TEGDMA + 40% PEGDMA) slightly decreased the binding capacity of polyHIPE from 160 mg BSA g^{-1} (SG-E2-400(78)) to 140 mg BSA g^{-1} (GMA-TEGDMA(60)/PEGDMA(40)). This could be because of a decreased solid/protein solution contact area due to the lower SSA of GMA-TEGDMA(60)/PEGDMA(40).

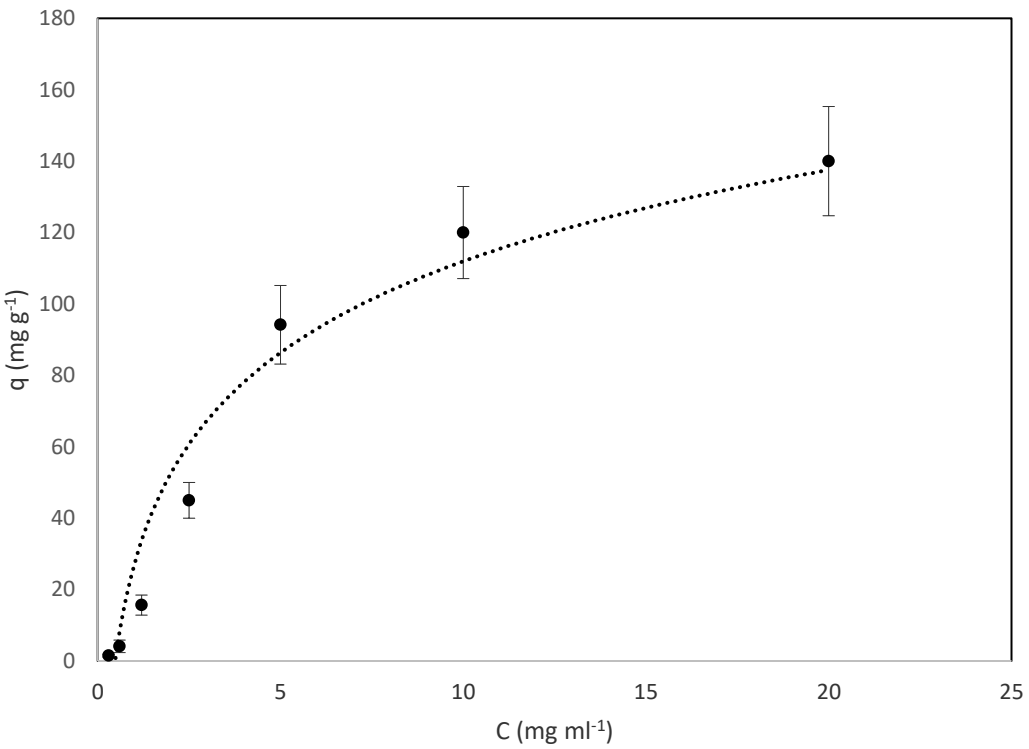

Figure 6-18. Static binding capacity of functionalized GMA-TEGDMA(60)/PEGDMA(40) for BSA. All measurements were at pH 7.4 and room temperature (20ºC). Error bars are ± one standard deviation.

6.2.3.2 Dynamic tests on GMA-TEGDMA(60)/PEGDMA(40)

To evaluate the chromatographic performance of mechanically improved GMA-based polyHIPE described in Chapter 5, a printed and functionalized GMA-TEGDMA(60)/PEGDMA(40) monolith was challenged for adsorption-desorption of 1 mg mL^{-1} BSA at 3 mL min^{-1} flow rate so that its breakthrough behaviour and dynamic binding capacity were compared with the previously discussed SG-E2-400(78) monolith. Figure 6-18 shows a comparison between the breakthrough curves of these monolithic columns and the column bypass,

without adsorption. Although the breakthrough occurred at the same volume for both monoliths, it is apparent that the modified GMA-TEGDMA(60)/PEGDMA(40) monoliths absorbed less BSA than the SG-E2-400(78) monolith. This is a result of the larger pore size and consequently lower specific surface area of GMA-TEGDMA(60)/PEGDMA(40) than the other polyHIPE, providing less accessible sites for functionalization as well as a lower liquid-solid contact area between the monolith backbone and the protein solution.

The sharpness of the breakthrough curve is indicative of the efficiency of mass transfer within the pores of the separation media. The breakthrough curve of the modified GMA-TEGDMA(60)/PEGDMA(40) monolithic column in Figure 18 is steeper than that of the modified SG-E2-400(78) monolith, indicating that the former monolith provided more efficient binding of proteins and higher resolution. This was previously observed by Li et al. [110] when comparing a poly (GMA- polyethylene glycol diacrylate (PEGDA)) bulk monolith with poly(GMA-co-EDMA) monolith. They suggested that the faster kinetic adsorption of proteins on poly(GMA-PEGDMA) could be attributed to decreased non-specific interaction of proteins with the monolith backbone when using PEGDA as a crosslinker [110].

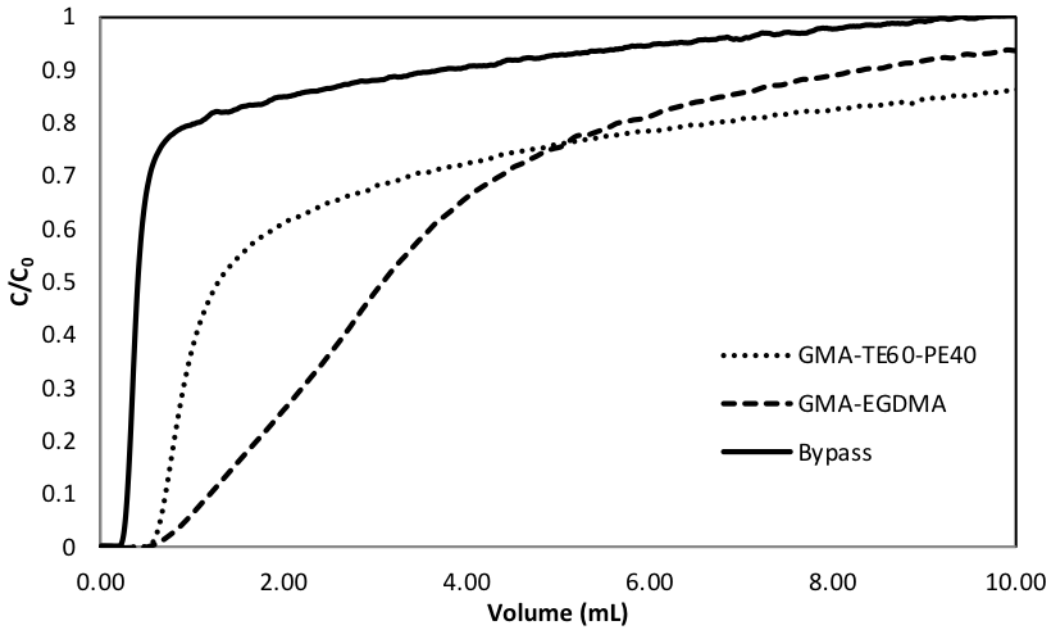

Figure 6-19. Breakthrough curves obtained by fontal analysis for DEAE modified GMA-TEGDMA(60)/PEGDMA(40), SG-E2-400(78) printed monolithic columns and bypass (no column).

6.2.3.3 Back pressure of the printed anion exchange monoliths

As shown in Figure 6-19, a linear dependency of the back pressure on velocity of the mobile phase for functionalized SG-E2-400(78) and GMA-TEGDMA(60)/PEGDMA(40) printed monoliths was achieved, which proves that the both porous printed monoliths were stable and were not compressed at high flow rate. The back pressure of the printed GMA-TEGDMA(60)/PEGDMA(40) monolithic column was lower for all the given flow rates in comparison with SG-E2-400(78). This might be caused by the larger pore sizes of GMA-TEGDMA(60)/PEGDMA(40) polyHIPE, discussed

in Chapter 5, which resulted in a higher permeability than that of SG-E2-400(78) monolith.

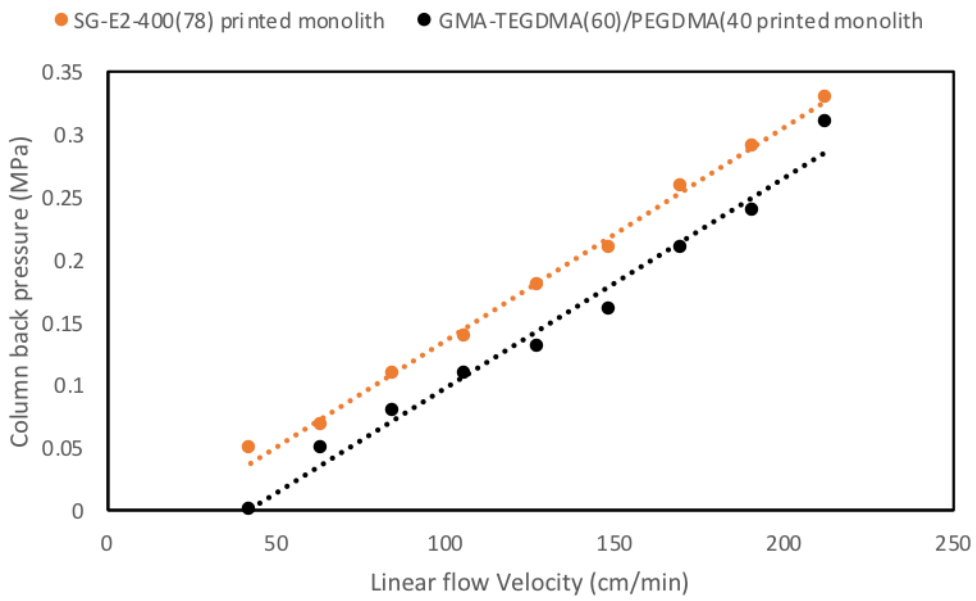

Figure 6-20. Dependency of back pressure on linear flow rate of mobile phase through DEAE-modified GMA-TEGDMA(60)/PEGDMA(40) and SG-E2-400(78) printed monolithic columns. Conditions: 3 mm×10 mm i.d. columns; mobile phase, 10 mM Tris buffer at pH 7.4.

6.2.3.4 Protein Separation

To investigate the chromatographic performance of the printed functionalized GMA-TEGDMA(60)/PEGDMA(40) monolith, a binary mixture of BSA/cytochrome C was injected onto the column and then a step gradient elution was performed under the same conditions as described above for the

printed SG-E2-400(78) column. Figure 6-20 shows the chromatogram and SDS-PAGE gel results for the separation test. Interestingly, the complete separation of BSA and cytochrome C occurred on the printed functionalized GMA-TEGDMA(60)/PEGDMA(40) monolith without the need for de-activation of the carboxylic groups. This is due to a lower number of residual carboxylic group in the higher molecular weight crosslinker, as the most of the chain in TEGDMA and PEGDMA contains methylene groups.

a)

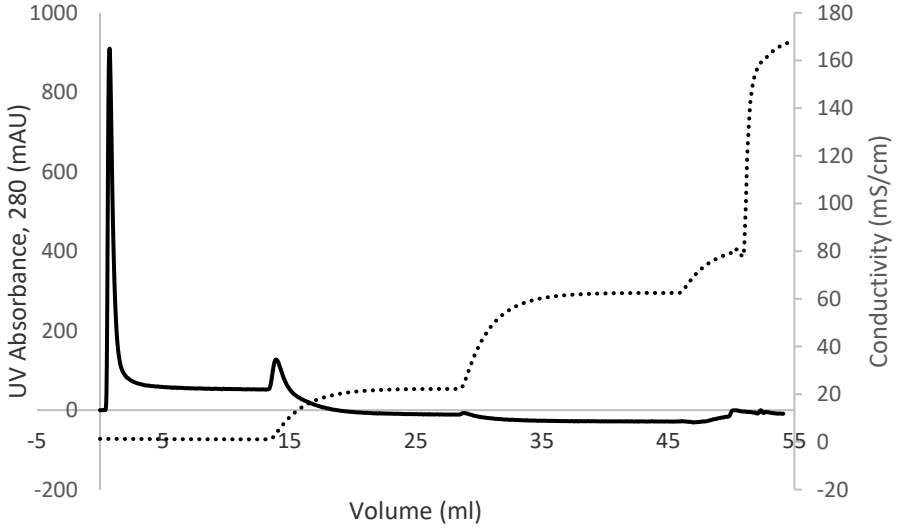

b)

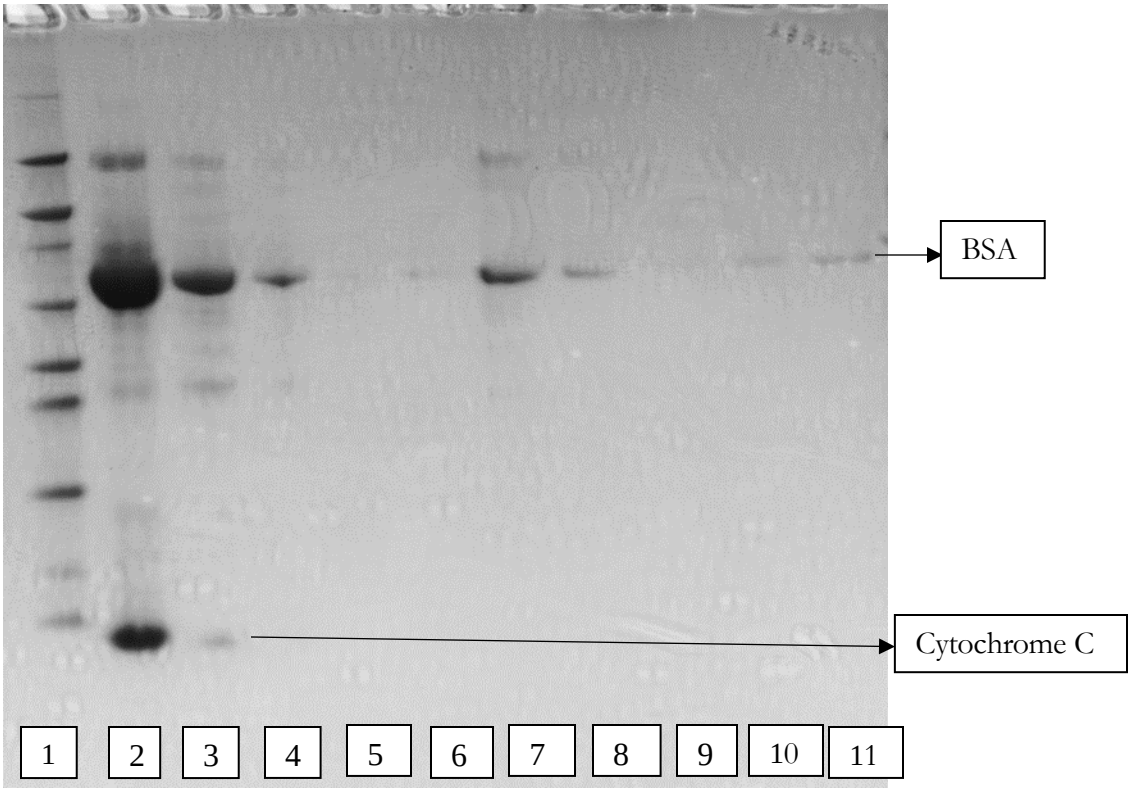

Figure 6-21. (a) Step gradient separation of BSA/cytochrome C binary mixture on carboxylic acid de-activated printed PolyHIPE monolithic columns. Conditions: mobile phase: buffer A: 10mM Tris–HCl buffer, pH 7.4; buffer B: 10mM Tris–HCl buffer+1M NaCl, pH 7.4; flow rate: 2 ml/min; step gradient: 20% buffer B, 70% buffer B (b) related SDS-PAGE gel represent a maker (Lane 1), feed protein mixture solution (Lane 2), loading the protein mixture (Lane 3,4 and 5),: washing step (Lane 6,7 and 8), elution step at 20% B (Lane 9, 10 and 11).

6.3 Conclusion

For the first time, a 3D printed weak anion exchange monolith was successfully developed using a DLP 3D printer, with functionalization with DEAE. The static BSA binding capacity of the basic polyHIPE (SG-E2-400(78)) had a maximum protein capacity of 160 mg BSA g^{-1} polyHIPE. Using a chromatography operation, the absorbance of BSA on the printed SG-E2-400(78) monolith was investigated to study the amount of the BSA absorbance on the weak anion exchanger group. The DBCs of the monoliths were measured at various flow rates and showed that increasing the flow rate from 0.5 to 6 ml min^{-1} decreased the DBC of the monoliths at 50% breakthrough from 13.56 to 10.64 mg ml^{-1} polyHIPE. These results are comparable with commercial and other GMA-based monoliths reported in the literature and concluded that although the binding capacities of the printed monoliths were lower than the other ones, they had a lower solid surface considering the 50% porosity design and 78% internal porosity. Complete separations of BSA/myoglobin and BSA/cytochrome C binary mixtures occurred on the SG-E2-400(78) monolithic column, as shown by SDS-PAGE, as long as the carboxylic acid groups in the backbone of SG-E2-400(78) monolith were deactivated for the separation of BSA/cytochrome C.

In the second section of this chapter, static binding capacity of BSA on a DEAE-functionalized GMA-TEGDMA(60)/PEGDMA(40) polyHIPE was studied and showed that the binding capacity of this tough polyHIPE was slightly lower than that of the basic polyHIPE, by 20 mg BSA per g^{-1} polyHIPE. The back pressure of both printed monoliths was evaluated and showed their back pressures at different flow rates were much lower than the commercial and other monoliths reported in the literature. The back pressure of the tough monolith was lower than that of the basic monolith and there was no compression under flow. The printed and functionalized GMA-TEGDMA(60)/PEGDMA(40) monolith separated cytochrome C from BSA completely, without the need for de-activation of carboxylic acid groups.

These results indicate that 3D printed polyHIPE monoliths, which are easily prepared and functionalized, have the potential for the use as the novel printed separation media

Chapter 7 Conclusions and recommendations for future work

7.1 Conclusions

The main objective of this thesis was to explore novel printing of monolithic columns with a complex geometry using a highly porous, interconnected structure of acrylic-based polyHIPE, which can be chemically modified for chromatography. The adopted approaches extended the use of 3D printing in creation of highly porous stationary phases with well-defined porosities, fine precision and scalability.

Macroporous GMA-based polyHIPE with a tuned porous structure was synthesised using photopolymerization. The average pore size and pore size distribution in the material was optimized using mixing conditions, proper surfactant concentration and internal phase volume ratio. The investigation

showed that a combination of an IKA propeller and a Probe Sonic Ruptor for stirring the template emulsion, using the volume of 21% surfactant relative to the oil phase and 78% of internal phase ratio resulted in a polyHIPE with an average pore size around 1 μm, a uniform pore size distribution and 17.6 m^2/g specific surface area. Attempts to increase the specific surface area using porogen solvents with different compatibilities with the polymer were not successful.

The toughness of GMA-based polyHIPE was improved by replacing EGDMA as the basic crosslinker with a mixture of higher molecular weight crosslinkers including TEGDMA and PEGDMA. The effect of replacing the crosslinkers on the macrostructures of polyHIPE was investigated by quantitative analysis of SEM images and measuring specific surface area by BET. The morphological studies showed the typical interconnected pore structure and specific surface area in the improved polyHIPEs. Mechanical studies showed that introducing higher molecular weight crosslinkers into polyHIPEs significantly increased compression strength and deformation at breakage as well as transforming the brittle behaviour of GMA-EGDMA polyHIPE to elastic behaviour on the stress-strain curve. This eliminated the undesirable brittleness and chalkiness commonly found in polyHIPE materials. The measured Young's modulus and average pore size of the prepared polyHIPEs passed through a peak with

increasing PEGDMA content in both crosslinker mixtures. The Young's modulus of GMA-based polyHIPEs containing 40% PEGDMA increased by 50% and the crush strength by 400% when compared with traditional GMA/ethylene glycol dimethylacrylate polyHIPEs. This improvement in mechanical properties suggested GMA-based polyHIPE with 60% TEGDMA and 40% PEGDMA in crosslinker mixture as a suitable candidate for the chromatographic stationary phase.

For the first time, a developed DLP 3D printer was used to create gyroid minimal surfaces from an emulsion templating technique with precisely defined morphologies, directly from computer aided design models and a close replication of the CAD model was achieved. The shape fidelity of the printed structure to the designed was controlled by constrain UV scattering, light penetration and by surface control methods. The morphological studies showed that the microstructure of printed polyHIPEs were comparable to those of bulk photopolymerized reference samples with the same range of pore and window sizes. Finally, monolithic columns with gyroid structures were printed with 50% external porosity.

The chromatographic performance of the printed GMA-based polyHIPE monolithic columns were tested as described in Chapter 6. For this, the printed columns were functionalized with DEAE as a weak anion exchanger. The

maximum static binding capacity of the basic polyHIPE was 160 mg BSA g^{-1} polyHIPE. The dynamic binding capacities of printed monoliths at different flow rates were measured, with a maximum of 13.56 mg ml^{-1} of BSA at 50% breakthrough and 0.5 ml min^{-1} flow rate. These values are around half those of commercial GMA-based monoliths with the same overall dimensions as the printed monolith. Given that there was 50% solid fraction in the printed gyriod and 78% internal porosity compared with the only 60-65% internal porosity in commercial CIM disks (Bio Separations), the binding capacity obtained is very promising. Binary mixtures of BSA/myoglobin and BSA/cytochrome C were injected onto the monolith and complete separation of both mixtures was obtained following de-activation of residual carboxylic groups on the monolith in the case of BSA/cytochrome C. The chromatographic performance of the mechanically improved printed monolith was also studied. The results showed that the improved monolith had a lower binding capacity than the basic monolith in both static and dynamic conditions but that a complete separation of both binary mixtures of the model proteins occurred on this monolith without requiring deactivation of carboxylic acid groups.

7.2 Recommendations for future work

In the present study, the IKA RW 20 DZM, Silverson mixer with an interchangeable tubular mixing unit and a Probe Sonic Ruptor 400 ultrasonic

probe were used and their performance for preparation of HIPE were compared. Combined use of the IKA RW 20 DZM and the Probe Sonic Ruptor 400 resulted in the smallest average pore size, most uniform pore size distribution and highest specific surface area of HIPE emulsions. Other types of homogenizers such as a high pressure homogenizer, as well as different mixing intensities or less/more time and pulses could be investigated to optimize the preparation of emulsions with the smallest and most uniform droplet sizes.

The base polyHIPE used throughout this study was GMA-EGDMA, with an average pore size around 1-2 μm and specific surface area in the range of 10-18 $m^2 g^{-1}$. Attempts to produce polyHIPEs with higher specific surface area by introducing porogenic solvents were not successful. Other methods such as using Friedel-Crafts chemistry to 'knit' together aromatic monomers using an external crosslinker or using Pickering-emulsion-templating could also be used to produce a high specific surface area base polymer to improve the chromatographic performance towards that of commercial monoliths.

When investigating the effect of high molecular weight crosslinkers on the mechanical behaviour of the GMA-based polyHIPE, the surfactant type and content were not varied. Considering that the best mechanically improved polyHIPE from this study, GMA-TE(60)-PE(40), had increased average pore sizes and decreased specific surface area, introducing another type of surfactant,

such as PEL-121 (~ 4400 MW), which might be more compatible with higher molecular weight crosslinkers and optimizing the surfactant content to achieve smaller average pore size and higher specific surface idea should be considered in future work.

The monolithic column printed in this study was based on a network gyroid unit cell with 50% porosity that resulted in 500 µm diameter monolith channels. Further exploration of printed monoliths with different geometries such as sheet gyroids or different porosities is necessary in future work. In addition, the HIPE emulsion bath of the costume built DLP 3D printer should be improved to print longer monoliths with a length of around 5-10 cm. For this, the stability of HIPE must be improved or the bath could be designed so that the HIPE in the bath can be continually refreshed during printing.

The chromatographic performance of printed monoliths for different types of chromatography such as cation exchange, hydrophobic interaction and reversed phase chromatography should be investigated. In this regard, the printed monolith for cation exchange chromatography should be modified with proper functionalities but residual carboxylic acids may be a potential starting point. For hydrophobic interaction and reversed phase chromatography, the base monomer (GMA) could be changed to a more hydrophobic monomer such as butyl methacrylate or phenyl dimethacrylate. In the current study, all

chromatographic characterization was done at a lab scale, therefore pilot scale and scale-up studies should be carried out in further research.

References

1. Fee, C., S. Nawada, and S. Dimartino, *3D printed porous media columns with fine control of column packing morphology*. Journal of Chromatography A, 2014. **1333**: p. 18-24.

2. Nawada, S., S. Dimartino, and C. Fee, *Dispersion behavior of 3D-printed columns with homogeneous microstructures comprising differing element shapes.* Chemical Engineering Science, 2017. **164**: p. 90-98.

3. Dolamore, F., C. Fee, and S. Dimartino, *Modelling ordered packed beds of spheres: The importance of bed orientation and the influence of tortuosity on dispersion.* Journal of Chromatography A, 2018. **1532**: p. 150-160.

4. Gordon, A., et al., *Protein Capture on 3D-printed Solid Tolerant Chromatography Columns for a Range of Chromatographic Functions.*, in *30th International Symposium on Preparative and Process Chromatography*. 2017: Philadelphia, PA.

5. Nicholas A. Sears, P.S.D., Elizabeth M. Cosgriff-Hernandez, *Emulsion Inks for 3D Printing of High Porosity Materials.* Macromol. Rapid Commun. , 2016.

6. Sušec, M., et al., *Hierarchically Porous Materials from Layer-by-Layer Photopolymerization of High Internal Phase Emulsions.* Macromolecular Rapid Communications, 2013. **34**(11): p. 938-943.

7. Johnson, D.W., et al., *Macrostructuring of Emulsion-templated Porous Polymers by 3D Laser Patterning.* Advanced Materials, 2013. **25**(23): p. 3178-3181.

8. Cooperstein, I., M. Layani, and S. Magdassi, *3D printing of porous structures by UV-curable O/W emulsion for fabrication of conductive objects.* Journal of Materials Chemistry C, 2015. **3**(9): p. 2040-2044.

9. Hentze, H.P. and M. Antonietti, *Porous Polymers and Resins*, in *Handbook of Porous Solids*. 2008.

10. Xie, Z., et al., *Porous Phosphorescent Coordination Polymers for Oxygen Sensing.* Journal of the American Chemical Society, 2010. **132**(3): p. 922-923.

11. Haupt, K. and K. Mosbach, *Plastic antibodies: developments and applications.* Trends in Biotechnology, 1998. **16**(11): p. 468-475.

12. Seo, J.S., et al., *A homochiral metal–organic porous material for enantioselective separation and catalysis.* Nature, 2000. **404**: p. 982.

13. Schulte, M.D., et al., *The effect of fluorine-substituted acrylate monomers on the electro-optical and morphological properties of polymer dispersed liquid crystals.* Liquid Crystals, 2000. **27**(4): p. 467-475.

14. Maier, G., *Low dielectric constant polymers for microelectronics.* Progress in Polymer Science, 2001. **26**(1): p. 3-65.

15. Karageorgiou, V. and D. Kaplan, *Porosity of 3D biomaterial scaffolds and osteogenesis.* Biomaterials, 2005. **26**(27): p. 5474-5491.

16. Kirschning, A., et al., *PASSflow Syntheses Using Functionalized Monolithic Polymer/Glass Composites in Flow-Through Microreactors.* Angewandte Chemie International Edition, 2001. **40**(21): p. 3995-3998.

17. Silverstein, M.S., *PolyHIPEs: Recent advances in emulsion-templated porous polymers.* Progress in Polymer Science 2014. **39**(1): p. 199-234.

18. Okay, O., *Macroporous copolymer networks.* Progress in Polymer Science, 2000. **25**: p. 711.

19. Thomas, S., et al., *Micro- and Nano-structured Interpenetrating Polymer Networks*, in *Micro- and Nano-structured Interpenetrating Polymer Networks*. 2016.

20. Cai, Y., et al., *Porous microsphere and its applications.* International Journal of Nanomedicine, 2013. **8**: p. 1111-1120.

21. Peters, E.C., F. Svec, and J.M.J. Frechet, *Rigid Macroporous Polymer Monoliths.* Advanced Materials, 1999. **11**(14): p. 1169.

22. Nischang, I., O. Brueggemann, and F. Svec, *Advances in the preparation of porous polymer monoliths in capillaries and microfluidic chips with focus on morphological aspects.* Analytical and Bioanalytical Chemistry, 2010. **397**: p. 953–960.

23. Dubinsky, S., et al., *Microfluidic Synthesis of Macroporous Copolymer Particles.* Macromolecules 2008. **41**: p. 3555-3561.

24. Gokmen, M.T., et al., *Fabrication of Porous "Clickable" Polymer Beads and Rods through Generation of High Internal Phase Emulsion (HIPE) Droplets in a Simple Microfluidic Device.* Macromolecules, 2009. **42**(23): p. 9289-9294.

25. Hentze, H.P. and M. Antonietti, *Porous polymers and resins for biotechnological and biomedical applications.* Reviews in Molecular Biotechnology, 2002. **90**(1): p. 27-53.

26. Silverstein, M.S., *PolyHIPEs: Recent advances in emulsion-templated porous polymers.* Progress in Polymer Science, 2014. **39**(1): p. 199-234.

27. Lissant, K.J., et al., *Structure of high-internal-phase-ratio emulsions.* Journal of Colloid and Interface Science, 1974. **47**(2): p. 416-423.

28. Lissant, K.J., *The geometry of high-internal-phase-ratio emulsions.* Journal of Colloid and Interface Science, 1966. **22**(5): p. 462-468.

29. Zhang, H., et al., *Synthesis of Hierarchically Porous Silica and Metal Oxide Beads Using Emulsion-Templated Polymer Scaffolds.* Chemistry of Materials, 2004. **16**: p. 4245-4256.

30. Štefanec, D. and P. Krajnc, *Aryl acrylate porous functional polymer supports from water-in-oil-in-water multiple emulsions.* Polymer International, 2007. **56**(10): p. 1313-1319.

31. Welch, C.F., et al., *Rheology of High Internal Phase Emulsions.* Langmuir, 2006. **22**(4): p. 1544-1550.

32. Das, A.K., et al., *Concentrated emulsions. 3. Studies on the influence of continuous-phase viscosity, volume fraction, droplet size, and temperature on emulsion viscosity.* Langmuir, 1992. **8**(10): p. 2427-2436.

33. Babak, V.G. and M.-J. Stébé, *Highly Concentrated Emulsions: Physicochemical Principles of Formulation.* Journal of Dispersion Science and Technology, 2002. **23**(1-3): p. 1-22.

34. Hughes, J.M., *Development Of PolyHIPE Chromatography And Lanthanide-Doped Latex Particles For Use In The Analysis Of Engineered Nanoparticles*. 2013, The University of Manchester.

35. Cameron, N.R., *High internal phase emulsion templating as a route to well-defined porous polymers.* Polymer, 2005. **46**(5): p. 1439-1449.

36. Cameron, N.R., et al., *Study of the formation of the open-cellular morphology of poly(styrene/divinylbenzene) polyHIPE materials by cryo-SEM.* Colloid and Polymer Science, 1996. **274**(6): p. 592-595.

37. Menner, A. and A. Bismarck, *New Evidence for the Mechanism of the Pore Formation in Polymerising High Internal Phase Emulsions or Why polyHIPEs Have an Interconnected Pore Network Structure.* Macromolecular Symposia, 2006. **242**(1): p. 19-24.

38. Zhang, H. and A.I. Cooper, *Synthesis of Monodisperse Emulsion-Templated Polymer Beads by Oil-in-Water-in-Oil (O/W/O)*

Sedimentation Polymerization. Chemistry of Materials, 2002. **14**(10): p. 4017-4020.

39. Barbetta, A., et al., *Tailoring the Porosity and Morphology of Gelatin-Methacrylate PolyHIPE Scaffolds for Tissue Engineering Applications.* Langmuir, 2005. **21**(26): p. 12333-12341.

40. Barbetta, A. and N.R. Cameron, *Morphology and Surface Area of Emulsion-Derived (PolyHIPE) Solid Foams Prepared with Oil-Phase Soluble Porogenic Solvents: Span 80 as Surfactant.* Macromolecules, 2004. **37**(9): p. 3188-3201.

41. Barbetta, A. and N.R. Cameron, *Morphology and Surface Area of Emulsion-Derived (PolyHIPE) Solid Foams Prepared with Oil-Phase Soluble Porogenic Solvents: Three-Component Surfactant System.* Macromolecules, 2004. **37**(9): p. 3202-3213.

42. Carnachan, R.J., et al., *Tailoring the morphology of emulsion-templated porous polymers.* Soft Matter, 2006. **2**(7): p. 608-616.

43. Lee, C.T., et al., *Water-in-Carbon Dioxide Emulsions: Formation and Stability.* Langmuir, 1999. **15**(20): p. 6781-6791.

44. Kronberg, j.K.A.B., *On the Formation and Stability of Concentrated Water-in-Oil Emuslions, Aphrons.* Colloids and Surfaces A, 1990. **50** p. 131-140.

45. Reynolds, P.A., et al., *Structure of High Internal Phase Aqueous-in-Oil Emulsions and Related Inverse Micelle Solutions. 3. Variation of Surfactant.* The Journal of Physical Chemistry B, 2009. **113**(36): p. 12231-12242.

46. Capdevila, M., et al., *Preparation of Span 80/oil/water highly concentrated emulsions: Influence of composition and formation variables and scale-up.* Journal of Colloid and Interface Science, 2010. **345**(1): p. 27-33.

47. Chen, H.H. and E. Ruckenstein, *Effect of the nature of the hydrophobic oil phase and surfactant in the formation of concentrated emulsions.* Journal of Colloid and Interface Science, 1991. **145**(1): p. 260-269.

48. Ikem, V.O., A. Menner, and A. Bismarck, *High Internal Phase Emulsions Stabilized Solely by Functionalized Silica Particles.* Angewandte Chemie International Edition, 2009. **48**(4): p. 632-632.

49. Menner, A., et al., *Particle-Stabilized Surfactant-Free Medium Internal Phase Emulsions as Templates for Porous Nanocomposite Materials: poly-Pickering-Foams.* Langmuir, 2007. **23**(5): p. 2398-2403.

50. Cetinkaya, S., E. Khosravi, and R. Thompson, *Supporting ruthenium initiator on PolyHIPE.* Journal of Molecular Catalysis A: Chemical, 2006. **254**(1): p. 138-144.

51. Krajnc, P., J.F. Brown, and N.R. Cameron, *Monolithic Scavenger Resins by Amine Functionalizations of Poly(4-vinylbenzyl chloride-co-divinylbenzene) PolyHIPE Materials.* Organic letters, 2002. **4**(15): p. 2497-2500.

52. Jerenec, S., et al., *Glycidyl methacrylate and ethylhexyl acrylate based polyHIPE monoliths: Morphological, mechanical and chromatographic properties.* Reactive and Functional Polymers, 2014. **78**: p. 32-37.

53. Hayman, M.W., et al., *Enhanced neurite outgrowth by human neurons grown on solid three-dimensional scaffolds.* Biochemical and biophysical research communications, 2004. **314**(2): p. 483-488.

54. Schwab, M.G., et al., *High surface area polyHIPEs with hierarchical pore system.* Soft Matter, 2009. **5**(5): p. 1055-1059.

55. Çira, F. and E.H. Mert, *PolyHIPE/pullulan composites derived from glycidyl methacrylate and 1,3-butanediol dimethacrylate-based high internal phase emulsions.* Polymer Engineering & Science, 2015. **55**(11): p. 2636-2642.

56. Haibach, K., et al., *Tailoring mechanical properties of highly porous polymer foams: Silica particle reinforced polymer foams via emulsion templating.* Polymer, 2006. **47**(13): p. 4513-4519.

57. Robert J. Groarke, a.D.B., *Methacrylate Polymer Monoliths for Separation Applications.* Materials 2016. **9**: p. 446.

58. Podgornik, A. and N.L. Krajnc, *Application of monoliths for bioparticle isolation.* Journal of Separation Science, 2012. **35**(22): p. 3059-72.

59. Radim Knob, V.S., Mukul Sonker, and Adam T.Woolley, *Advances in monoliths and related porous materials for microfluidic.* Biomicrofluidics 2016. **10**: p. 032901.

60. Sidratul Choudhury, D.C.a.B.a.W., *Supermacroporous polyHIPE and cryogel monolithic materials as stationary phases in separation science: a review.* Anal. Methods,, 2015(7): p. 6967.

61. Sebastjan Huˇsa, M.K., Peter Krajnc, *Separation of heavy metals from water by functionalized glycidyl methacrylate poly (high internal phase emulsions).* Journal of Chromatography A, , 2016. **1437** p. 168-175.

62. Kovačič, S. and P. Krajnc, *Macroporous monolithic poly(4-vinylbenzyl chloride) columns for organic synthesis facilitation byin situpolymerization of high internal phase emulsions.* Journal of Polymer Science Part A: Polymer Chemistry, 2009. **47**(23): p. 6726-6734.

63. Yeliz Tunc¸ Cigdem Gölgelioglu, N.H., Kezban Ulubayram, Ali Tuncel, *Acrylic-based high internal phase emulsion polymeric monolith for capillary electrochromatography.* Journal of Chromatography A, 2010. **1217** p. 1654-1659.

64. Chunhe Yao, L.Q., Hongying Jia, Peiyong Xin, Gengliang Yang and Yi Chen, *A novel glycidyl methacrylate-based monolith with sub-micron skeletons and well-defined macropores.* J. Mater. Chem., 2009. **19**: p. 767-772.

65. Yao, C.H., et al., *Preparation of sub-micron skeletal monoliths with high capacity for liquid chromatography.* Journal of Separation Science, 2010. **33**: p. 475-483.

66. Krajnc, P., et al., *Preparation and characterisation of poly(high internal phase emulsion) methacrylate monoliths and their application as separation media.* Journal of Chromatography A, 2005. **1065**: p. 69-73.

67. Jerenec, S., et al., *Glycidyl methacrylate and ethylhexyl acrylate based polyHIPE monoliths: Morphological, mechanical and chromatographic properties.* React. Funct. Polym., 2014. **78**: p. 32-37.

68. Theato, P. and H.-A. Klok, *Functional Polymers by Post-Polymerization Modification concepts, guidlines, and application*. 2013: Wiley-VCH.

69. Krajnc, P., et al., *Aryl Acrylate Based High-Internal-Phase Emulsions as Precursors for Reactive Monolithic Polymer Supports.* Journal of Polymer Science Part A: Polymer Chemistry, 2005. **43**: p. 296–303.

70. Majer J and K. P, *Cross-linked porous poly(acrylic acid-coacrylamide) from high internal phase emulsions: preparation and functionalisation.* Acta Chimica Slovenica, 2009. **56**: p. 629–634.

71. Theato, P. and H.K. Klok, *Functional Polymers by Post-Polymerization Modification: Concepts, Guidelines and Applications*. 2012: Wiley.

72. Brown, J.F., P. Krajnc, and N.R. Cameron, *PolyHIPE Supports in Batch and Flow-Through Suzuki Cross-Coupling Reactions.* Industrial & Engineering Chemistry Research, 2005. **44**(23): p. 8565-8572.

73. Jones, K., et al., *Porous polymers*. 1987, Google Patents.

74. Jomes, K., et al., *Porous polymers*. 1986, Google Patents.

75. Benicewicz, B.C., et al., *Open-celled polymeric foam monoliths for heavy metal separations study.* Journal of Radioanalytical and Nuclear Chemistry, 1998. **235**(1): p. 31-35.

76. Haq, Z., *Porous cross-linked absorbent polymeric materials*. 1985, Unilever PLC Unilever NV

77. Hainey, P., et al., *Synthesis and Ultrastructural Studies, of Styrene-Divinylbenzene Polyhipe Polymers.* Macromolecules 1991. **24**: p. 117-121.

78. Weiner, N.D., *Emulsions and emulsion technology, part I (volume 6 in surfactant science series). Edited by Kenneth J. Lissant. Marcel Dekker, 305 E. 45th St., New York, NY 10017, 1974. 440 pp. 15.5 × 23 cm. Price $39.50.* Journal of Pharmaceutical Sciences, 1975. **64**(8): p. 1434-1434.

79. Michael Layani, I.C.a.S.M., *UV crosslinkable emulsions with silver nanoparticles for inkjet printing of conductive 3D structures.* J. Mater. Chem. C,, 2013. **1**: p. 3244.

80. David W. Johnson , C.S., Matthew P. Didsbury , Christopher Pateman , Neil R. Cameron , and Frederik Claeyssens, *Macrostructuring of Emulsion-templated Porous Polymers by 3D Laser Patterning.* Adv. Mater., 2013. **25**: p. 3178-3181.

81. Maja Susec , S.C.L., Jürgen Stampfl , Robert Liska , Peter Krajnc, *Hierarchically Porous Materials from Layer-by-Layer Photopolymerization of High Internal Phase Emulsions.* Macromol. Rapid Commun. , 2013. **34**: p. 938−943.

82. Lee, S.-H., et al., *Silver inkjet printing with control of surface energy and substrate temperature.* Journal of Micromechanics and Microengineering, 2008. **18** p. 075014 (7pp).

83. Beneš, M.J., D. Horák, and F. Svec, *Methacrylate-based chromatographic media.* Journal of Separation Science, 2005. **28**(15): p. 1855-1875.

84. Williams, J.M. and D.A. Wrobleski, *Spatial distribution of the phases in water-in-oil emulsions. Open and closed microcellular foams from cross-linked polystyrene.* Langmuir, 1988. **4**(3): p. 656-662.

85. Williams, J.M., A.J. Gray, and M.H. Wilkerson, *Emulsion stability and rigid foams from styrene or divinylbenzene water-in-oil emulsions.* Langmuir, 1990. **6**(2): p. 437-444.

86. Jeřábek, K., et al., *Porogenic Solvents Influence on Morphology of 4-Vinylbenzyl Chloride Based PolyHIPEs.* Macromolecules, 2008. **41**(10): p. 3543-3546.

87. Cameron, N.R. and A. Barbetta, *The influence of porogen type on the porosity, surface area and morphology of poly(divinylbenzene) PolyHIPE foams.* Journal of Materials Chemistry, 2000. **10**(11): p. 2466-2471.

88. Dubinsky, S., et al., *Microfluidic Synthesis of Macroporous Copolymer Particles.* Macromolecules, 2008. **41**(10): p. 3555-3561.

89. Pakeyangkoon, P., et al., *Polymeric foam via polymerized high internal phase emulsion filled with organo-modified bentonite.* Journal of Applied Polymer Science, 2009. **114**(5): p. 3041-3048.

90. R. Cameron, N. and D. C. Sherrington, *Preparation and glass transition temperatures of elastomeric PolyHIPE materials.* Journal of Materials Chemistry, 1997. **7**(11): p. 2209-2212.

91. Kovacic, S., et al., *Ring opening metathesis polymerisation of emulsion templated dicyclopentadiene giving open porous materials with excellent mechanical properties.* Polymer Chemistry, 2012. **3**(2): p. 325-328.

92. Huš, S. and P. Krajnc, *PolyHIPEs from Methyl methacrylate: Hierarchically structured microcellular polymers with exceptional mechanical properties.* Polymer, 2014. **55**(17): p. 4420-4424.

93. Sevšek, U., et al., *Post polymerisation hypercrosslinking of styrene/divinylbenzene poly(HIPE)s: Creating micropores within macroporous polymer.* Polymer, 2014. **55**(1): p. 410-415.

94. Seo, M., et al., *Hierarchically Porous Polymers from Hyper-cross-linked Block Polymer Precursors.* Journal of the American Chemical Society, 2015. **137**(2): p. 600-603.

95. Luo, Y., A.-N. Wang, and X. Gao, *One-pot interfacial polymerization to prepare PolyHIPEs with functional surface.* Colloid and Polymer Science, 2015. **293**(6): p. 1767-1779.

96. Lovelady, E., et al., *Preparation of emulsion-templated porous polymers using thiol-ene and thiol-yne chemistry.* Polymer Chemistry, 2011. **2**(3): p. 559-562.

97. Menner, A., et al., *Tough reinforced open porous polymer foams via concentrated emulsion templating.* Polymer, 2006. **47**(22): p. 7628-7635.

98. Silverstein, M.S., *Emulsion-templated porous polymers: A retrospective perspective.* Polymer, 2014. **55**(1): p. 304-320.

99. Ikem, V.O., A. Menner, and A. Bismarck, *High-Porosity Macroporous Polymers Sythesized from Titania-Particle-Stabilized Medium and High Internal Phase Emulsions.* Langmuir, 2010. **26**(11): p. 8836-8841.

100. Chen, C., et al., *Emulsion-templated porous polymers prepared by thiol-ene and thiol-yne photopolymerisation using multifunctional acrylate and non-acrylate monomers.* Polymer, 2017. **126**(Supplement C): p. 395-401.

101. Pulko, I. and P. Krajnc, *High Internal Phase Emulsion Templating – A Path To Hierarchically Porous Functional Polymers.* Macromolecular Rapid Communications, 2012. **33**(20): p. 1731-1746.

102. Binks, B.P., et al., *Stability of Oil-in-Water Emulsions in a Low Interfacial Tension System.* Langmuir, 2000. **16**(3): p. 1025-1034.

103. Gibson, L.J. and M.F. Ashby, *Cellular Solids: Structure and Properties*. 2 ed. Cambridge Solid State Science Series. 1997, Cambridge: Cambridge University Press.

104. Gibson, L.J., *Biomechanics of cellular solids.* Journal of Biomechanics, 2005. **38**(3): p. 377-399.

105. Roos, G. *UV LEDs Boost Flux Density and Efficiency, Driving New Applications*. 2014.

106. Gandy, P.J.F. and J. Klinowski, *Exact computation of the triply periodic G (`Gyroid') minimal surface.* Chemical Physics Letters, 2000. **321**(5): p. 363-371.

107. Fee, C., *3D-printed porous bed structures.* Current Opinion in Chemical Engineering, 2017. **18**: p. 10-15.

108. Femmer, T., et al., *Print your membrane: Rapid prototyping of complex 3D-PDMS membranes via a sacrificial resist.* Journal of Membrane Science, 2015. **478**: p. 12-18.

109. Bruchet, A., et al., *Synthesis and Characterization of Ammonium Functionalized Porous Poly(glycidyl methacrylate-co-ethylene dimethacrylate) Monoliths for Microscale Analysis and Its Application to DNA Purification.* Journal of Biomedical Nanotechnology, 2011. **7**(3): p. 415-425.

110. Li, Y., et al., *Preparation of polymeric monoliths by copolymerization of acrylate monomers with amine functionalities for anion-exchange capillary liquid chromatography of proteins.* Journal of Chromatography A, 2009. **1216**(29): p. 5525-5532.

111. Krajnc, P., et al., *Preparation and characterisation of poly(high internal phase emulsion) methacrylate monoliths and their application as separation media.* Journal of Chromatography A, 2005. **1065**(1): p. 69-73.

112. Wertz, C.F. and M.M. Santore, *Adsorption and Reorientation Kinetics of Lysozyme on Hydrophobic Surfaces.* Langmuir, 2002. **18**(4): p. 1190-1199.

113. Trang, H.K., et al., *Evaluation of loading characteristics and IgG binding performance of Staphylococcal protein A on polypropylene*

capillary-channeled polymer fibers. Journal of Chromatography B, 2016. **1015-1016**: p. 92-104.

114. Wang, M., et al., *Preparation and characterization of polyethyleneimine modified ion-exchanger based on poly(methacrylate-co-ethylene dimethacrylate) monolith.* Journal of Chromatography A, 2007. **1147**(1): p. 24-29.

115. Separation, B., *Product Specific Information Sheet, CIM Disks for Ion Exchange Chromatography*. 2015.

116. Staby, A., et al., *Comparison of chromatographic ion-exchange resins: VI. Weak anion-exchange resins.* Journal of Chromatography A, 2007. **1164**(1): p. 82-94.

117. Wakeman, R.J., Z.G. Bhumgara, and G. Akay, *Ion exchange modules formed from polyhipe foam precursors.* Chemical Engineering Journal, 1998. **70**(2): p. 133-141.

Abbreviations

AA	Acrylic acid
AM	Additive manufacturing
ATRP	Atom transfer radical polymerization
BCC	Body centered cubic
BET	Brunauer–Emmet–Teller
BJH	Barrett-Joyner-Halenda
BSA	Bovin serum albumin
CAD	Computer aided design
$CaCl_2.2H_2O$	Calcium chloride dehydrate
CIM	Convective Interaction Media
<D>	Average pore diameter
<d>	Average interconnecting window diameter

DBC	Dynamic binding capacity
DCPD	Dicyclopentadiene
DEA	Diethylamine
DLP	Digital light processing
DMD	Digital micro mirror device
DMF	Dimethylformamide
DMPA	2,2-dimethoxy-2-phenylacetophenone
EDAC	1-ethyl-3-(3-dimethylaminopropyl) carbodiimide hydrochloride
EGDMA	Ethylene glycol dimethylacrylate
EHA	Ethylhexyl acrylate
FCC	Face centered cubic
FDM	Fused deposition modelling
FPLC	Fast protein liquid chromatography

FTIR	Fourier-transform infrared spectroscopy
GMA	Glycidyl methacrylate
GUI	Graphical user interface
HEMA	2-hydroxyethyl methacrylate
HIPE	High internal phase emulsion
HLB	Hydrophilic-Lipophilic Balance
LOM	Laminated object manufacturing
MeOH	Methanol
µLS	Micro laser sintering
µSL	Micro stereo lithography
O/W	Oil-in-water
PAM	Polyacrylamide
PEGDMA	Poly(ethylene glycol) dimethacrylate

PEI	Polyethyleneimine
Pluronic® L-81	Poly(ethylene oxide)-b-poly(propylene oxide)-b-poly(ethylene oxide)
polyHIPE	Poly high internal phase emulsion
RAFT	Reversible addition-fragmentation chain transfer
ROMP	Ring opening metathesis polymerization
SBC	Static Binding Capacity
SC	Simple cubic
scCO2	Supercritical carbon dioxide
SDS-PAGE	Sodium dodecyl sulfate polyacrylamide gel electrophoresis
SFF	Solid Freeform Fabrication
SEM	Scanning electron microscope
SL	Stereo lithography
SLS	Selective laser sintering

δ	Solubility parameter
Sulfo-NHS	N-hydroxysulfosuccinimide
TEGDMA	Triethylene glycol dimethacrylate
3DP	Three Dimensional Printing
W/O	Water-in-oil
W/O/W	Water-in-oil-in-water

Appendix A

Design of developed DLP 3D printer

Figures A-1 and A-2 show the design and CAD drawings of the developed DLP 3D printer. The printer design contains a frame, a DLP projector, a reservoir vat, a printing platform and a wiper. The prepared HIPE was poured in the reservoir vat. The wiper and platform movements control by G-code commands. For printing each layer, the printing platform move downward by a distance equal to the thickness of the single layer to allow a new layer of HIPE monomer to cover the surface of the printing platform. The platform then lift to reach the zero point in the z direction. Next, the wiper move forward and backward in the y direction to make an even covering of the new layer. The DLP then illuminate the layer for the set exposure time and cure the HIPE.

A)

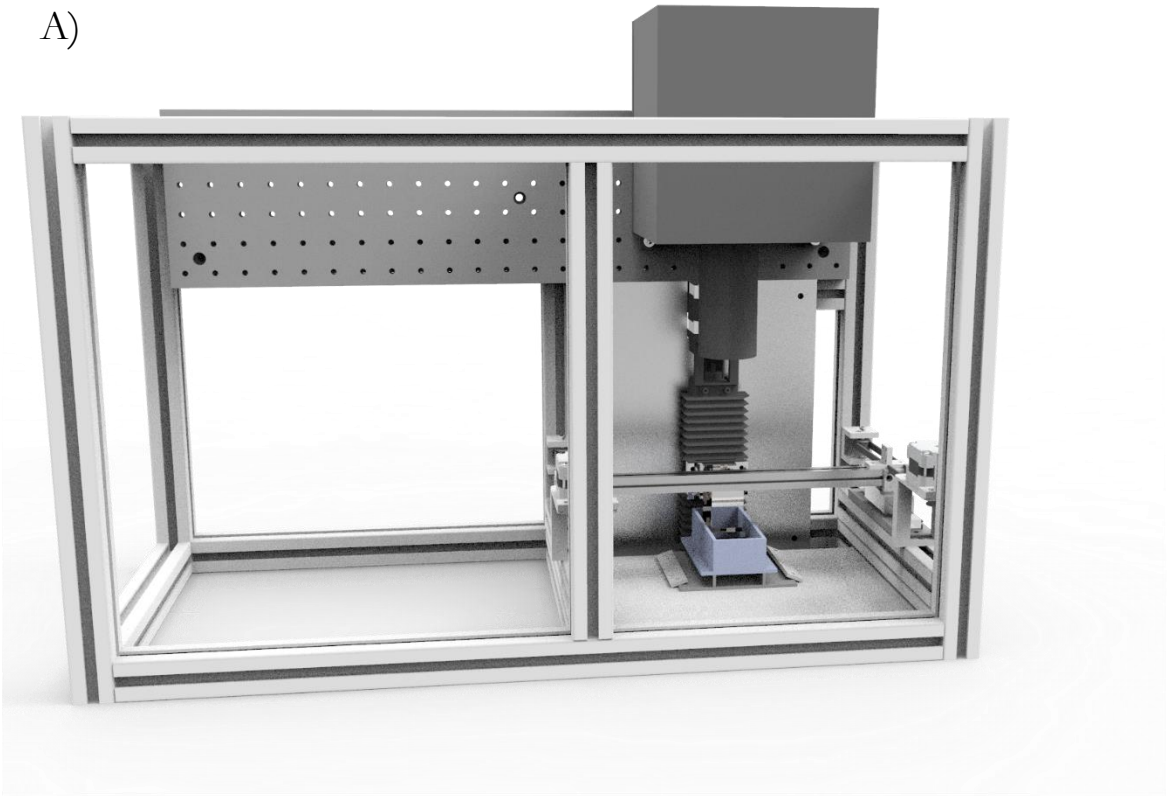

B)

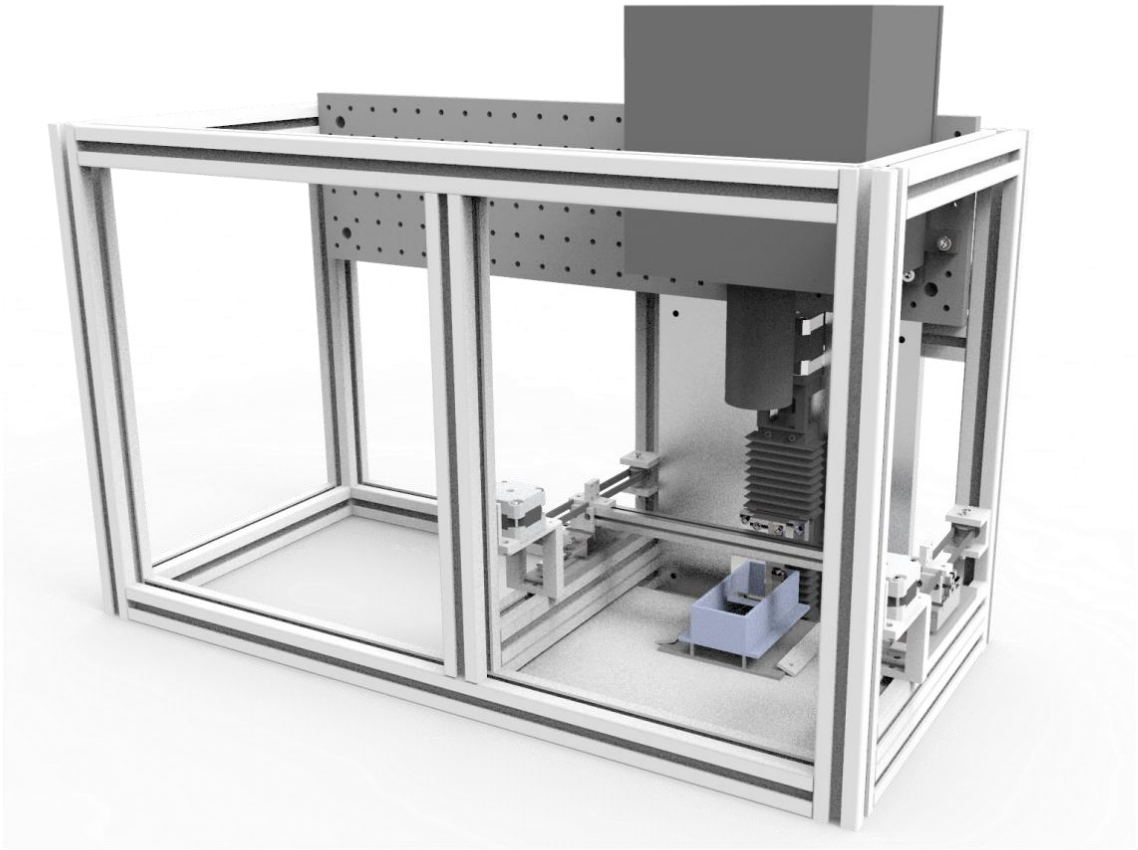

Figure A- 1. 3D modelling of the developed DLP 3D printer from two different views A) straight and B) right.

A)

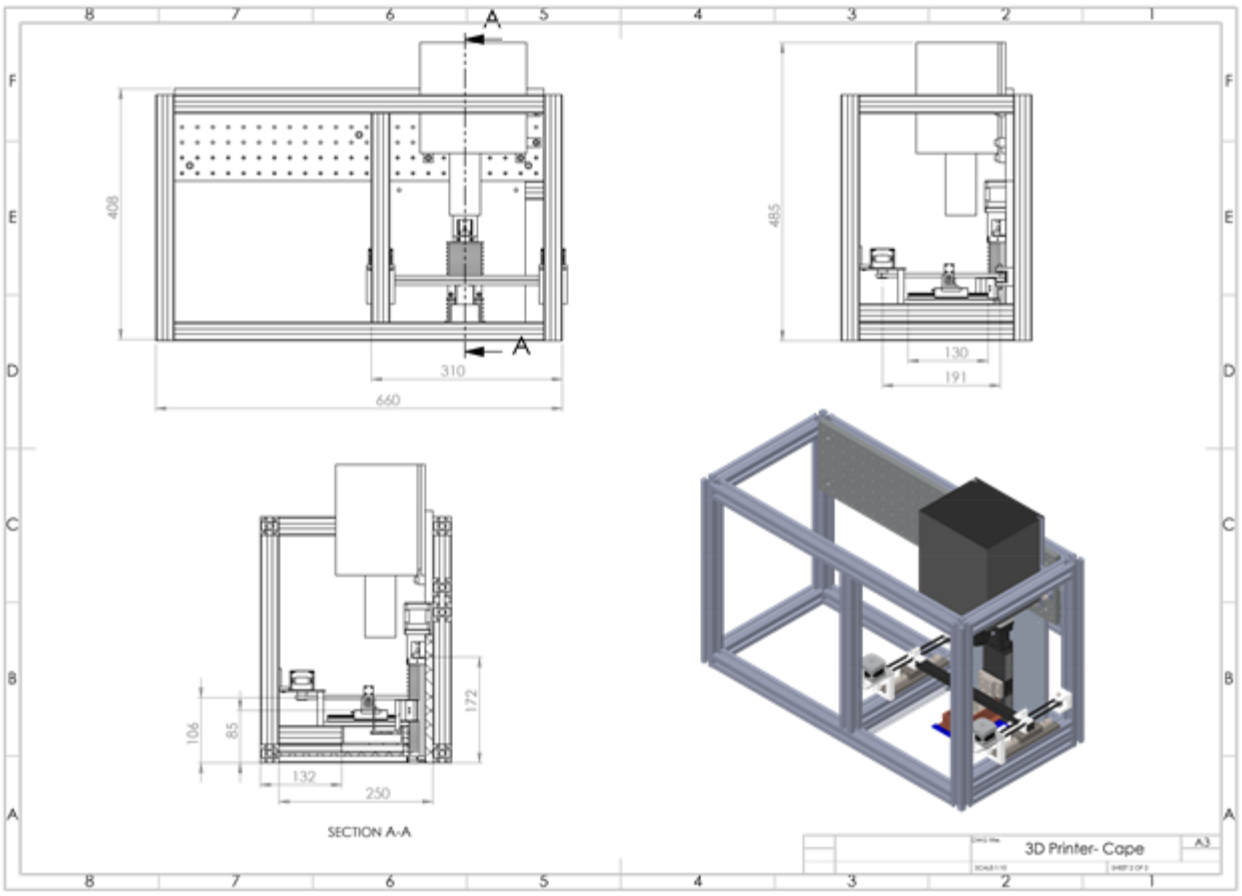
A
A
408
310
660
485
130
191
106
85
172
132
250
SECTION A-A
3D Printer- Cape
A3

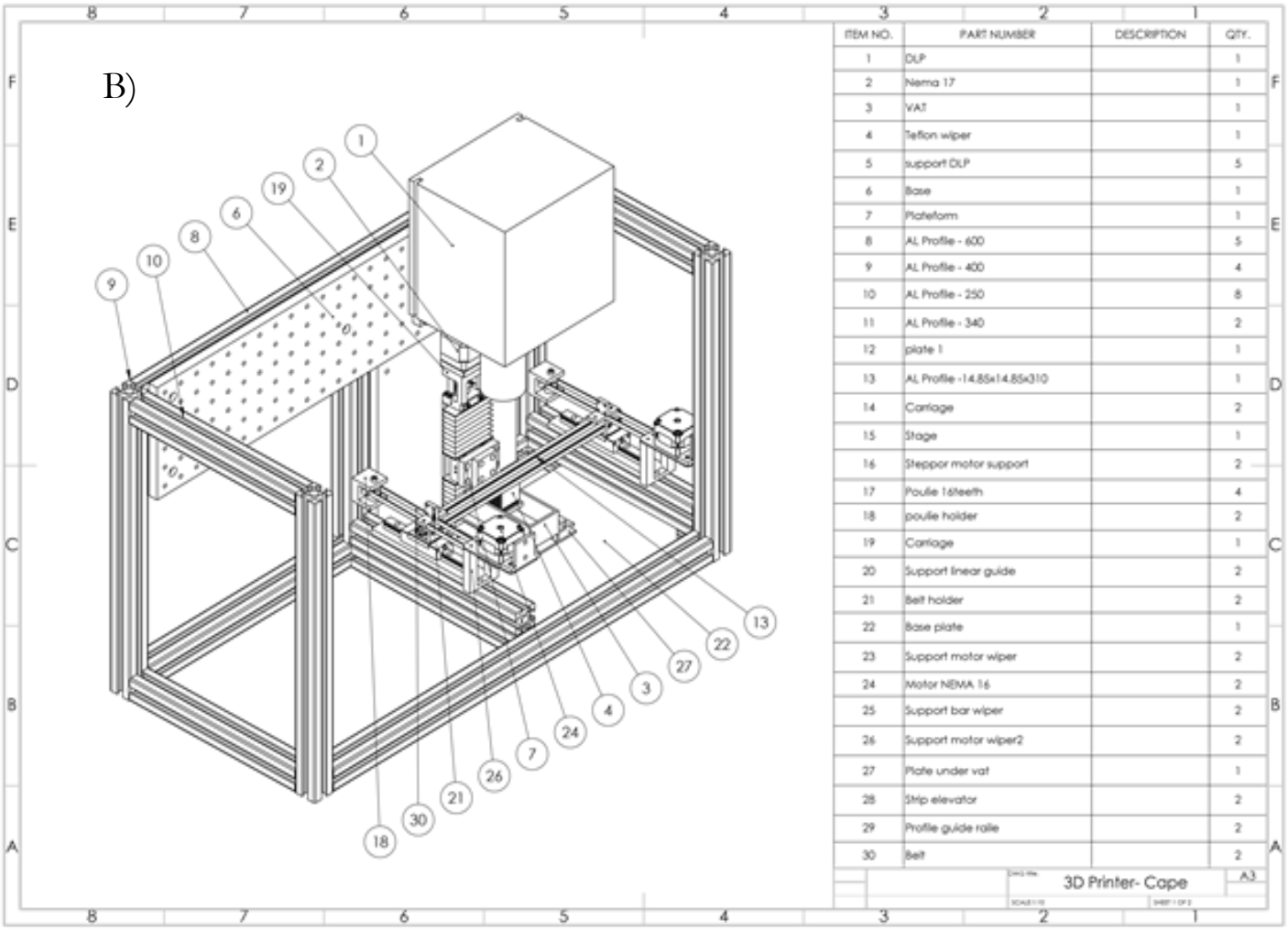

ITEM NO.	PART NUMBER	DESCRIPTION	QTY.
1	DLP		1
2	Nema 17		1
3	VAT		1
4	Teflon wiper		1
5	support DLP		5
6	Base		1
7	Plateform		1
8	AL Profile - 600		5
9	AL Profile - 400		4
10	AL Profile - 250		8
11	AL Profile - 340		2
12	plate 1		1
13	AL Profile -14.85x14.85x310		1
14	Carriage		2
15	Stage		1
16	Steppor motor support		2
17	Poulie 16teeth		4
18	poulie holder		2
19	Carriage		1
20	Support linear guide		2
21	Belt holder		2
22	Base plate		1
23	Support motor wiper		2
24	Motor NEMA 16		2
25	Support bar wiper		2
26	Support motor wiper2		2
27	Plate under vat		1
28	Strip elevator		2
29	Profile guide ralle		2
30	Belt		2

3D Printer- Cape A3

Figure A- 2. CAD drawings of developed DLP 3D printer A) from different views with dimensions B) Bill of Materials.

Appendix B

G-code for printing designed polyHIPE monolith

G-code is a numerical control programming language to control automated machine tools in computer-aided manufacturing. With 3D printing, the G-code has commands that tell the motors where to move, how fast to move, and what path to follow. G-code contains G-commands (movement codes) and M-commands (machine-specific codes). After slicing a model by Workshop Creation software, the developed 3D printer starts moving the printing platform and the wiper according to the speed and direction that has defined by the following G-code commands.

********** Header Start ********
;Here you can set any G or M-Code which should be executed BEFORE the build process
G21 ;Set units to be mm
G91 ;Relative Positioning
M17 ;Enable motors
;********** Header End **********

********** Pre-Slice Start ********
;Set up any GCode here to be executed before a lift
;********** Pre-Slice End **********

********** Lift Sequence ********

```
G1{$SlideTiltVal != 0? X$SlideTiltVal:}

 Z($ZLiftDist * $ZDir) F{$CURSLICE < $NumFirstLayers?$ZBottomLiftRate:$ZLiftRate}
G1{$SlideTiltVal != 0? X($SlideTiltVal * -1):} Z(($LayerThickness-$ZLiftDist) * $ZDir) F$ZRetractRate
;<Delay> %d$BlankTime
;********** Lift Sequence **********


********** Footer Start ********
;Here you can set any G or M-Code which should be executed after the last Layer is Printed
M18 ;Disable Motors
;<Completed>
;********** Footer End ******
```

Appendix C

Controlling the BSA absorbance on the polyHIPE anion exchanger at different flow rates

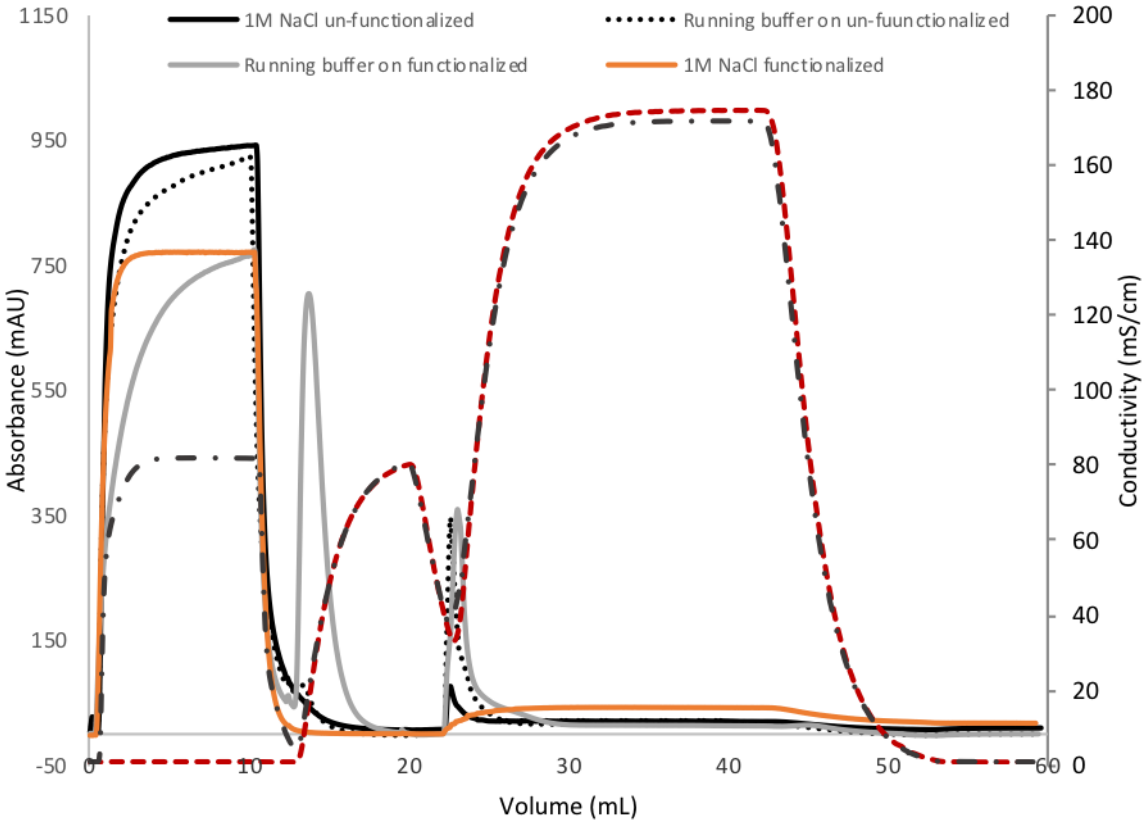

Figure C-1. Chromatograph for 2 mg mL^{-1} BSA absorbance on printed SG-E2-400(78) column at 1 mL min^{-1} flow rates.

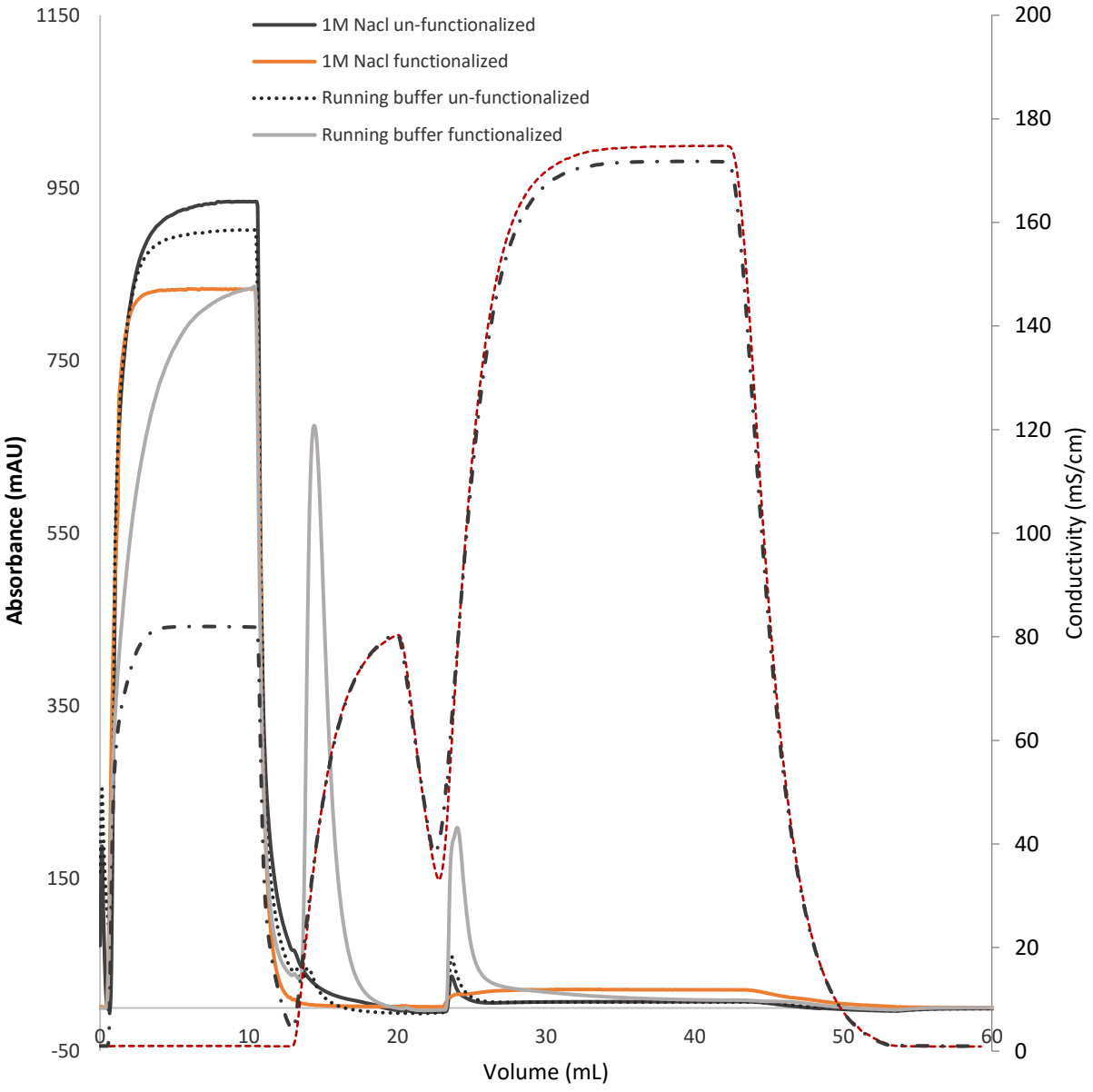

Figure C-2. Chromatograph for 2 mg mL-1 BSA absorbance on printed SG-E2-400(78) column at 4 mL min-1 flow rates.